
**Improved understanding of
boron-oxygen-related carrier lifetime
degradation and regeneration
in crystalline silicon solar cells**

Von der Fakultät für Mathematik und Physik
der Gottfried Wilhelm Leibniz Universität Hannover

zur Erlangung des akademischen Grades

Doktorin der Naturwissenschaften

Dr. rer. nat.

genehmigte Dissertation von

M. Sc. Lailah Helmich

geboren am 04.11.1991 in Hildesheim

Referent: Prof. Dr. Jan Schmidt
Korreferent: Prof. Dr. Tobias Wietler
Korreferent: Prof. Dr. Michael Seibt
Tag der Promotion: 11.07.2022

Was man zu verstehen gelernt hat, fürchtet man nicht mehr.

Marie Curie (1867-1934)

Kurzzusammenfassung

In dieser Arbeit werden Instabilitäten der Ladungsträgerlebensdauer in sauerstoffreichem, Bor-dotiertem p -Typ Czochralski-Silizium (Cz-Si) untersucht, wobei der Schwerpunkt auf der permanenten Deaktivierung des Bor-Sauerstoff (BO)-korrelierten Defektzentrums liegt, die zu einer Regeneration der Lebensdauer führt.

Um widersprüchliche Aussagen aus vorherigen Berichten in der Literatur über den Mechanismus der Regeneration in dieser Arbeit aufzulösen, werden auf Bor-dotierten Cz-Si Wafern hergestellte PERC-Zellen (engl. *passivated emitter and rear solar cell*) im Dunkeln durch Ladungsträgerinjektion über angelegte Spannungen in Vorwärtsrichtung V_{appl} bei erhöhten Temperaturen regeneriert. Die Regenerationskinetik wird unter Regenerationsbedingungen durch das Messen des gesamten Rekombinationsstroms der Zelle bei der tatsächlichen Regenerationstemperatur und einer variierend angelegten Spannung V_{appl} analysiert. Parallel dazu messen wir das von der Solarzelle emittierte Elektrolumineszenzsignal in mehreren Zeitintervallen während der Regeneration, um die injizierte Überschussladungsträgerkonzentration Δn bei jeder angelegten Spannung V_{appl} zu bestimmen. Aus dem zeitabhängig gemessenen Zellstrom wird die Deaktivierungsrate R_{de} des BO-Defekts bestimmt. Die experimentellen Ergebnisse zeigen erstmals eindeutig, dass R_{de} während des Regenerationsprozesses proportional zu Δn ansteigt, wodurch die Unstimmigkeiten aus der Literatur unter Regenerationsbedingungen aufgelöst werden.

Um den Effekt des Wasserstoffs auf die BO-korrelierte Lebensdauerdegradations- und -regenerationskinetik zu ermitteln, werden verschiedene Mengen an Wasserstoff durch eine schnelle thermische Erwärmung (engl. *Rapid Thermal Annealing*, RTA, auch „Feuern“ genannt) in einem industriellen Feuerofen in das Silizium-Volumen eingebracht und durch Messungen einer Widerstandsänderung unter Tempern im Dunkeln quantifiziert. Die Messmethode der Widerstandsänderung basiert auf der Bildung von Bor-Wasserstoff-Paaren. Die Wasserstoffquelle in unseren Experimenten sind wasserstoffreiche Siliziumnitrid ($\text{SiN}_x\text{:H}$)-Schichten, die auf die Oberflächen der Siliziumwafer beidseitig abgeschieden werden. Die Variation der Peak-Temperatur des RTA-Schritts zeigt, dass es ein temperaturabhängiges Maximum des in das Silizium-Volumen eingetragenen Wasserstoff-Gehalts gibt. Die genaue Position dieses Maximums hängt von der Zusammensetzung der $\text{SiN}_x\text{:H}$ -Schichten ab. Der höchste Wasserstoff-Gehalt, der 10^{15} cm^{-3} übersteigt, wird von siliziumreichen SiN_x -Schichten mit einem Brechungsindex von $n = 2.3$ (bei einer Wellenlänge von $\lambda = 633 \text{ nm}$) bei einer RTA Peak-Temperatur von $800 \text{ }^\circ\text{C}$ in das Silizium-Volumen eingetragen. Das Einfügen einer 20 nm dicken Al_2O_3 -Zwischenschicht zwischen die Silizium-Waferoberfläche und den $\text{SiN}_x\text{:H}$ Schichten reduziert den eindiffundierten Wasserstoff-Gehalt um einen Faktor von vier, was zeigt, dass Al_2O_3 als effektive Wasserstoffdiffusionsbarriere wirkt. Durch die Variation der Al_2O_3 -Dicke wird der Wasserstoff-Gehalt um mehr als eine Größenordnung variiert. Um den Einfluss des Wasserstoffs auf die Degradationskinetik zu untersuchen, werden alle Proben mit einer Lichtintensität von 0.1 Sonnen bei Raumtemperatur beleuchtet. Es wurde kein Einfluss des eindiffundierten Wasserstoff-Gehalts auf die Degradationsrate beobachtet, was bestätigt, dass Wasserstoff nicht am BO-Degradationsmechanismus beteiligt ist. Regenerationsexperimente mit einer Lichtintensität von 1 Sonne bei erhöhter Temperatur zeigen jedoch eine deutliche Abhängigkeit vom Wasserstoff-

Gehalt über einen linearen Anstieg der Regenerationsrate mit zunehmender Wasserstoffkonzentration im Silizium-Volumen. Eine Extrapolation dieser Korrelation auf einen Wasserstoff-Gehalt von Null im Silizium-Volumen zeigt, dass die Regeneration auch ohne eindiffundierten Wasserstoff funktioniert. Unsere Experimente zeigen also zum ersten Mal deutlich, dass zwei verschiedene Regenerationsprozesse stattfinden, einer mit und einer ohne die Beteiligung von Wasserstoff. Diese Ergebnisse bestätigen ein vorausgegangenes theoretisches Modell, das bisher noch nicht experimentell verifiziert worden war.

In einer weiteren Versuchsreihe untersuchen wir die Langzeitstabilität der Ladungsträgerlebensdauer in Bor-dotierten Cz-Si Materialien mit unterschiedlichen Bor- und Sauerstoff-Konzentrationen nach Regeneration in einem industriellen Feuerofen. Nach dem Feuern mit anschließender Regeneration im Feuerofen werden die Silizium-Proben einer Langzeitbeleuchtung ausgesetzt mit einer Lichtintensität von 0.1 Sonnen bei einer Proben temperatur von 30 °C. Nach der Regeneration degradieren die Proben in ihrer Lebensdauer erneut (30-72% weniger im Vergleich zur beobachteten Degradation ohne Regenerationsschritt). Diese erneute Degradation wird auf eine unvollständige Regeneration im Feuerofen zurückgeführt aufgrund der kurzen Regenerationszeit. Alles in allem scheint der Industrieprozess, bestehend aus einem Feuerschritt mit anschließender Regeneration in derselben Anlage, für industriell relevante Silizium-Materialien sehr effektiv zu sein. Typische industrielle Silizium-Wafer mit einem spezifischen Widerstand von $(1.75 \pm 0.03) \Omega\text{cm}$ und einer interstitiellen Sauerstoffkonzentration von $(6.9 \pm 0.3) \times 10^{17} \text{ cm}^{-3}$ weisen nach Regeneration und zwei Jahren der Beleuchtung Lebensdauern von mehr als 2 ms auf.

Abstract

This thesis examines carrier lifetime instabilities in oxygen-rich boron-doped *p*-type Czochralski-grown silicon (Cz-Si) with the focus on the permanent deactivation of the boron-oxygen (BO)-related defect center leading to a regeneration in lifetime. In order to resolve contradictory statements reported previously in the literature concerning the mechanism of regeneration in this thesis, passivated emitter and rear solar cells (PERCs) fabricated on boron-doped *p*-type Cz-Si wafers are regenerated in darkness by carrier injection via application of a forward-bias voltage V_{appl} at elevated temperatures. The regeneration kinetics is analyzed under regeneration conditions by measuring the total recombination current of the solar cell at the actual regeneration temperature at varying applied voltages V_{appl} . In parallel, we measure the electroluminescence signal emitted by the solar cell at different time steps during regeneration to directly determine the injected excess carrier concentration Δn at each applied forward-bias voltage V_{appl} . The deactivation rate constant R_{de} of the BO defect is determined from the measured time-dependent cell current. The experimental results show unambiguously for the first time that R_{de} increases proportionally with Δn during the regeneration process, solving the inconsistencies reported in the literature under actual regeneration conditions.

To identify the impact of hydrogen on the BO-related lifetime degradation and regeneration kinetics, different amounts of hydrogen are introduced into the silicon bulk by rapid thermal annealing (RTA) treatment in an infrared conveyor-belt furnace quantified by measurements of the silicon resistivity increase. The silicon resistivity increases under dark-annealing due to hydrogen passivation of boron dopant atoms. The hydrogen source in our experiments are hydrogen-rich silicon nitride ($\text{SiN}_x\text{:H}$) layers deposited on the silicon wafer surfaces. Varying the peak-temperature of the RTA step indicates that there exists a temperature-dependent maximum in the hydrogen content introduced into the silicon bulk. The exact position of this maximum depends on the composition of the $\text{SiN}_x\text{:H}$ layers. The highest total hydrogen content, exceeding 10^{15} cm^{-3} , is introduced into the silicon bulk from silicon-rich SiN_x layers with a refractive index of $n = 2.3$ (at a wavelength of $\lambda = 633 \text{ nm}$) at an RTA peak temperature of $800 \text{ }^\circ\text{C}$. Adding a 20 nm thick Al_2O_3 interlayer in-between the silicon wafer surfaces and the $\text{SiN}_x\text{:H}$ layers, reduces the in-diffused hydrogen content up to a factor of four, demonstrating that Al_2O_3 acts as a highly effective hydrogen diffusion barrier. By varying the Al_2O_3 thickness, the hydrogen bulk content is varied over more than one order of magnitude. In order to examine the impact of hydrogen on the degradation kinetics, all samples are illuminated at a light intensity of 0.1 suns near room temperature. No influence of the in-diffused hydrogen content on the degradation rate constant is measured, confirming that hydrogen is not involved in the BO degradation mechanism. The regeneration experiments at a light intensity of 1 suns at elevated temperatures, however, show a clear dependence on the hydrogen content with a linear increase of the regeneration rate constant with increasing bulk hydrogen concentration. An extrapolation of this correlation towards a zero in-diffused hydrogen content shows that the regeneration is still working even without any in-diffused hydrogen. Hence, our experiments clearly reveal for the first time that two distinct regeneration processes are taking place, one involving hydrogen, the other not. These results confirm a previous theoretical model, which had

not been experimentally verified so far.

In another series of experiments, we examine the long-term stability of the carrier lifetime in boron-doped Cz-Si materials with different boron and oxygen concentrations after regeneration in an industrial belt furnace. After firing and subsequent regeneration in the conveyor-belt furnace, the silicon samples are exposed to long-term illumination at an intensity of 0.1 suns and a sample temperature of about 30 °C for more than two years. After regeneration, the lifetime samples re-degrade (30-72 % reduced compared to the degradation observed without regeneration step). This re-degradation is attributed to an incomplete regeneration within the belt furnace due to the short regeneration period. All in all, the industrial process consisting of firing with subsequent regeneration in the same belt-furnace unit seems to be very effective for industrially relevant silicon materials. Typical industrial silicon wafers with a resistivity of $(1.75 \pm 0.03) \Omega\text{cm}$ and an interstitial oxygen concentration of $(6.9 \pm 0.3) \times 10^{17} \text{ cm}^{-3}$ show lifetimes larger than 2 ms after regeneration and two years of light exposure.

Schlagwörter: Bor-Sauerstoff-Defekt, Czochralski-gezogenes Silizium, Ladungsträgerlebensdauer, Solarzelle, Regeneration, Elektrolumineszenz, Wasserstoff, Aluminiumoxid, Langzeitstabilität

Keywords: boron-oxygen-defect, Czochralski-grown silicon, charge carrier lifetime, solar cell, regeneration, electroluminescence, hydrogen, aluminum oxide, long-term stability

Contents

1	Introduction	3
1.1	Brief overview of the thesis	3
2	Characterization and sample preparation methods	5
2.1	Characterization methods	5
2.1.1	Carrier lifetime measurements	5
2.1.2	Luminescence-based imaging techniques	10
2.1.3	Fourier-Transform Infrared spectroscopy	12
2.1.4	Resistivity measurements	17
2.1.5	Ellipsometry	18
2.2	Sample preparation methods	21
2.2.1	Atomic layer deposition	22
2.2.2	Plasma-enhanced chemical vapor deposition	24
3	Review of boron-oxygen-related light-induced degradation and regeneration in crystalline silicon	27
3.1	Boron-oxygen-related carrier lifetime degradation	27
3.2	Permanent deactivation of BO-related recombination centers	31
3.2.1	The role of hydrogen	35
3.3	BO defect models	36
3.3.1	Physical models	36
3.3.1.1	B_sO_{2i} model	36
3.3.1.2	B_iO_{2i} model	38
3.3.1.3	$B_iB_sO_i$ model	40
3.3.1.4	Permanent deactivation model	42
4	In-situ characterization of electron-assisted regeneration of Cz-Si solar cells	45
4.1	Introduction	45
4.2	Experimental details	47
4.3	In-situ measured degradation and regeneration kinetics	50
4.4	Determination of the excess carrier concentration via EL	53
4.5	Regeneration rate constant as a function of excess carrier concentration	57
4.6	In-situ regeneration experiments of lifetime samples	58
4.7	Chapter summary	58
5	Impact of hydrogen on the boron-oxygen-related lifetime degradation and regeneration kinetics	61
5.1	Introduction	62
5.2	Experimental details	63
5.3	Determination of hydrogen concentration via resistivity measurements	64

5.4	Impact of RTA treatment and silicon nitride composition on hydrogen in-diffusion	65
5.5	Impact of aluminum oxide thickness on hydrogen in-diffusion	69
5.6	Impact of firing temperature on the effective lifetime	72
5.7	Impact of silicon material on hydrogen in-diffusion	73
5.8	Impact of hydrogen on the boron-oxygen-related lifetime degradation	76
5.9	Impact of hydrogen on the boron-oxygen-related lifetime regeneration	78
5.10	Chapter summary	81
6	Carrier lifetime stability of boron-doped Cz-Si materials for years after regeneration in an industrial belt furnace	83
6.1	Introduction	83
6.2	Experimental details	84
6.3	Lifetime measurements and analysis	86
6.4	Defect analysis	92
6.5	Discussion	94
6.6	Summary	94
7	Summary	97
	Bibliography	101
	Publications	I
	List of Figures	III
	List of Tables	XI
	Abbreviations	XIII
	Arabic symbols	XV
	Greek symbols	XIX
	Chemical formula	XXI
	Danksagung	XXIII
	Curriculum vitae	XXV

1 Introduction

In boron-doped Czochralski-grown silicon (Cz-Si), the carrier lifetime degrades severely under illumination near room temperature due to the activation of a boron-oxygen (BO) defect center [1–3]. If the samples are, however, illuminated during annealing, it was found that the BO defect can be permanently deactivated [4]. After permanent deactivation of the BO defect, the efficiency of solar cells based on *p*-type boron-doped Cz-Si can be improved by up to 3% absolute [5, 6].

The aim of this thesis is to develop an improved understanding of the boron-oxygen-related light-induced degradation and regeneration of Cz-Si lifetime samples and solar cells through advanced characterization methods and is subdivided into five chapters. The focus is to investigate the regeneration kinetics at the *actual* regeneration conditions and as a function of the hydrogen content in the silicon bulk as well as to examine the lifetime stability after regeneration.

1.1 Brief overview of the thesis

Chapter 2: Characterization and sample preparation methods

To improve our understanding of the boron-oxygen-related light-induced lifetime degradation and regeneration, various characterization methods are applied to boron-doped Cz-Si lifetime samples and solar cells, some of them newly developed in this thesis. Chapter 2 introduces the experimental setups and a detailed understanding of the physical principle. In addition, Chapter 2 introduces two different deposition techniques applied in this work for sample preparation, namely plasma-assisted atomic layer deposition (PA-ALD) and plasma-enhanced chemical vapor deposition (PECVD).

Chapter 3: Review of boron-oxygen-related light-induced degradation and regeneration in crystalline silicon

The purpose of Chapter 3 is to provide a comprehensive overview of previous research activities prior to this work concerning the boron-oxygen(BO)-related recombination centre in crystalline silicon. The activation and permanent deactivation of the BO recombination centre leading to the degradation and regeneration of the carrier lifetime, is described and discussed in detail and physical defect models explaining the degradation/regeneration behavior are presented.

Chapter 4: In-situ characterization of electron-assisted regeneration of Cz-Si solar cells

Until this thesis, the dependence of the boron-oxygen deactivation rate constant, respectively the regeneration rate constant R_{reg} , had only been analyzed by lifetime measurements at room temperature. In Chapter 4, the regeneration kinetics are for the first time examined at the *actual* regeneration temperature at a well-defined injected excess carrier concentration Δn . PERC solar cells fabricated on boron-doped p -type Czochralski-grown silicon are used to address the dependence of R_{reg} on Δn . In addition, the injected excess carrier concentration during regeneration is determined by a newly designed setup for electroluminescence measurements during the regeneration of solar cells. The regeneration rate constant is extracted as a function of the injected excess carrier concentration solving the inconsistencies reported before in the literature.

Chapter 5: Impact of hydrogen on the boron-oxygen-related lifetime degradation and regeneration kinetics

To identify the impact of hydrogen on the BO-related lifetime degradation and regeneration kinetics in Cz-Si, different amounts of hydrogen are introduced into the silicon bulk by rapid thermal annealing (RTA).

In Chapter 5, the hydrogen content in the silicon bulk is quantified by measurements of the silicon resistivity increase during dark-annealing due to hydrogen passivation of boron dopant atoms. The hydrogen source are thereby hydrogen-rich silicon nitride ($\text{SiN}_x\text{:H}$) layers. By varying the peak firing temperature during RTA and the thickness of aluminum oxide interlayers between the silicon wafer and the $\text{SiN}_x\text{:H}$ layer, different amounts of hydrogen were introduced into the silicon bulk.

Chapter 6: Carrier lifetime stability of boron-doped Cz-Si materials for years after regeneration in an industrial belt furnace

Finally, in Chapter 6 the long-term stability of the carrier lifetime in boron-doped Cz-Si materials with different boron and oxygen concentrations is examined after regeneration in an industrial belt furnace. The Cz-Si materials are typical present-day industrial Cz-Si materials, standard Cz-Si material from the early 2000s and wafers from the top region of a silicon crystal, which are illuminated by 0.1 suns illumination intensity at room temperature after regeneration for up to 2 years.

2 Characterization and sample preparation methods

In the first part of this chapter, characterization techniques for (i) carrier lifetime measurements in crystalline silicon wafer, (ii) measurements of spatially resolved excess carrier concentrations in wafers and solar cells, (iii) measurements of atomic bond concentrations within dielectric layers, (iv) for the analysis of optical layer properties are presented. In the second part of this chapter, two different deposition techniques applied in this work are described: (i) plasma-assisted atomic layer deposition (PA-ALD) and (ii) plasma-enhanced chemical vapor deposition (PECVD).

2.1 Characterization methods

2.1.1 Carrier lifetime measurements

The WCT-120 measurement system from Sinton Instruments [7] is used in this work to measure the carrier lifetime of samples as a function of excess carrier concentration. The experimental setup is schematically illustrated in Figure 2.1.

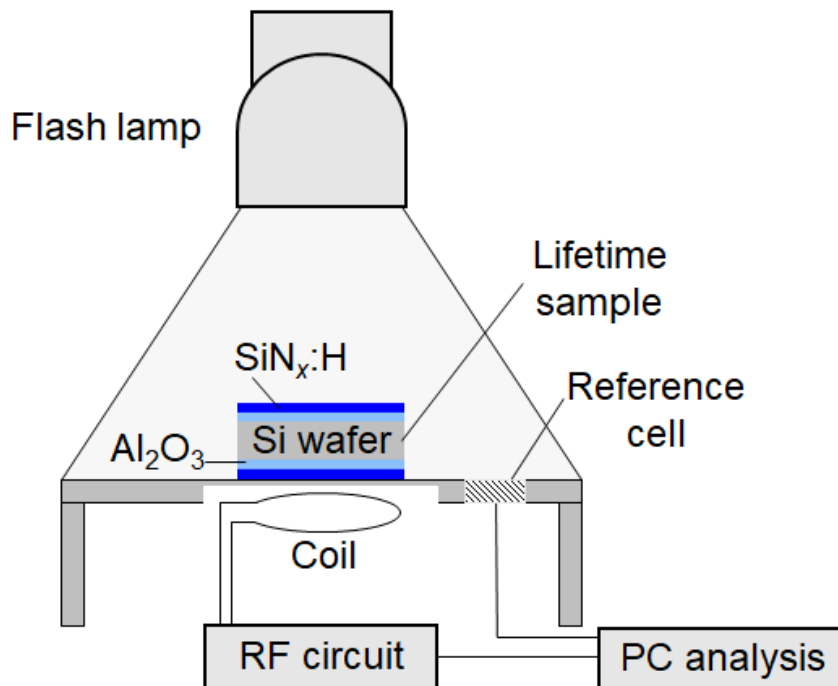


Figure 2.1: Schematic of the experimental setup of the WCT-120 System from Sinton Instruments.

The sample, in our case a Si wafer, is inductively coupled to a coil of an rf-bridge circuit and the output voltage of this circuit is directly proportional to the samples conductance. By measuring the voltage of eleven calibration wafers with different doping concentrations or known sheet resistance R_{sheet} , the sample conductance σ according to

$$\sigma = \frac{1}{R_{\text{sheet}}} \quad (2.1)$$

can be correlated to the output voltage V , as illustrated in Figure 2.2, with a calibration curve of the general expression

$$\sigma = A \times V^2 + B \times V + C \quad . \quad (2.2)$$

The prefactors A , B and the constant C are determined and checked by regular calibration procedures. The calibration wafer with the lowest doping concentration has a sample conductance of 0.0020 Siemens, whereas the calibration wafer with the highest doping concentration has a sample conductance of 0.3378 Siemens.

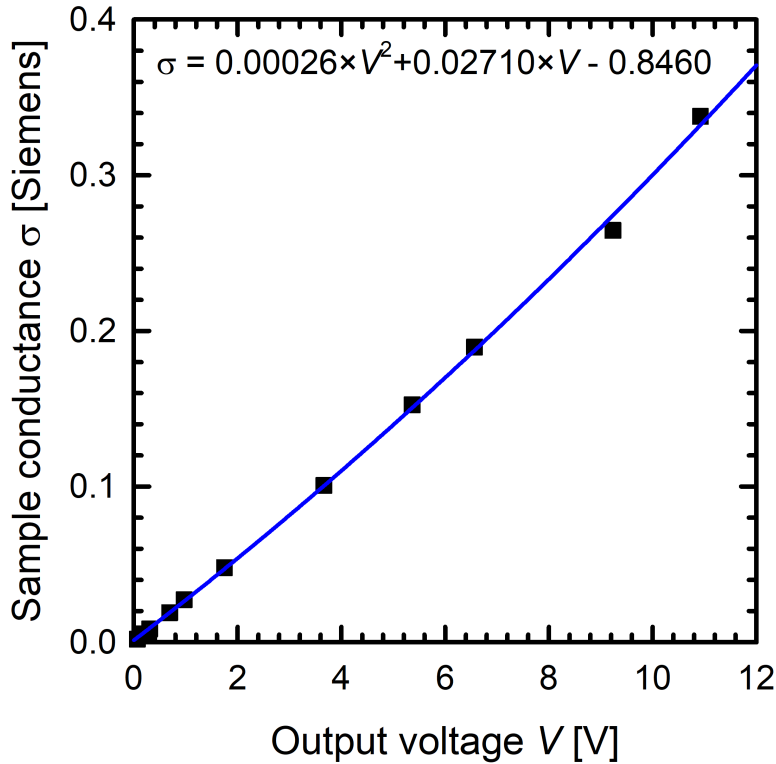


Figure 2.2: Calibration of the coil for lifetime measurements in the experimental setup of the WCT-120 System from Sinton Instruments by different calibration wafers with different conductances.

By illumination with a flash Xe-lamp, electron-hole pairs, i.e. excess carriers with a concentration Δn , are generated within the silicon sample by a photogeneration rate G , resulting in an increased measured sample conductance. For a homogenous generation of excess carriers, realized by a long-pass filter in front of the flash lamp, one can assume that the induced Δn is constant over the thickness of the silicon wafer. The total conductance is then given by

$$\sigma = \sigma_0 + q_e W \Delta n (\mu_n + \mu_p) = \sigma_0 + \Delta \sigma_{\text{ph}} \quad , \quad (2.3)$$

2.1 Characterization methods

with the sample's dark conductance σ_0 , the elementary charge q_e , the wafer thickness W and the mobilities of electrons μ_n and holes μ_p . The latter two quantities depend on the excess carrier density and the value for their sum can be taken from the literature [8]. The second term of Equation (2.3) can be summarized as the sample's conductance under illumination, also called photoconductance $\Delta\sigma_{\text{ph}}$, which is a time-variable photoinduced parameter instead of σ_0 , which is constant over illumination time. According to Equation (2.3), the generated excess carrier concentration Δn is calculated via the recorded photoconductance $\Delta\sigma_{\text{ph}}$ by

$$\Delta n = \frac{\Delta\sigma_{\text{ph}}}{q_e W (\mu_n + \mu_p)} . \quad (2.4)$$

The time-dependent illumination intensity of the flash light is measured over an integrated reference solar cell in the sample stage. From the measured short-circuit current density of the reference cell under 1 sun $J_{\text{sc.1 sun}}$, the generation rate G can be calculated according to

$$G = \frac{I_{\text{ill}} \times J_{\text{sc.1 sun}} \times T_{\text{eff}}}{q_e W} , \quad (2.5)$$

with the measured time-dependent illumination intensity I_{ill} (in suns) from the reference cell and the effective transmission T_{eff} , which takes differences in the photogeneration within the silicon sample and the reference cell due to i.e. differing optical properties or thicknesses into account. Thus, G can be directly calculated from the measured light intensity I_{ill} . The ratio G/I_{ill} was found to be $2.5 \times 10^{17} \text{ cm}^{-3}\text{s}^{-1}\text{suns}^{-1}$ if G is in $\text{cm}^{-3}\text{s}^{-1}$ and I_{ill} is in suns [9]. Besides the generation rate, the time evolution of the excess carrier concentration $\Delta n(t)$ within the sample is also influenced by the simultaneous recombination of electron-hole pairs by the recombination rate U via the continuity equation [10]

$$\frac{\partial \Delta n(x, t)}{\partial t} = G(x, t) - U(x, t) + \frac{1}{q_e} \frac{\partial J_n}{\partial x} , \quad (2.6)$$

with J_n being the electron current density. If the carrier distribution upon illumination is homogeneous, the latter term in Equation (2.6) and the local dependence on the coordinate x vanishes. By the definition of the effective lifetime $\tau_{\text{eff}} = \Delta n/U$ a generalized expression for the effective carrier lifetime τ_{eff} can be derived from Equation 2.6 [10]:

$$\tau_{\text{eff}} = \frac{\Delta n}{G(t) - \frac{\partial \Delta n(t)}{\partial t}} . \quad (2.7)$$

For the lifetime measurements, two modes of flash excitation with different decay time constants are used. In both modes, the excess carrier concentration is determined via the recorded decay of the sample's photoconductance (see Equation (2.4)). However, regarding the illumination, we differentiate between the photoconductance-decay method (PCD), as illustrated in Figure 2.3(a), and the quasi-steady-state photoconductance (QSSPC) method, as illustrated in Figure 2.3(b).

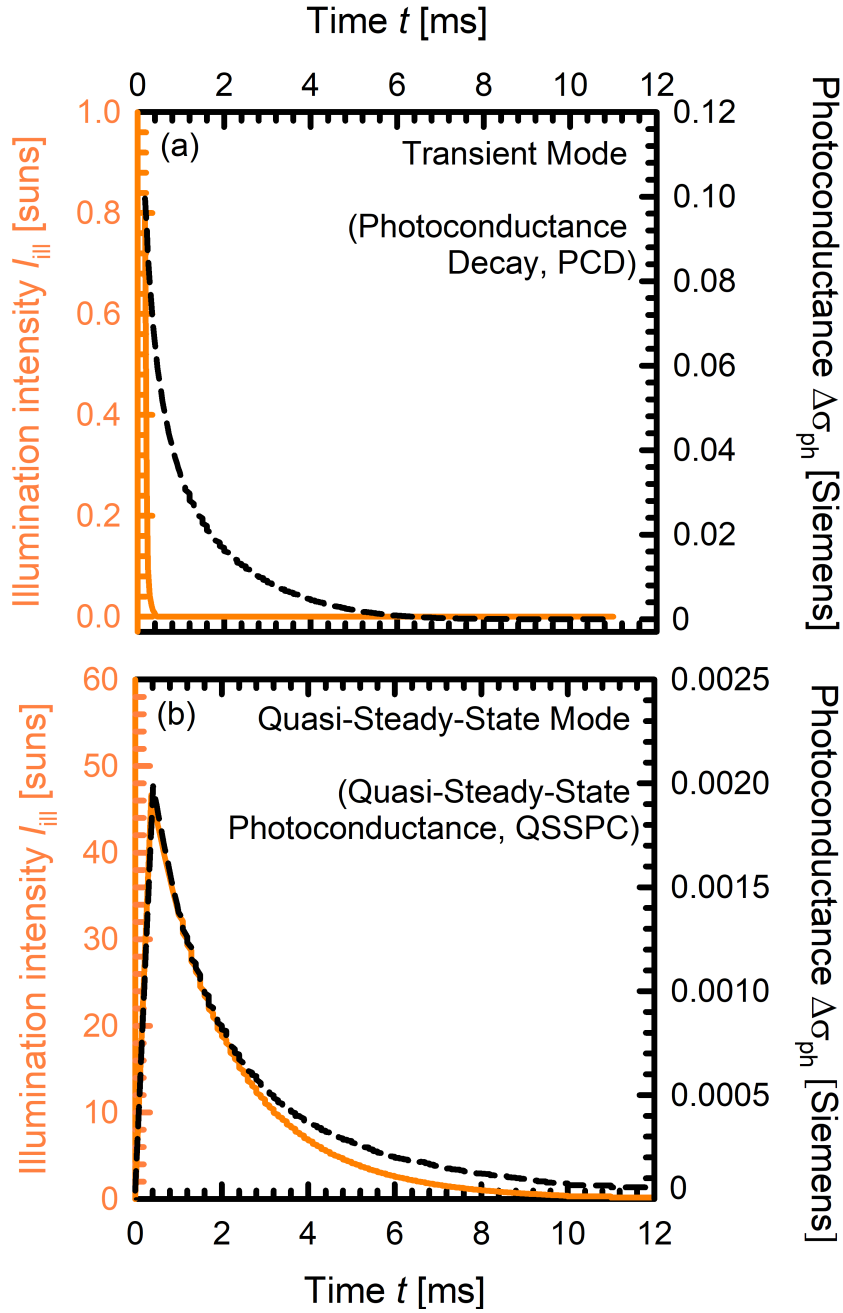


Figure 2.3: Illumination intensity I_{ill} (straight line) and photoconductance $\Delta\sigma_{\text{ph}}$ (dashed line) plotted versus time t , measured by means of the WCT-120 System from Sinton Instruments. (a) Quasi-Steady-State Photoconductance (QSSPC) mode with a long flash and (b) Photoconductance Decay (PCD) technique with a short flash pulse compared to the lifetime of the Si sample.

The **PCD method** with a short flash is applied for lifetime extraction if the sample exhibits carrier lifetimes which are much larger compared to the decay time constant of the flash light. The generation rate can then be neglected after full decay of the flash (i.e. $G = 0$) and as a consequence

$$\tau_{\text{eff}} = -\frac{\Delta n}{\frac{\partial \Delta n}{\partial t}} \quad (2.8)$$

2.1 Characterization methods

The **QSSPC method** on the other hand uses a very slowly decaying flash (typically in the millisecond range) compared to the sample's lifetime. In this case, Eq. (2.7) can be directly applied. In the special case that the carrier lifetimes are significantly smaller than the flash decay time constant, the generation and recombination rates are equal at each t and $\partial\Delta n/\partial t = 0$ is resulting in

$$\tau_{\text{eff}} = \frac{\Delta n}{G} , \quad (2.9)$$

which is the steady-state case. In Figure 2.4, typical injection-dependent BO-related lifetime curves are shown, which were measured by the QSSPC method due to the relatively short lifetimes.

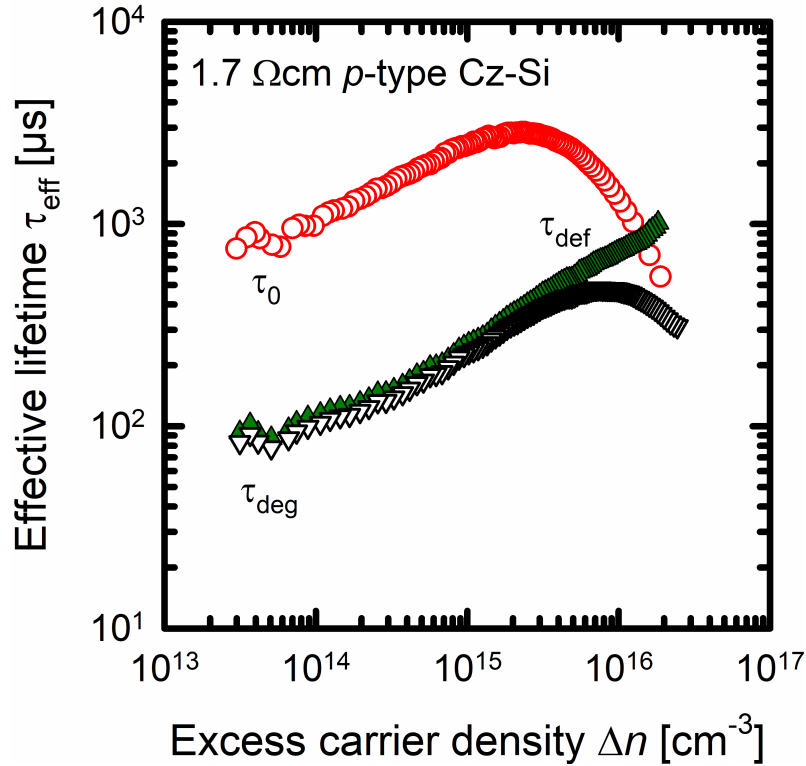


Figure 2.4: Injection-dependent lifetimes after complete degradation under illumination at room temperature (open triangles) and after annealing in darkness (open circles) for an 1.7 Ωcm *p*-type Cz-Si sample with an Al₂O₃/SiN_x-stack on both surfaces for passivation. According to the measured resistivity and Fourier-Transform-Infrared (FTIR) spectrum the sample has a boron concentration N_A about $8.3 \times 10^{15} \text{ cm}^{-3}$ and an oxygen concentration $[O_i]$ of $7 \times 10^{17} \text{ cm}^{-3}$. The green solid lifetime curve represents the lifetime of the activated defect, obtained by Eq.(2.10).

As can be seen, the lifetime shows a strong dependence on the generated excess carrier density, also called injection dependence. After interpolation of the lifetime curves to comparable excess carrier density values, the difference of the injection-dependent lifetimes after complete degradation under illumination at room temperature τ_{deg} and after annealing in darkness τ_0 results in the lifetime of the activated defect τ_{def} :

$$\tau_{\text{def}} = \left(\frac{1}{\tau_{\text{deg}}} - \frac{1}{\tau_0} \right)^{-1} . \quad (2.10)$$

Plotting the normalized defect-related lifetime $\tau_{\text{def}}/\tau_{n0}$ versus the ratio of the electron-to-hole concentrations n/p can help to identify defect centers (see Section 6.4). In this work, we focus on the activated BO defect.

2.1.2 Luminescence-based imaging techniques

The photoconductance-calibrated photoluminescence imaging (PC-PLI) characterization technique is based on the principle of photoluminescence (PL) emission. As shown in Figure 2.5(a), the silicon sample is homogeneously illuminated by a laser diode at a wavelength of $\lambda = 808 \text{ nm}$, which is widened and homogenised by an array of microlenses for homogenisation [11]. Electron-hole pairs are generated in the silicon wafer under test followed by radiative band-to-band recombination. The emitted PL signal is measured by a silicon charge-coupled device (Si-CCD) camera. In Figure 2.5(b), a photoluminescence image of a boron-doped Cz-Si lifetime sample at a laser intensity of 0.9 suns is shown. It indicates an influence of the rotation symmetric Czochralski process by ring-like structures and of sample handling by dark areas of lower PL-intensity due to a deteriorated passivation quality.

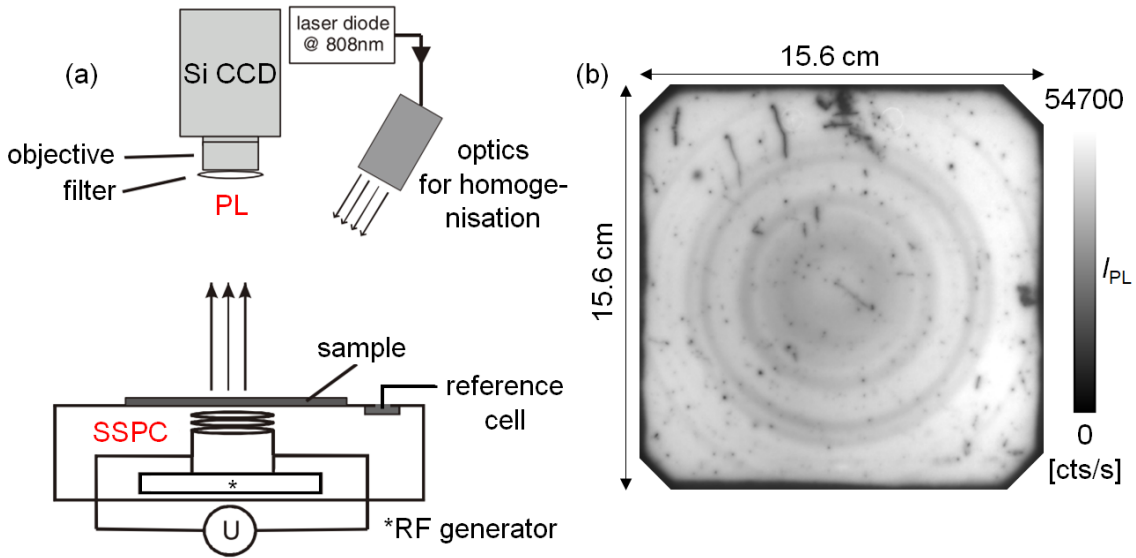


Figure 2.5: (a) Schematic of the photoconductance-calibrated photoluminescence imaging (PC-PLI) setup for spatially resolved measurements of the carrier lifetime, taken from [11]. (b) Photoluminescence (PL) image of an $1.6 \Omega\text{cm}$ p -type Cz-Si sample with an $\text{Al}_2\text{O}_3/\text{SiN}_x$ -stack on both surfaces for passivation at a laser intensity of 0.9 suns.

The intensity of the PL signal I_{PL} is proportional to the radiative recombination rate U_{rad} , which itself is dependent on the product of the electron n and hole concentrations p . For a p -type silicon sample, the electron concentration $n = \Delta n + n_0$ simplifies to $n = \Delta n$, neglecting n_0 due to p -type doping ($n_0 \ll p_0 = N_{\text{dop}}$), and $p = \Delta p + N_{\text{dop}}$ becomes $p = \Delta n + N_{\text{A}}$ assuming charge neutrality ($\Delta p = \Delta n$). Thus, the PL intensity I_{PL} is quadratically dependent on the generated excess carrier density Δn [11]:

$$I_{\text{PL}} \propto U_{\text{rad}} \approx B \Delta n (\Delta n + N_{\text{A}}) \quad , \quad (2.11)$$

2.1 Characterization methods

with B being the coefficient of radiative recombination. For calibration, the generated excess carrier density Δn is determined via inductive coupling to the coil of a WCT-120 lifetime tester (see Section 2.1.1). By calibrating the PL intensity to the excess carrier density Δn , spatially resolved lifetime measurements can be obtained from the PL images. The calibration procedure, which is described in detail by Herlufsen et al. [11], includes the photoconductance measurement of the silicon wafer at a steady-state illumination of the sample generating a constant excess carrier concentration with an effective lifetime according to Equation (2.9). The generation rate G for excess carriers is calculated by

$$G = \Phi(1 - R_{808\text{ nm}}) \frac{1}{W} , \quad (2.12)$$

with the reflectivity $R_{808\text{ nm}}$ and the photon flux of the excitation Φ . The photon flux of the excitation is measured by a calibrated Si solar cell and the value for reflectivity can be calculated e.g. on the PV Lighthouse website [12] for different types of passivated wafers. A PL calibration for a p -type $\text{Al}_2\text{O}_3/\text{SiN}_x$ -passivated Cz-Si lifetime sample is shown in Figure 2.6(a).

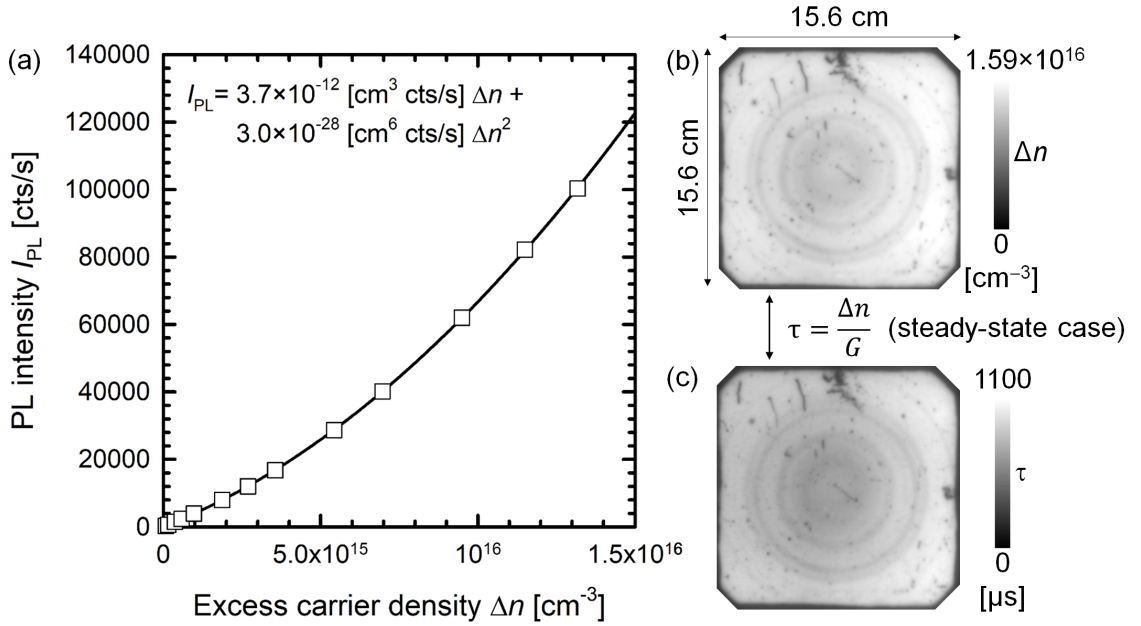


Figure 2.6: (a) PL-calibration for a p -type $\text{Al}_2\text{O}_3/\text{SiN}_x$ -passivated Cz-Si lifetime sample by different laser intensities between 0.009 and 0.9 suns in steady-state mode. (b) Spatially resolved excess carrier image and (c) spatially resolved carrier lifetime image at a laser intensity of 0.9 suns.

The PL signal I_{PL} as a function of the excess carrier density Δn can be described by a quadratic function on the basis of Equation (2.11): $I_{\text{PL}} = a\Delta n + b\Delta n^2$, which corresponds to the calibration function [11]. Thus, using the fit parameters the spatially resolved PL image can be converted into a spatially resolved excess carrier image (see Figure 2.6(b)), which has subsequently to be divided by the generation rate G (see Equation (2.9)) to obtain a spatially resolved carrier lifetime image (see Figure 2.6(c)).

In this work, also solar cells are characterized on the basis of luminescence detection using the EL setup shown in Figure 2.7. As shown in Figure 2.7(a), the front side of the solar cell is contacted by a copper wire centrally inserted into the window of the top brass plate. The rear side is fully contacted by a brass plate. Excess carriers are generated by applying a forward-bias voltage V_{appl} to solar cells in darkness, so that the resulting radiative recombination can be detected as a luminescence-signal with the intensity $\Phi_{i,\text{EL}}$ using a Si-CCD camera. Thereby, in addition the recombination properties, information about broken fingers (see Figure 2.7(b)) or locally increased series resistances can be obtained.

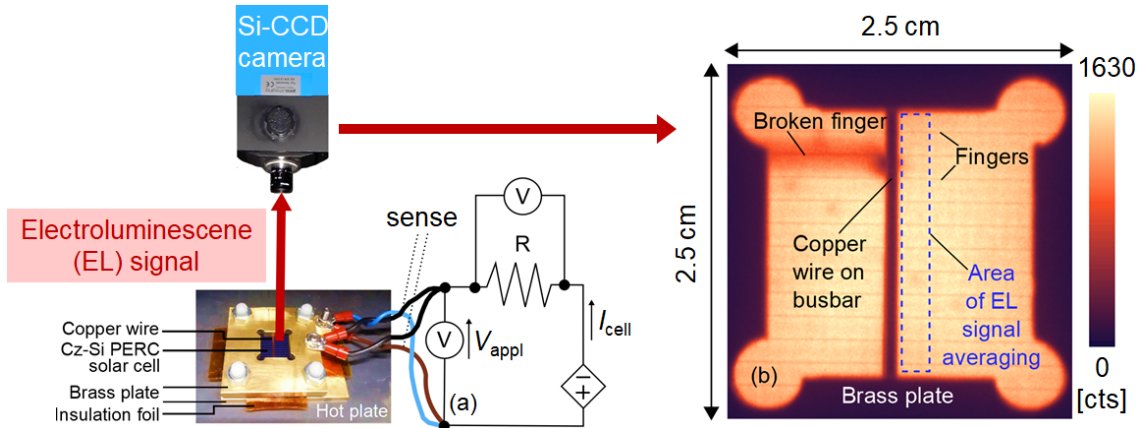


Figure 2.7: Schematic of the electroluminescence (EL) imaging setup for determination of the injected excess carrier concentration Δn . (b) EL image of a passivated emitter and rear cell (PERC) fabricated on a boron-doped p -type Cz-Si wafer.

With increasing V_{appl} , the measured EL-intensity $\Phi_{i,\text{EL}}$ increases due to a higher injected excess carrier concentration Δn and thus an increased radiative recombination. In general, near-infrared light is emitted from silicon-based solar cells, because silicon is a semiconductor with a band gap of about 1.12 eV (corresponds to $\lambda \approx 1150$ nm) at room temperature [13]. The determination of the excess carrier concentration via EL is described in detail in Section 4.4.

2.1.3 Fourier-Transform Infrared spectroscopy

In the case of Fourier-Transform Infrared (FTIR) spectroscopy, atomic bonds are getting in vibration by the absorption of light in the mid-infrared (MIR) range with a wavelength λ between 2.5 and 50 μm , corresponding to a wave number $\bar{\nu}$ between 4000 and 200 cm^{-1} . The different vibrational modes can be identified by detecting their characteristic absorption peaks.

Three characteristic absorption peaks of interstitial oxygen, due to bonding and vibrational modes with two adjacent silicon atoms, can be observed at $\bar{\nu}_1 = 1205$ cm^{-1} , $\bar{\nu}_2 = 1107$ cm^{-1} and $\bar{\nu}_3 = 515$ cm^{-1} . Because the absorbance at $\bar{\nu}_2 = 1107$ cm^{-1} is the strongest, the interstitial oxygen concentration $[\text{O}_i]$ in Cz-Si wafers is determined by FTIR measurements in a wave number range between 900 and 1200 cm^{-1} , using a *VERTEX 70* (Bruker) FTIR spectrometer in this work (see Figure 2.8(a)). In this setup, a globar (silicon carbide pin) emits light in the MIR range [14], which travels through an aperture and optical filter to an interferometer. A schematic of the

2.1 Characterization methods

basic working principle of the simplest form of an interferometer with flat mirrors is illustrated in Figure 2.8.

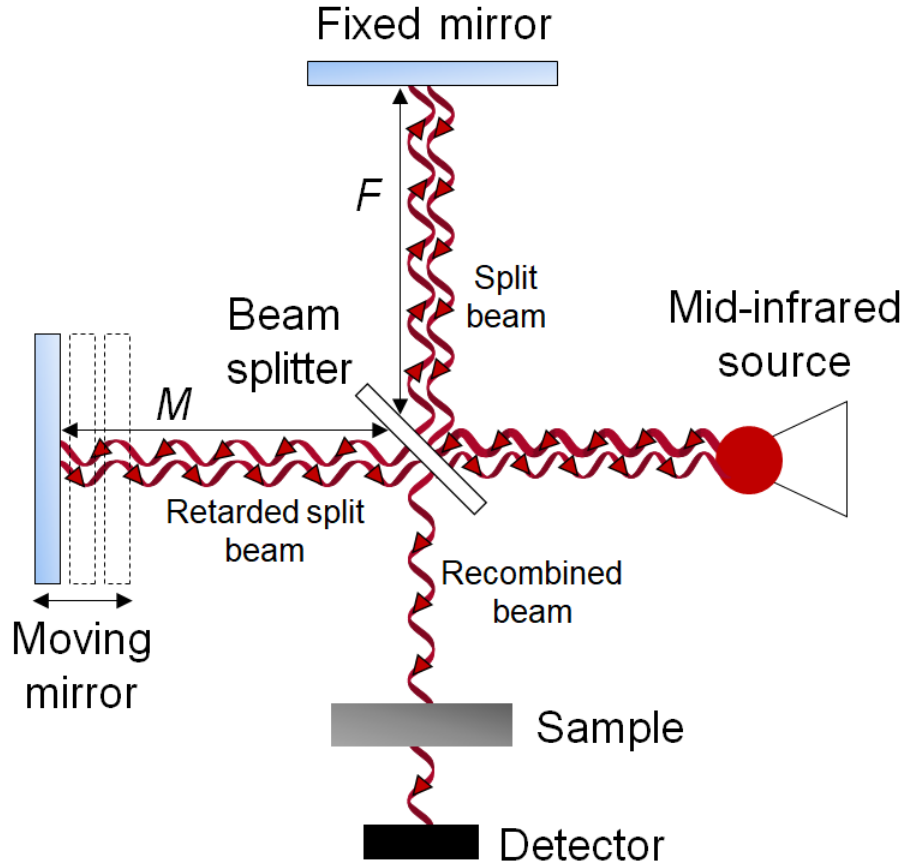


Figure 2.8: Schematic of the beam path and basic working principle within an interferometer.

Within the interferometer, the light beam is divided in two equal parts by a beam splitter, so that 50% of the light travels to a fixed mirror and the other 50% to a moving mirror. The light returning from both mirrors with the phase path length F and M recombines again at the beam splitter and is directed one half each to the sample with a detector behind and to the light source. All in all, there are two limiting cases. If both mirrors have the same distance to the beam splitter, then the light beams are in phase (constructive interference) and the resulting amplitude of the interferogram signal is maximal [15]. If the moveable mirror has a distance of $\lambda/4$, the light beams are in opposite phase (destructive interference) and the amplitude of the interferogram signal becomes zero [15]. Plotting the radiated signal versus the retardation $\delta (= 2(M - F))$ results in a so-called interferogram with a cosine function in the simplest case of mono-frequent radiation (monochromatic light). The relation between the optical frequency ν , or rather the wave number $\bar{\nu}$ with $\bar{\nu} = \nu/c = 1/\lambda$, and the frequency of the interferogram f can be described by

$$f = \frac{2v_M}{c} \nu = 2v_M \bar{\nu} = \frac{2v_M}{\lambda} \quad , \quad (2.13)$$

with the velocity of the movable mirror v_M and the velocity of light c (3×10^{10} cm/s) [15]. Thus, by moving the mirror with a constant velocity v_M , different frequencies

f can be realized in the case of light of different wavelengths λ (i.e. in the mid-infrared range), resulting in an interferogram as a sum of the interferograms at each wavelength. The sample interacts by absorption with this modulated light beam influencing the amplitude of the interferogram signal, which can be converted by applying a Fourier transformation and by comparison to a reference measurement without a sample in the beam path in a transmission spectrum.

The evaluation of the measured oxygen-related absorption peak at $\bar{\nu}_2 = 1107 \text{ cm}^{-1}$ with a resolution of 8 cm^{-1} , shown in Figure 2.9, was performed in accordance with the German standard DIN-50438-1 for polished samples with an etched rear side.

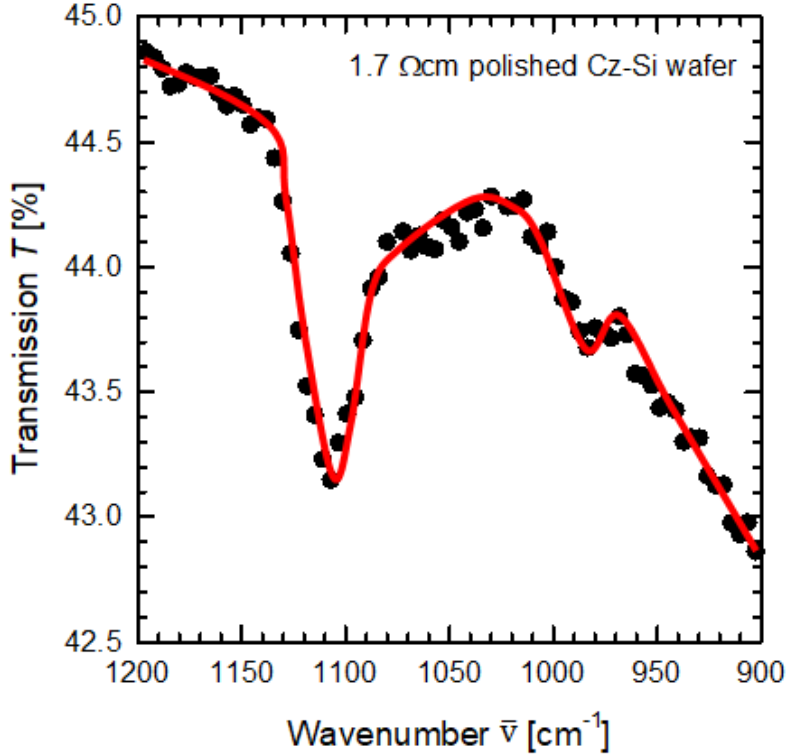


Figure 2.9: Measured transmission T due to Si–O–Si vibration modes in dependence on the wave number $\bar{\nu}$ of a polished Cz-Si wafer.

The Cz-Si samples in this work were chemically polished by a so-called CP4-etchant, which contains a solution of pure acetic acid (98.99%), hydrofluoric acid (40%) and nitric acid (69%) in the ratio 1:1:6. The obtained spectra of the Cz-Si samples and an oxygen-free reference sample, i.e. Fz-Si, are aligned according to method B of DIN-50438-1, so that the interstitial oxygen concentration $[O_i]$ can be calculated based on Beer's law by

$$[O_i] = K \times \alpha_O [\text{cm}^{-3}] \quad , \quad (2.14)$$

with the calibration constant K (see Table 2.1) and the absorption coefficient of oxygen α_O , which is given by

$$\alpha_O = \frac{-\ln(A + \sqrt{A^2 + B^2})}{W} \quad , \quad (2.15)$$

with $A = T_B(1 - B^2)/2T_M$ with the reference value of the baseline T_B and the minimal value T_M of the comparison spectrum and $B = (1/R) \times \exp(\alpha_B W)$ with

2.1 Characterization methods

the reflectance R about 0.3 for silicon in the examined wave number range. The comparison spectrum is obtained by the division of the transmittance spectra $\theta(\bar{\nu})$ of the sample and the reference sample: $\theta_s(\bar{\nu})/\theta_r(\bar{\nu})$. The absorption coefficient α_B is defined as

$$\alpha_B = \frac{-\ln(D + \sqrt{D^2 + 1/R^2})}{W} , \quad (2.16)$$

with $D = -(1 - R)^2/2\theta_R R^2$, which includes the transmittance of the aligned reference sample's spectrum θ_R . If the reference sample and the Cz-Si sample have a differing carrier concentration (ΔN), or rather doping concentration N_A , the absorption coefficient of oxygen α_O has to be corrected additionally according to

$$\alpha_O(\Delta N) = \alpha_O(1 - W(\alpha_{Ns} - \alpha_{Nr})) , \quad (2.17)$$

with the absorption coefficient of the free carriers of the reference sample α_{Nr} and of the Cz-Si sample α_{Ns} , which can be calculated by $1.43 \times 10^{-16} \times N_A + 0.85$. Finally, the temperature dependence of α_O is considered according to Equations (18) and (23) in DIN-50438-1.

Besides the interstitial oxygen concentration, the total hydrogen concentration $[H]$ within the silicon nitride layers is obtained from FTIR measurements in this work (see Section 5.4) according to

$$[H] = [Si - H] + [N - H] , \quad (2.18)$$

with the concentration of Si – H and N – H bonds, neglecting the concentration of hydrogen-hydrogen bonds (H – H) based on the study from Bredemeier et al. [16]. Hydrogen molecules are weakly IR-active in boron-doped material and could only be detected by IR absorption spectroscopy measurements of specific long-path-length samples (≈ 17 mm) at 10 K [17]. Thus these characteristic absorption peaks are not observed within our FTIR measurements at room temperature. However, two characteristic absorption peaks of hydrogen can be observed at $\bar{\nu}_1 = 3320 \text{ cm}^{-1}$ corresponding to N–H bonds and at $\bar{\nu}_2 = 2180 \text{ cm}^{-1}$ corresponding to Si–H bonds. The strongest absorbance is at $\bar{\nu}_3 = 880 \text{ cm}^{-1}$ within silicon nitride layers corresponding to Si–N bonds. An exemplary transmission spectra of a symmetrically passivated Fz-Si sample by single layers of silicon nitride with a refractive index of $n = 2.3$ is shown in Figure 2.10.

The evaluation of the measured characteristic absorption peaks of the different atomic bonds and the transformation in a concentration, generalized as $[X - Y]$, is performed by

$$[X - Y] = K(X - Y) \times \int_{\bar{\nu}_{\text{lower}}}^{\bar{\nu}_{\text{upper}}} \alpha(\bar{\nu}) d\bar{\nu} , \quad (2.19)$$

with the calibration constant K , the absorption peak area between the wave numbers $\bar{\nu}_{\text{lower}}$ and $\bar{\nu}_{\text{upper}}$ and the absorption coefficient α [18].

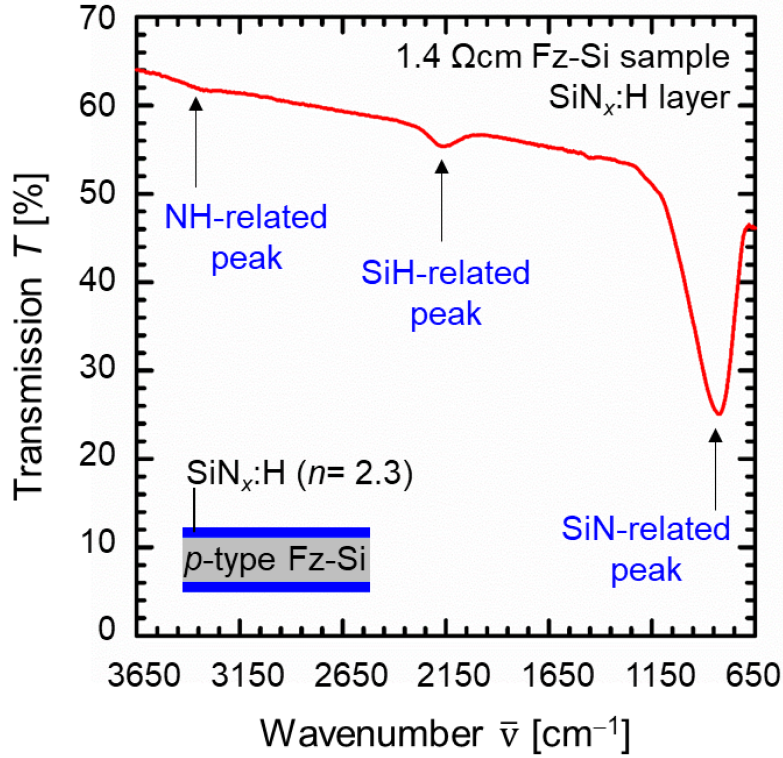


Figure 2.10: Measured transmission T due to N–H, Si–H and Si–N vibration modes in dependence on the wave number $\bar{\nu}$ of a symmetrically passivated Fz-Si sample by single layers of $\text{SiN}_x\text{:H}$ with a refractive index of $n = 2.3$.

The absorption coefficient α is calculated from the measured transmission T including a correction by the baseline

$$\alpha = \frac{-\log_{10}(T)}{\log_{10}(e) \times t} \approx 2.3026 \frac{-\log_{10}(T)}{t}, \quad (2.20)$$

with the total layer thickness t from the front and back side of the measured sample. The used calibration constants in this work are summarized in the following table.

Table 2.1: Calibration constants from Yin and Smith [18] for the characteristic absorption peaks of the different atomic bonds within the silicon nitride layers and from IOC88 standard for the characteristic oxygen absorption peaks.

Atomic bond	Calibration constant K [cm^{-1}]
Si–N	2.1×10^{16}
Si–H	5.9×10^{16}
N–H	8.2×10^{16}
Si–O–Si	3.14×10^{17}

The hydrogen loss $[\text{H}]_{\text{loss}}$ of the hydrogen-rich silicon nitride layers is analyzed by FTIR measurements before and after rapid thermal annealing (RTA) of $5 \times 5 \text{ cm}^2$ sister samples, which were processed identically to the $2.5 \times 2.5 \text{ cm}^2$ lifetime samples (see Chapter 5):

$$[\text{H}]_{\text{loss}} = [\text{H}]_{\text{before firing}} - [\text{H}]_{\text{after firing}}. \quad (2.21)$$

2.1 Characterization methods

According to Equation (2.21) the concentration loss of Si – H and N – H due to firing is calculated and described by a percentage loss c in relation to the hydrogen concentration before firing $[H]_{\text{before firing}}$:

$$c = \frac{[X - Y]_{\text{loss}}}{[H]_{\text{before firing}}} \times 100 \text{ [\%]} . \quad (2.22)$$

The different atomic bonds Si – H and N – H are generalized as $[X - Y]$ in Equation (2.22), which is valid for each of them.

The concentration loss of Si – N due to firing is calculated and described by a percentage loss $[\text{Si} - \text{N}]_{\text{loss}}$ in relation to the Si – N concentration before firing $[\text{Si} - \text{N}]_{\text{before firing}}$:

$$[\text{Si} - \text{N}]_{\text{loss}} = \frac{[\text{Si} - \text{N}]_{\text{before firing}} - [\text{Si} - \text{N}]_{\text{after firing}}}{[\text{Si} - \text{N}]_{\text{before firing}}} \times 100 \text{ [\%]} . \quad (2.23)$$

2.1.4 Resistivity measurements

The hydrogen concentration in the silicon bulk is determined via resistivity measurements (see Section 5.3) in this work. We measure the resistivities using the eddy-current method by inductive coupling the sample to a WCT-120 bridge from Sinton Instruments. The sample temperature is recorded during each measurement and the resistivities are extrapolated to 25 °C.

The sample conductance (see Equation (2.1)) is correlated to the voltage V by calibration wafers, as illustrated in Figure 2.11 with a linear calibration curve

$$\sigma = A \times V , \quad (2.24)$$

assuming sufficiently low σ values (< 0.2 Siemens). The prefactor A is determined and checked by regular calibration procedures. The calibration wafer with the lowest doping concentration has a conductance of 0.0019 Siemens, whereas the calibration wafer with the highest doping concentration has a conductance of 0.1728 Siemens, resulting in a relevant voltage range from 0.06 V to 5.45 V for our resistivity measurements.

By knowing the proportionality factor A and the wafer thickness W , the specific bulk resistivity $\rho_{\vartheta_{\text{meas}}}$ at the measured sample temperature ϑ_{meas} is calculated by

$$\rho_{\vartheta_{\text{meas}}} [\Omega\text{cm}] = \frac{W [\text{cm}]}{V [\text{V}] \times A \left[\frac{1}{\text{V}\Omega} \right]} = \frac{W [\text{cm}]}{\sigma \left[\frac{1}{\Omega} \right]} , \quad (2.25)$$

with the SI-unit Siemens of the sample conductance σ being the reciprocal Ohm. Finally, the specific bulk resistivity ρ is extrapolated to 25 °C according to

$$\rho = (1 - 0.00722 \left[\frac{1}{^\circ\text{C}} \right] \times (\vartheta_{\text{meas}} [^\circ\text{C}] - 25 [^\circ\text{C}])) \times \rho_{\vartheta_{\text{meas}}} [\Omega\text{cm}] , \quad (2.26)$$

with $0.00722 \text{ 1/}^\circ\text{C}$ being the temperature coefficient for p -type silicon. Thereby, all values of a measured resistivity evolution during dark annealing on a hotplate can be compared. In contrast to the carrier lifetime measurements (see Section 2.1.1), the output voltage of the resonant circuit is directly measured by a precision multimeter (8845A, Fluke) for resistivity measurements.

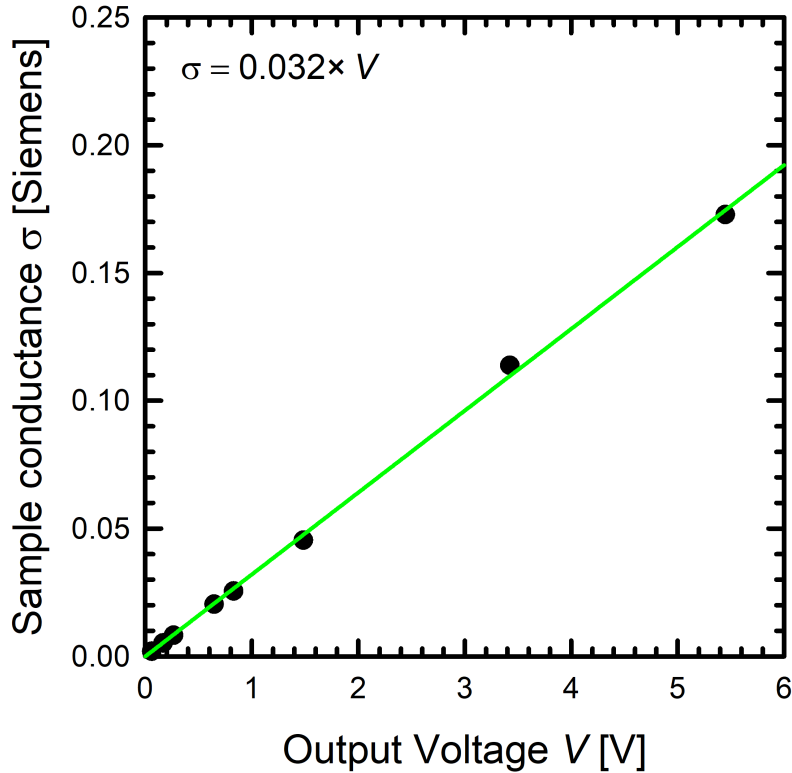


Figure 2.11: Calibration of the coil for resistivity measurements in the experimental setup of the WCT-120 System from Sinton Instruments by different calibration wafers with a different doping concentration or rather conductance. The $\sigma(V)$ dependence is linear for sufficiently low σ values (< 0.2 Siemens).

Bredemeier et al. [19] showed by resistivity measurements that in dependence on the refractive index n and thickness d of the silicon nitride layers, different amounts of hydrogen are introduced into the silicon bulk. Thus, these optical properties of the layers should be characterized during processing as an important parameter within the hydrogen experiments in this work.

2.1.5 Ellipsometry

The refractive index n and thickness d of dielectric layers are determined via spectroscopic ellipsometry using a Woollam M-2000UI ellipsometer. The light source is a halogen lamp, followed by a polarizer, the sample, a rotating compensator (which is a retarder), an analyzer for determining the polarization of the reflected light and a Si-CCD and InGaAs detector. The basic measurement principle of ellipsometry is schematically illustrated in Figure 2.12. In this thesis, we use Fz-Si samples coated with single silicon nitride (SiN_x) layers or $\text{Al}_2\text{O}_3/\text{SiN}_x$ stacks. In Section 2.2, the deposition methods for these dielectric layers are described in more detail.

As can be seen in Figure 2.12, light is irradiated oblique at an incidence angle θ on an interface of optically different media, i.e. an air/coated c-Si interface in this work. According to Maxwell's equations, light can be described as an electromagnetic wave with an electric field component E_f , which can be oriented or rather *polarized* in specific directions. In the case of spectroscopic ellipsometry based on light reflection, the light waves are p-polarized with a parallel and s-polarized with

2.1 Characterization methods

a perpendicular oscillatory direction of the electric field to the incident plane [20].

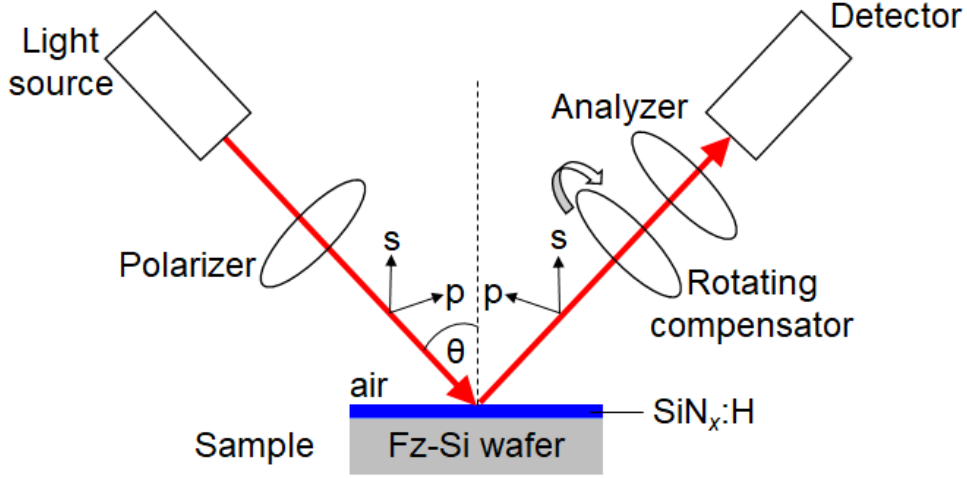


Figure 2.12: Schematic of the basic measurement principle of ellipsometry in accordance with the used Woollam M-2000UI ellipsometry tool in this work.

In general, the electric field of a one-dimensional wave can be described as

$$E = E_0 \exp[i(\omega t - K_{\text{prop}}x + \delta)] \quad , \quad (2.27)$$

with the amplitude E_0 , the imaginary number i , the angular frequency ω , the time t , the propagation number $K_{\text{prop}} (= 2\pi/\lambda)$, the distance or rather position x and the initial phase δ . The propagation number depends on the velocity of the wave s according to

$$K_{\text{prop}} = \frac{\omega}{s} \quad . \quad (2.28)$$

Thus, the phase shows a large change upon light reflection, because the propagation of light waves changes characterized by the refractive index n according to

$$n(\lambda) \equiv \frac{c_{\text{light}}}{s} \rightarrow K_{\text{prop}} = \frac{\omega n}{c_{\text{light}}} \quad , \quad (2.29)$$

with s being the speed of light in a medium and c_{light} being the speed of light in vacuum ($c_{\text{light}} = 2.998 \times 10^8 \text{ m/s}$). In a medium with a high refractive index n , the propagation of light waves becomes slower [21]. The influence of the refractive index n on the amplitude (detailed description in [21], pp. 35) is defined over the amplitude reflection coefficient.

The phase and amplitude changes of the p- and s-polarized waves upon light reflection depends on the refractive index n , the extinction coefficient (not discussed in detail here) and the film thickness of the sample [20, 21]. It can be described by the total change in the polarization state ρ due to superposition of the reflected polarized light waves

$$\rho \equiv \frac{r_p(\theta)}{r_s(\theta)} \equiv \tan(\Psi(\theta)) \times e^{i\Delta(\theta)} \equiv \left(\frac{E_{f,rp}}{E_{f,ip}} \right) / \left(\frac{E_{f,rs}}{E_{f,is}} \right) \quad (2.30)$$

by the ratio of amplitude reflection coefficients of p-polarized $r_p(\theta)$ and s-polarized light $r_s(\theta)$, including the amplitude ratio $\Psi(\theta)$ and the phase difference $\Delta(\theta)$ between

the p- and s-polarization. The electric field vectors of incident p- and s-polarizations are defined as $E_{f,rp}$ and $E_{f,rs}$, whereas $E_{f,ip}$ and $E_{f,is}$ are of the reflected light waves. In Figure 2.13, typical ellipsometry measurement data at the so-called Brewster angle of an Fz-Si sample with an $\text{Al}_2\text{O}_3/\text{SiN}_x$ stack are shown.

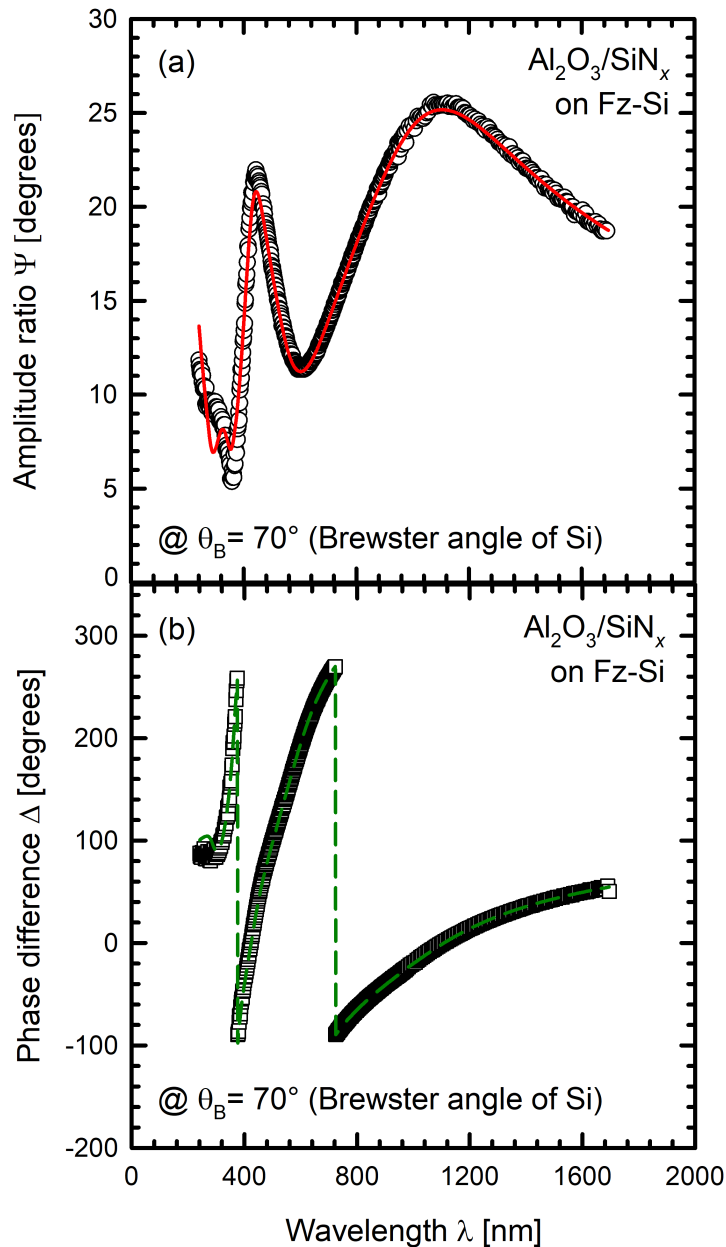


Figure 2.13: Exemplary ellipsometry measurement data: (a) amplitude ratio Ψ and (b) phase difference Δ as shown symbols, which are fitted (solid lines) using optical models. The measurement was performed at the Brewster angle of silicon ($\theta_B = 70^\circ$).

Ellipsometry measurements are usually performed at the Brewster angle θ_B as incidence angle onto the sample ($\theta_B(\text{Si}) = 70^\circ$), where the difference between r_p and r_s is maximized [21]. Additionally, in spectroscopic ellipsometry, $\Psi(\theta)$ and $\Delta(\theta)$ values are acquired as a function of wavelength, increasing the information content in the data set [22]. Using an optical model, which describes the sample as a layered structure (substrate, film 1, film 2 etc.), for a fit of the ellipsometry measurement

2.2 Sample preparation methods

data for Ψ and Δ , the thickness of the thin film d and the wavelength-dependent refractive index n as well as the extinction coefficient k (see Figure 2.14) of the investigated sample's structure can be analyzed. Each layer of the sample's structure has different optical properties within the model. In this work, we used the WVASE32 software (J. A. Woollam) for the evaluation of the measurement data, which has implemented different types of oscillators and physically based film equations (Snell's law, Fresnel equations, etc.) for fitting [22]. The model generated data adequately fits the measured data in Figure 2.13. The SiN_x layer is assumed to be a transparent film within the model. However, it becomes absorbing toward shorter wavelengths (240-400 nm) observed by an increasing extinction coefficient k toward shorter wavelengths (see Figure 2.14), which is why the model doesn't fit the data set in this wavelength range. The optical constants have a physical shape [22].

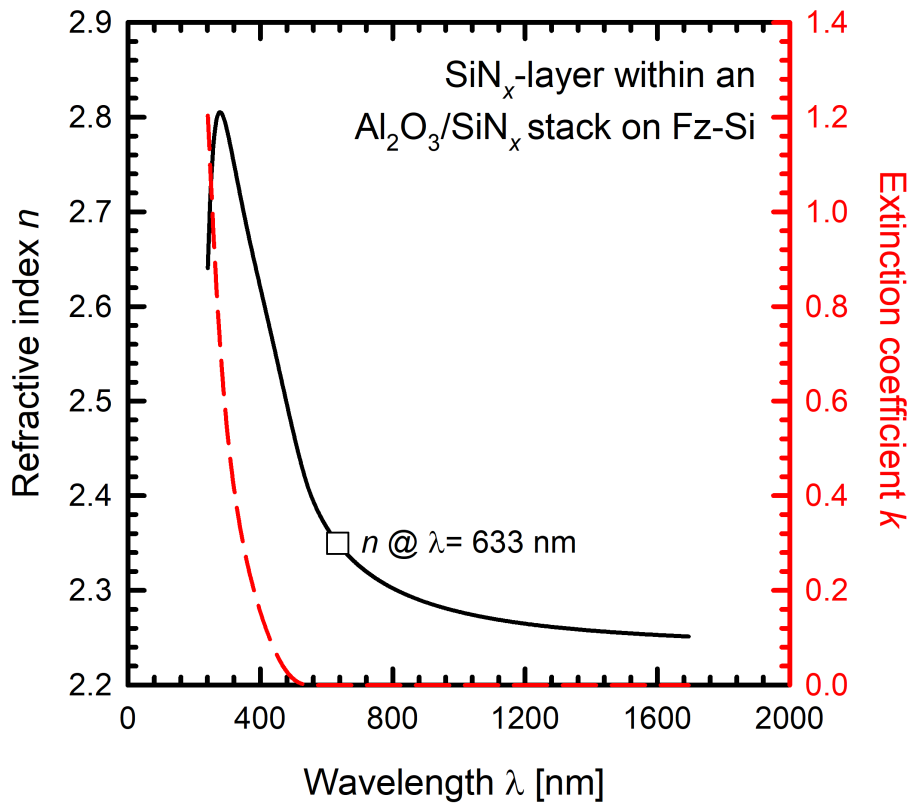


Figure 2.14: Refractive index n (solid line, corresponding to left y-axis) and extinction coefficient k (dashed line, corresponding to right x-axis) as a function of the wavelength λ obtained from fits of the ellipsometry measurement data using a model including optical properties of a $\text{Al}_2\text{O}_3/\text{SiN}_x$ stack of layers. The SiN_x layer shows a refractive index n of 2.35 for light with a wavelength λ of 633 nm (open square).

The SiN_x layer shows a refractive index n of 2.35 for light with a wavelength λ of 633 nm (the wavelength of a HeNe laser).

2.2 Sample preparation methods

Silicon lifetime samples are typically coated by aluminum oxide (Al_2O_3) and silicon nitride (SiN_x) layers to minimize surface recombination. In this work, the Al_2O_3 lay-

ers are deposited by means of plasma-assisted atomic layer deposition (PA-ALD) and the SiN_x layers by means of plasma-enhanced chemical vapor deposition (PECVD). Before surface passivation, the silicon samples receive a chemical cleaning step, also called RCA cleaning [23], in two different chemical solutions: SC-1 and SC-2. The SC-1 mixture contains ammonia (25%), hydrogen peroxide (30%) and deionized water at a ratio of 1:1:5 to remove particles and organic contaminants from the silicon surface. The SC-2 mixture contains hydrochloric acid (37%), hydrogen peroxide (30%) and deionized water in the ratio of 1:1:6 to remove metallic inorganic contaminants from the silicon surface. The silicon samples are typically treated for 10 min in each solution at a temperature between 75 and 80 °C [23] followed by a short dip (≈ 2 min) in hydrofluoric acid (1%) to remove the formed thin silicon oxide layer together with the contaminants. After each step, the silicon samples are rinsed in deionized water for 5 min, so that the silicon surface is saturated by silanol groups (Si-OH) in equilibrium with adsorbed water at the end [24]. If the samples are kept in open air for too long, the free hydroxyl groups on the silicon surface decrease rapidly and a native silicon oxide layer is formed [25]. Therefore, the RCA cleaning should be performed immediately prior to deposition of the dielectric passivation layers.

2.2.1 Atomic layer deposition

Al_2O_3 layers are deposited by means of plasma-assisted atomic layer deposition (PA-ALD) using a FlexALTM system (Oxford Instruments), as shown in Figure 2.15(a). The silicon wafers are transferred by a quartz carrier onto a heating stage with a temperature of about 200 °C in an evacuated deposition chamber.

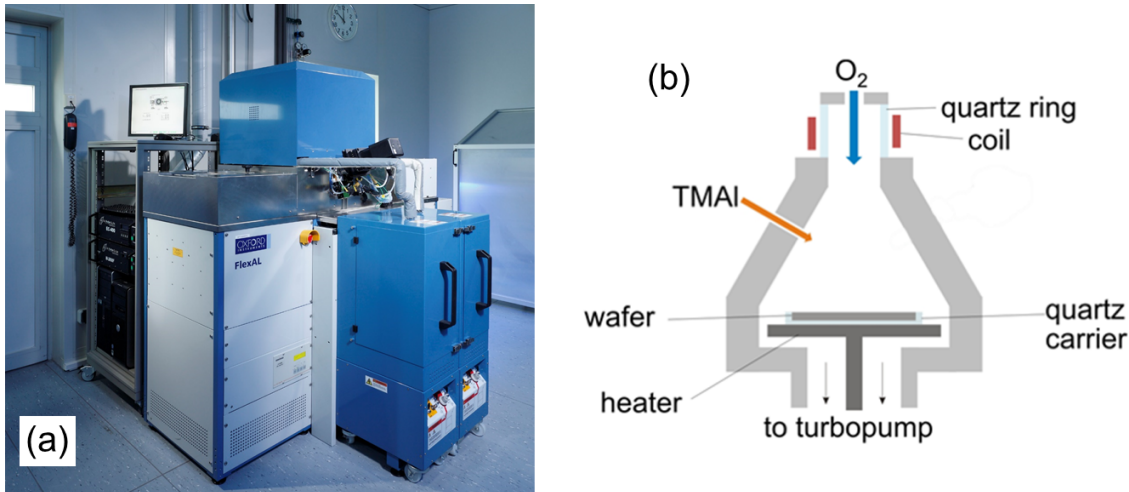
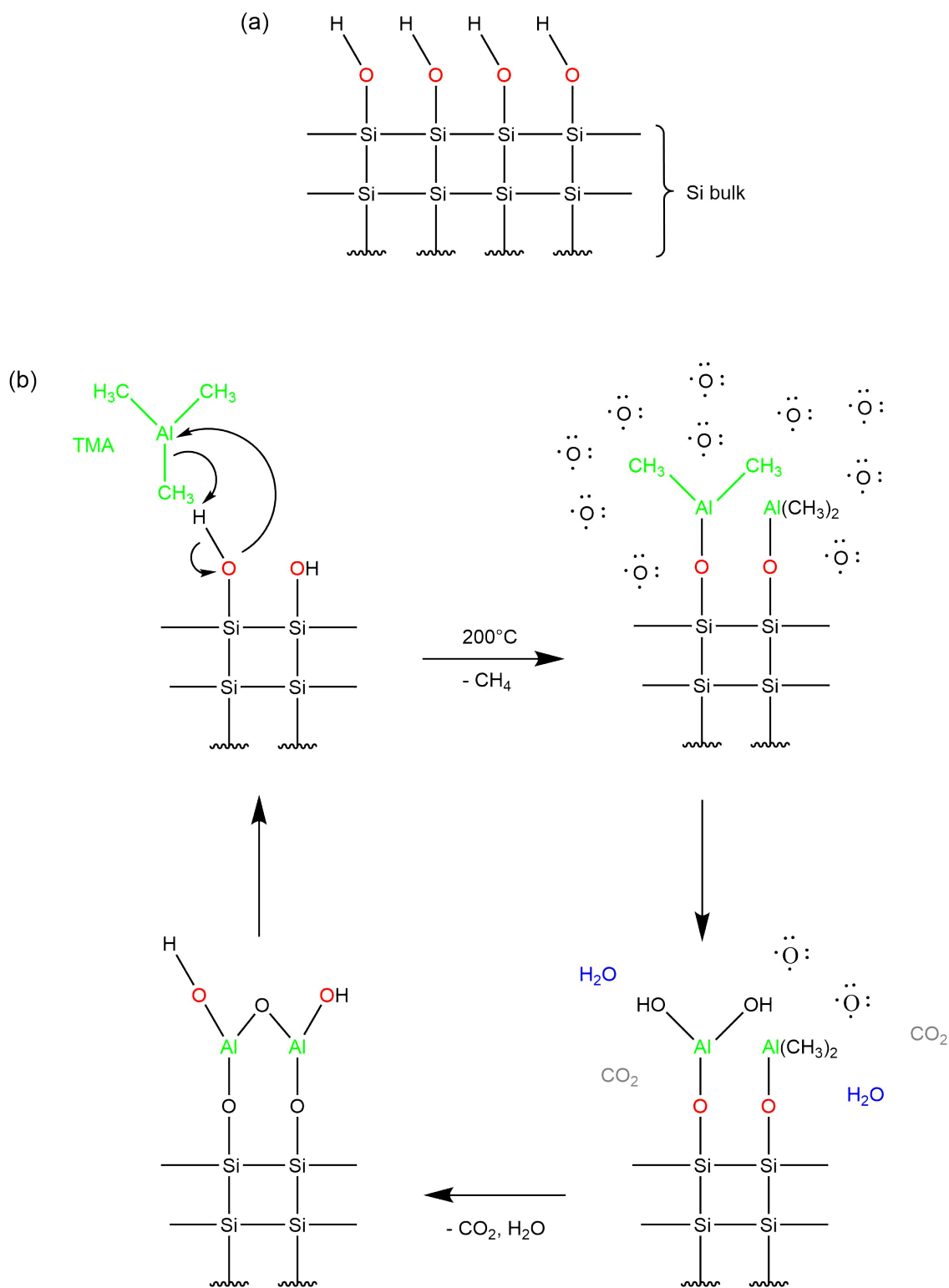


Figure 2.15: (a) FlexALTM (Oxford Instruments) for atomic layer deposition of Al_2O_3 used throughout this work. (b) Schematic of the ALD deposition chamber, taken from [26].

As precursor, trimethylaluminum (TMA) and atomic oxygen, generated by an oxygen plasma, are injected into the deposition chamber (see Figure 2.15(b)) in one of the two half-cycles, which are schematically illustrated in Figure 2.16.

2.2 Sample preparation methods



Starting with a hydroxyl-terminated silicon surface directly after RCA cleaning,

the first precursor gas TMA is introduced into the deposition chamber. The TMA molecules react with the hydroxyl-groups under elimination of methane until the silicon surface is saturated by methylaluminium groups ($\text{Si-Al}(\text{CH}_3)_2$). The remaining TMA molecules are removed by purging with O_2 . This is the first half-cycle. In the second half-cycle, atomic oxygen, produced in an inductively coupled plasma (ICP) directly above the sample surface, is introduced into the deposition chamber, which reacts with the methylaluminium groups by replacing the methyl groups and forming carbon dioxide (CO_2) and water (H_2O). After complete oxidation of the aluminum, the residual gas and the chemical byproducts are purged out again by an oxygen gas flow leaving a hydroxyl-terminated aluminum oxide monolayer for the next deposition cycle. In this thesis, by varying the number of cycles between 42 and 209, the Al_2O_3 thickness was adjusted between 5 and 25 nm to systematically examine the impact of the Al_2O_3 thickness on the hydrogen diffusion into the silicon bulk during an RTA step (see Section 5.5).

The Al_2O_3 layers deposited by PA-ALD are stoichiometric ($[\text{O}]/[\text{Al}] = 1.5$) in composition and contain about 1-2 at% hydrogen [27, 28], mainly incorporated as OH groups [28]. Based on thermal effusion measurements using mass spectrometry (MS), Dingemans et al. [29] proposed the formation of hydrogen within the aluminum oxide layer during annealing due to reactions of the hydroxyl-groups with Al atoms forming Al-O bonds. In addition, H_2O was detected by MS during annealing due to an assumed reaction of two hydroxyl groups in close vicinity [29]. However, atomic hydrogen cannot be analyzed directly by this method, only indirectly as H_2 molecules after recombination at the surface, the film-substrate interface or internal surfaces [29]. In Chapter 5, the hydrogen in-diffusion into the silicon bulk from hydrogen-rich silicon nitride layers and hydrogen-lean aluminum oxide layers is analyzed via resistivity measurements (see Section 2.1.4 and Section 5.3).

2.2.2 Plasma-enhanced chemical vapor deposition

Two different plasma-enhanced chemical vapor deposition (PECVD) tools were used for the deposition of SiN_x layers in this thesis. The $\text{SiN}_x\text{:H}$ layers deposited on $156 \times 156 \text{ mm}^2$ sized silicon wafers were processed in an industrial-type inline SINA system (see Figure 2.17(a)) from Meyer Burger Technology AG, whereas small samples ($2.49 \times 2.49 \text{ cm}^2$) were coated in a Plasmalab 80 Plus System (Oxford Instruments) as illustrated in Figure 2.17(b). Both tools are based on the principle of PECVD with a *remote* plasma. However, the SINA system is a dynamic deposition tool with a moving sample during deposition. In the SINA system, we use a gas mixture of silane (SiH_4), ammonia (NH_3) and hydrogen (H_2) for $\text{SiN}_x\text{:H}$ deposition. The Plasmalab 80 Plus System is a static deposition tool using silane (SiH_4), ammonia (NH_3) and nitrogen (N_2) as process gases.

Ammonia and hydrogen gases are injected into the processing chamber of the SINA system through the plasma zone. Within the Plasmalab 80 Plus system, ammonia and nitrogen pass the plasma zone (see Figure 2.17(b)). Thereby, different types of reactants are generated by the plasma in the different deposition tools. However, both systems use silane as a source of silicon. Within both tools, the plasma of reactive ammonia species (i.e. radicals) is excited by means of continuous-wave

2.2 Sample preparation methods

magnetron microwave generators ($f = 2.45$ GHz) introducing a microwave power in the gas mixture (microwave induced plasma). Subsequently, the excited NH_3 reactants are forming a $\text{SiN}_x\text{:H}$ layer on the silicon surface with the silane gas in the processing chamber.

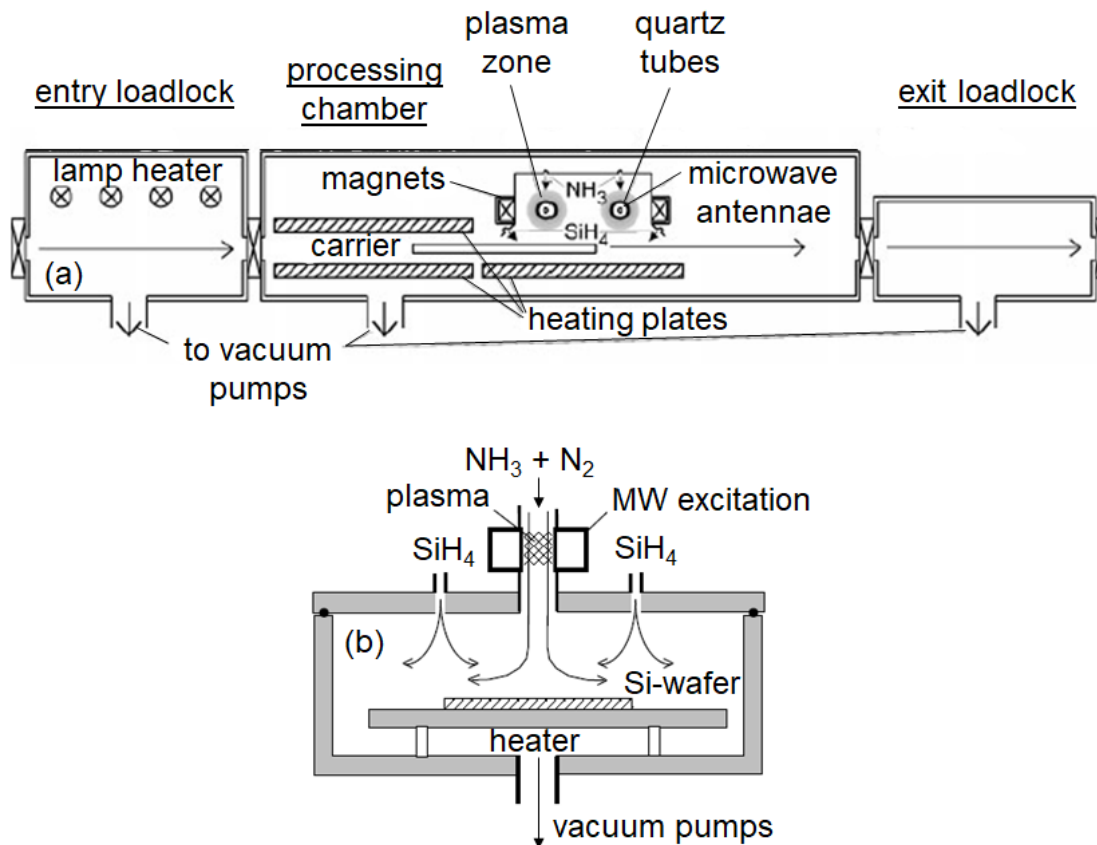


Figure 2.17: (a) Schematic of the inline PECVD SiNA system from Meyer Burger Technology AG, taken from [30], used for silicon nitride deposition on $156 \times 156 \text{ mm}^2$ sized silicon wafers. (b) Schematic of the remote-PECVD reactor of the Plasmalab 80 Plus system, taken from [31], used for silicon nitride deposition on smaller silicon samples.

The adjusted deposition parameters in this work are summarized in detail in Table 2.2. All $\text{SiN}_x\text{:H}$ films on the small samples processed in this work had the same thickness of about 130 nm by adjusting the deposition time and all $\text{SiN}_x\text{:H}$ films on the $156 \times 156 \text{ mm}^2$ sized wafers had a thickness of about 70 nm by adjusting the carrier velocity. The thickness d and the refractive indices n of the deposited layers were measured by ellipsometry (see Section 2.1.5). Silicon nitride layers with a refractive index $n = 1.9$ (at a wavelength of $\lambda = 633 \text{ nm}$) are stoichiometric in composition (i.e. $[\text{Si}]/[\text{N}] = 3/4 = 0.75$) and the higher the refractive index, the silicon-richer ($0.75 < [\text{Si}]/[\text{N}] \leq 2.5$) the SiN_x film is.

PECVD $\text{SiN}_x\text{:H}$ films are amorphous and contain a lot of hydrogen [32], about 16-18 at% hydrogen for the $\text{SiN}_x\text{:H}$ layers deposited in this work. In general, PECVD $\text{SiN}_x\text{:H}$ can contain up to 39 at% of hydrogen [33]. Hydrogen is present in the form of Si-H and N-H bonds or interstitially at Si-Si bonds within the $\text{SiN}_x\text{:H}$ network [32].

Until now, only the hydrogen effusion of $\text{SiN}_x\text{:H}$ layers during annealing was investigated by Fourier Transform Infrared (FTIR) spectroscopy and mass spectrometry (MS) measurements [34–36]. These experiments showed a hydrogen loss due to the formation of molecular hydrogen (H_2), which is explained by Si–H bonds breaking and the diffusion of atomic hydrogen [37].

Table 2.2: Silicon nitride set deposition parameters of the two different tools used in this thesis.

Parameter	SiNA	Plasmalab 80 Plus		
NH_3 gas flow [sccm]	200	200		
N_2 gas flow [sccm]	–	100		
H_2 gas flow [sccm]	100	–		
SiH_4 gas flow [sccm]	114	1.2	8.5	15
Refractive index n (at $\lambda = 633$ nm)	2.05	1.9	2.3	2.7
Deposition time [min]	–	11:25	6:12	5:30
Carrier velocity [cm/min]	39	–		
Layer thickness d [nm]	70	130		
Chamber pressure [bar]	2×10^{-4}	2×10^{-4}		
Microwave power [W]	1200	150		
Set deposition temperature [$^\circ\text{C}$]	500	400		

By varying the refractive index n of the $\text{SiN}_x\text{:H}$ layers, the impact of the $\text{SiN}_x\text{:H}$ composition on the hydrogen diffusion into the silicon bulk during an RTA firing step was examined in this work (see Section 5.4).

3 Review of boron-oxygen-related light-induced degradation and regeneration in crystalline silicon

In this chapter, we present the state-of-the-art of research on the light-induced boron-oxygen defect center in silicon. The purpose is to provide a comprehensive overview of previous research activities prior to this work.

The chapter provides an overview of the activation and permanent deactivation of the boron-oxygen (BO) related recombination centre, which have to be considered when using Czochralski-grown silicon (Cz-Si) as bulk material for solar cells, as the activation of the BO defect center significantly reduces the carrier lifetime and thus the efficiency of solar cells during operation.

3.1 Boron-oxygen-related carrier lifetime degradation

Lifetime samples (i.e. surface-passivated silicon samples) fabricated on boron-doped, oxygen-rich Czochralski-grown silicon (Cz-Si) as bulk material degrade in carrier lifetime during light exposure. High concentrations of oxygen in Cz-Si are due to the partial dissolution of the silica crucible during the Czochralski growth process. The oxygen interacts with the dopant boron to form a boron-oxygen complex. Typical interstitial oxygen concentrations in standard Cz-Si wafers are in the range of $(5 - 8) \times 10^{17} \text{ cm}^{-3}$ [2].

Fischer and Pschunder [38] were the first who observed the phenomenon of degradation under illumination of solar cell parameters in 1974, which is today frequently labeled “light-induced degradation” (LID). Others followed on investigating this LID effect of the carrier lifetime in boron-doped Cz-Si [1, 39–41]. It was shown that the degradation originates from the activation of a boron-oxygen (BO)-related defect center during excess carrier injection (e.g. by illumination) [1]. In Figure 3.1, we measured a typical lifetime evolution of an $1.1 \Omega\text{cm}$ boron-doped *p*-type Cz-Si sample with an $\text{Al}_2\text{O}_3/\text{SiN}_x$ -stack on both surfaces for their passivation is shown, which is illuminated by an intensity of $I_{\text{ill}} = 0.1 \text{ suns}$ ($10 \text{ mW}/\text{cm}^2$) near room temperature $[(25 \pm 3)^\circ\text{C}]$ and measured at an injection level of $\Delta n = 1 \times 10^{15} \text{ cm}^{-3}$.

It was shown by Bothe and Schmidt [41] that the lifetime degrades with a fast and slow stage of degradation. In our experiment shown in Figure 3.1, the illumination intensity is adjusted by a halogen lamp to the equivalent generated current density of one sun defined from the sun’s spectrum [42] using a calibrated reference silicon solar cell. The lifetime measurements (see Section 2.1.1) are performed using the WCT-120 measurement system from Sinton Instruments [7] in the PCD mode. It was also shown [1] that by annealing in darkness the boron-oxygen defect can be temporarily deactivated. Typical conditions for full deactivation are 200°C for 10 min in the dark

[1]. However, under illumination, the lifetime decreases again due to activation of the boron-oxygen defect [1]. The recombination-active defect centers are formed during the carrier injection in lifetime samples by illumination. In the case of solar cells (see Chapter 4), excess carriers can also be injected through the pn -junction by applying a forward-bias voltage. The degradation, either of lifetime or of open-circuit voltage, proceeds over a fast initial degradation and a slower second degradation stage to a minimum value [43].

The measured lifetimes can be transformed into an effective defect concentration N_t^* according to Equation (3.1), assuming that all other recombination channels remain unchanged upon illumination:

$$N_t^* \equiv \frac{1}{\tau(t)} - \frac{1}{\tau_0} . \quad (3.1)$$

By fitting the evolution of the effective defect concentration N_t^* using an exponential rise-to-maximum function, the light-induced lifetime degradation can be described by a degradation rate constant R_{deg} , also known as generation rate constant:

$$N_t^* = N_{t,\text{max}}^* [1 - \exp(-R_{\text{deg}} \times t)] , \quad (3.2)$$

with the maximum effective defect concentration $N_{t,\text{max}}^*$. Using this fit, the slow decay component of lifetime degradation $R_{\text{deg,slow}}$ ($\equiv R_{\text{deg}}$) is analyzed within this work. The initial fast decay component $R_{\text{deg,fast}}$, which is observed during the first few minutes under illumination at room temperature (first deviating data points from the fit in Figure 3.1(b)), can be described accordingly [43].

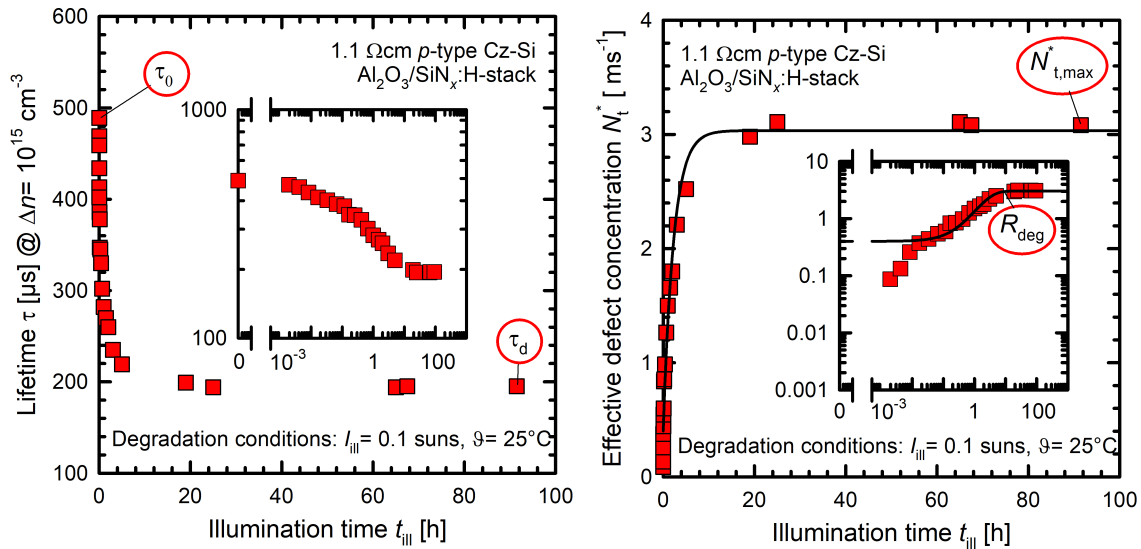


Figure 3.1: (a) Typical lifetime evolution of an 1.1 Ωcm boron-doped p -type Cz-Si sample with an $\text{Al}_2\text{O}_3/\text{SiN}_x$ -stack, which is illuminated by an illumination intensity of $I_{\text{ill}} = 0.1$ suns ($10 \text{ mW}/\text{cm}^2$) near room temperature ($(25 \pm 3)^\circ\text{C}$). The lifetime is measured at 30°C and analyzed at an excess carrier density of $\Delta n = 1 \times 10^{15} \text{ cm}^{-3}$. (b) Calculated effective defect concentration N_t^* from the measured lifetimes $\tau(t)$ and the lifetime τ_0 directly measured after annealing in darkness at 200°C . The N_t^* evolution with the maximum effective defect concentration $N_{t,\text{max}}^*$ can be described by an exponential rise-to-maximum function with one degradation rate constant R_{deg} .

3.1 Boron-oxygen-related carrier lifetime degradation

The slow degradation stage proceeds over hours under illumination at room temperature until the so-called degraded lifetime τ_d is reached as a minimum. The measured degradation curve in the given example in Figure 3.1 results in a degradation rate constant of $R_{\text{deg}} = 0.4 \text{ h}^{-1}$ for the slow-forming defect center and a maximum effective defect concentration of $N_{\text{t,max}}^* = 3.1 \text{ ms}^{-1}$.

In the following, some general influence parameters on the generation kinetics of the B-O defect center, or rather the lifetime degradation kinetics, are summarized, which have been established in literature prior to this work and are relevant for this work.

By performing time-resolved lifetime measurements on various Cz-Si materials with different boron concentrations and comparable oxygen concentrations under illumination at room temperature, Schmidt and Bothe [2, 41] (see Figure 3.2(a)) demonstrated a quadratic dependence of the defect generation rate, also known as the degradation rate constant R_{deg} , on the boron doping concentration N_{dop} , which was identical to the hole concentration p on the examined samples: $R_{\text{deg}} \propto p^2$. The effective defect concentration N_{t}^* in boron-only doped samples was furthermore shown to increase linearly with the boron doping concentration: $N_{\text{t}}^* \propto [\text{B}]$ [2, 41].

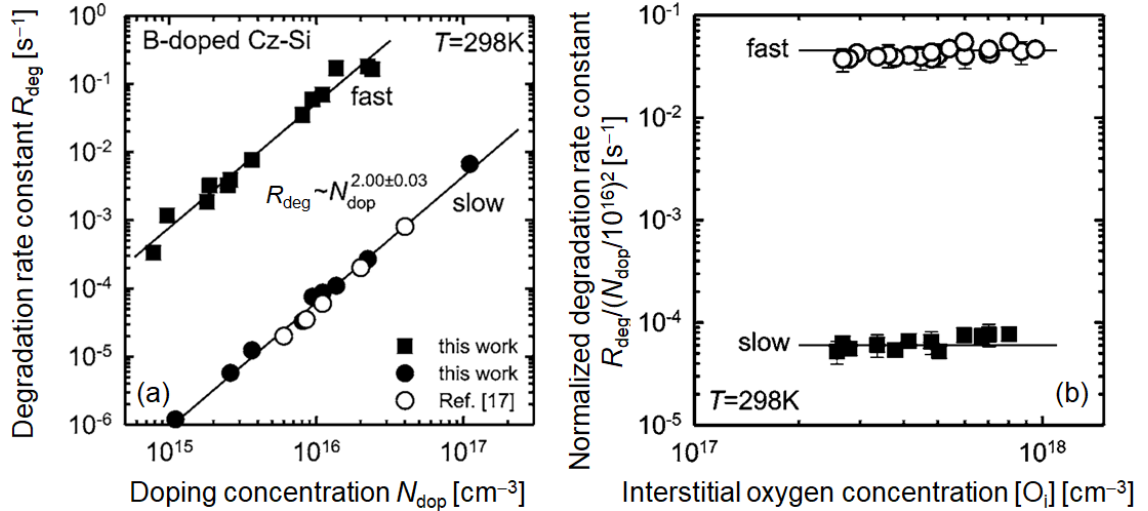


Figure 3.2: Degradation rate constant R_{deg} of the fast and the slow stages of degradation versus (a) the boron concentration N_{dop} and (b) the interstitial oxygen concentration $[\text{O}_i]$ according to Bothe and Schmidt [41].

Varying the oxygen concentration of the Cz-Si samples does not influence the degradation kinetics. As shown in Figure 3.2(b), the degradation rate constants of the fast and the slow degradation are independent of the interstitial oxygen concentration in the silicon [41, 44]. In addition, N_{t}^* increases quadratically with increasing interstitial oxygen concentration: $N_{\text{t}}^* \propto [\text{O}]^2$ [2, 41].

Macdonald et al. [45] and Lim et al. [46] showed that the effective defect concentration N_{t}^* of compensated p -type Cz-Si is proportional to the net doping concentration p_0 , which is given by $p_0 = N_{\text{A}} - N_{\text{D}}$, with N_{A} being the acceptor concentration (usually boron) and N_{D} being the donor concentration (usually phosphorus). The degra-

degradation rate in phosphorus-compensated Cz-Si samples was found to be dependent on the square of the net doping concentration p_0^2 rather than $p_0 \times N_A$ (as expected from the defect knowledge at that point in time), as shown in Figure 3.3.

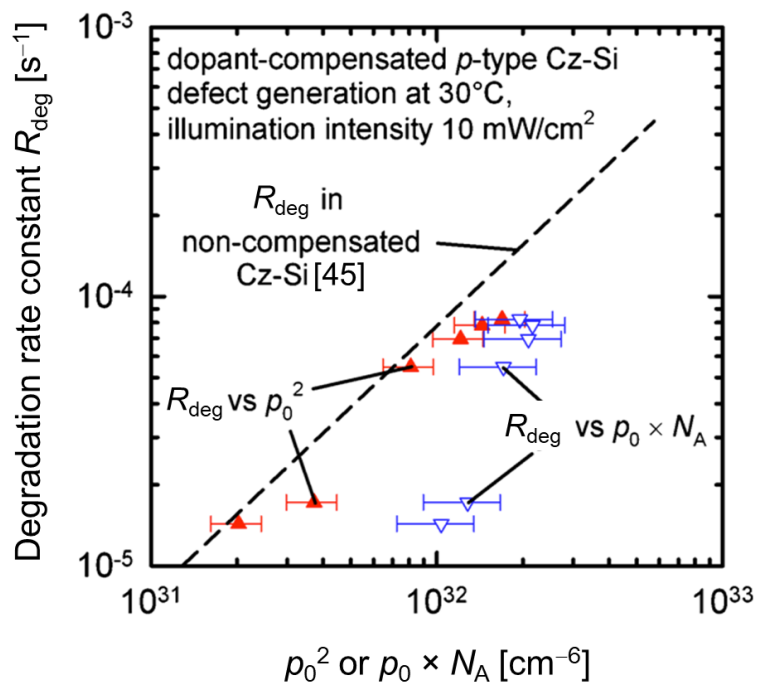


Figure 3.3: Degradation rate constant for non-compensated and dopant-compensated p -type Cz-Si samples in dependence on the square of net doping concentration p_0^2 and the product of the net doping and the total boron concentration $p_0 \times N_A$ according to Lim et al. [46].

Later it was shown [47] that the effective defect concentration N_t^* of non-compensated, but Cz-Si samples co-doped with B and Ga, is proportional to the boron concentration N_A and not on the net doping concentration p_0 .

In other studies it was shown that high-temperature processes as typical oxidation or phosphorus diffusion processes can decrease N_t^* significantly in uncompensated Cz-Si samples [39, 40, 48] and increase the degraded lifetime τ_d [49].

As already mentioned, the boron-oxygen defect can temporarily be deactivated or rather the effective defect concentration can be temporarily reduced in boron-doped p -type Cz-Si by a short dark-annealing step. In general, the defect deactivation by dark-annealing was found to be a thermally activated process with an activation energy of 1.2-1.3 eV [2, 50, 51] and does not depend on the doping concentration N_{dop} [52].

The defect activation or rather the degradation process was shown to be a thermally activated process with an activation energy of $E_{\text{deg,slow}} = 0.4\text{ eV}$ [2, 44, 50, 52] for the slow stage and a lower energy barrier of $E_{\text{deg,fast}} = 0.2\text{ eV}$ [41] for the fast stage of degradation. Thereby, the degradation rate constant is increasing with increasing degradation temperature [41].

3.2 Permanent deactivation of BO-related recombination centers

Concerning the dependence of R_{deg} on the illumination intensity I_{ill} it was found [2] that R_{deg} does not depend on I_{ill} for intensities above 0.01 suns as shown in Figure 3.4.

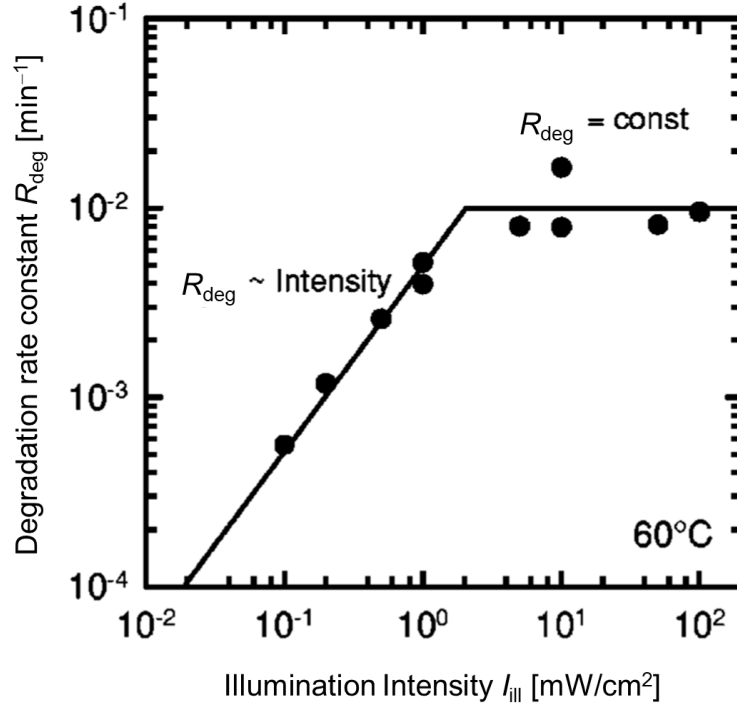


Figure 3.4: Measured degradation rate constants R_{deg} versus the illumination intensity I_{ill} and thus versus different injected carrier concentrations according to Schmidt and Bothe [2].

However, below 0.01 suns, a linear dependence on I_{ill} is found, corresponding to a linear increase of R_{deg} on Δn .

3.2 Permanent deactivation of BO-related recombination centers

As was first shown by Herguth et al. [53] in order to permanently deactivate the BO-related recombination center, the sample must be illuminated at elevated temperature. This lifetime regeneration process results in a stable permanent lifetime τ_{op} after several minutes of illumination on a hot-plate, as demonstrated on our own samples in Figure 3.5(a).

We start our regeneration experiment shown in Figure 3.5 after dark-annealing. We apply regeneration conditions of 185°C and 1 sun of illumination intensity. The permanent deactivation process proceeds over a fast initial lifetime degradation, which is followed by a regeneration of the lifetime. By fitting the evolution of the effective defect concentration N_t^* (see Equation (3.1)) by an exponential decay function, as illustrated in Equation (3.3), the lifetime evolution can be described by a regeneration rate constant R_{reg} (see the inset in Figure 3.5(b)).

$$N_t^* = N_{t,\text{max}}^* [\exp(-R_{\text{reg}} \times t)] \quad . \quad (3.3)$$

The measured regeneration curve shown in Figure 3.5 results in a regeneration rate constant of $R_{\text{reg}} = 100 \text{ h}^{-1}$.

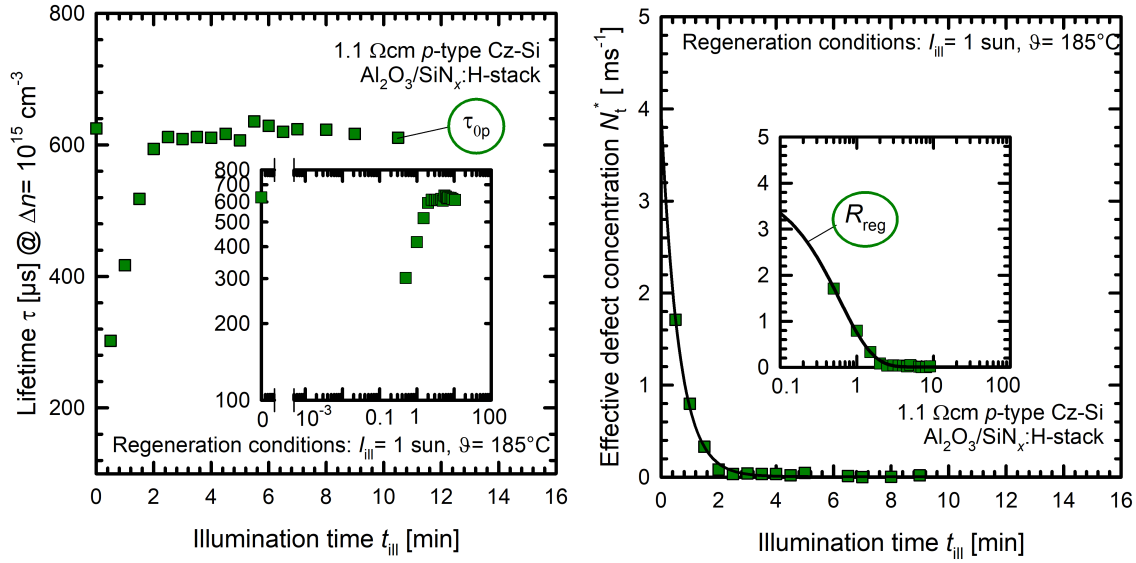


Figure 3.5: (a) Typical lifetime evolution of an 1.1 Ωcm boron-doped *p*-type Cz-Si sample with an Al₂O₃/SiN_x-stack, which is illuminated at elevated temperature ($I_{\text{ill}} = 1 \text{ sun}$, 185°C). This treatment deactivates the boron-oxygen defect and regenerates the lifetime to the so-called permanent lifetime τ_{0p} . The lifetime is measured at 30°C and analyzed at an excess carrier density of $\Delta n = 1 \times 10^{15} \text{ cm}^{-3}$. (b) Calculated effective defect concentration N_t^* versus the illumination time t_{ill} , which can be described by an exponential decay function with a single regeneration rate constant R_{reg} .

In the following, some general influence parameters on the permanent deactivation kinetics of the B-O recombination defect center or rather the lifetime regeneration kinetics, are summarized, which have been established in literature prior to this work and are relevant for this work.

By performing time-resolved lifetime measurements for various Cz-Si samples with different boron concentrations and comparable oxygen concentrations under illumination at elevated temperature, Lim et al. [54] showed for both compensated and non-compensated boron-doped Cz-Si samples a decrease of the regeneration rate constant R_{reg} with the total boron concentration N_A : $R_{\text{reg}} \propto [N_A]^{-1}$ (see Figure 3.6(a)). In general, the regeneration experiments of Lim et al. [54] showed that the regeneration rate constants of the non-compensated Cz-Si samples are higher than that of the compensated Cz-Si samples at all applied regeneration temperatures. The activation energy of the deactivation process was shown to increase linearly with the boron concentration [54].

By varying the interstitial oxygen concentration of the Cz-Si samples for regeneration experiments, Lim et al. [55] found a decreasing regeneration rate constant R_{reg} with increasing oxygen concentration $[O_i]$: $R_{\text{reg}} \propto [O_i]^{-1.5}$ (see Figure 3.6(b)). Wilking et al. [56] observed a weaker dependence of $R_{\text{reg}} \propto [O_i]^{-0.8}$ applying an injection correction. However, in both cases the regeneration process takes longer the higher the interstitial oxygen concentration is.

3.2 Permanent deactivation of BO-related recombination centers

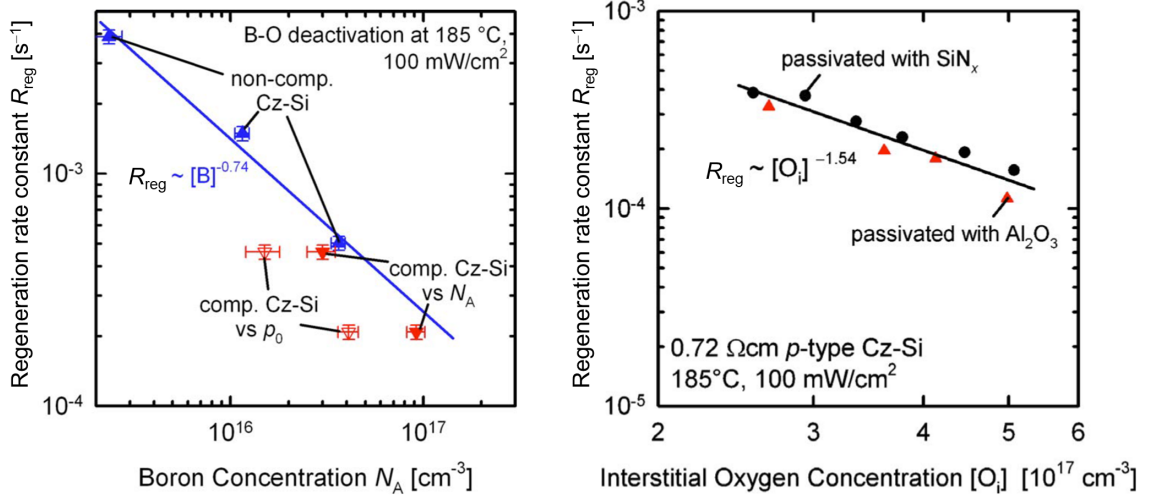


Figure 3.6: Regeneration rate constant R_{reg} versus (a) the boron concentration N_A according to Lim et al. [54] and (b) the interstitial oxygen concentration $[O_i]$ according to Lim et al. [55].

The regeneration process was found to depend critically on the applied illumination intensity, thus the regeneration rate constant R_{reg} is increasing with increasing illumination intensity corresponding to an increasing injected excess carrier concentration Δn [57, 58]. At higher illumination intensities, the regeneration rate constant saturates [57] due to the marginal increase of Δn with further increasing intensity. However, the regeneration process can also be induced if electrons are injected by application of a forward bias voltage to the solar cell at elevated temperatures [4, 53, 59, 60]. The dependence of the regeneration rate R_{reg} on the injected carrier concentration Δn will be discussed in the introduction of Chapter 4 in more detail.

Steckenreiter et al. [61] investigated whether the initial state of the lifetime sample has an influence on the regeneration kinetics. The only impact they found was that after dark-annealing the effective defect concentration N_t^* proceeds mono-exponentially during regeneration, whereas a two-stage process is observed when starting in the fully degraded state [61]. However, after 100 s of deactivation treatment N_t^* is identical for both initial states. Quite similar or even identical regeneration rate constants are observed independent of the initial state [61].

In a study by Walter et al. [62] it was found that the applied firing treatment has a crucial impact on the lifetime level. The lifetimes after dark-annealing τ_0 , after complete degradation under illumination τ_d and after permanent deactivation τ_{0p} show a pronounced dependence on the firing conditions, also described as rapid thermal annealing (RTA) treatment [62]. All three lifetime values increase with increasing belt speed. The regenerated lifetime τ_{0p} is significantly higher for RTA-processed samples than without this treatment [62]. Furthermore, the regeneration rate constant was found to increase with increasing peak temperature [62, 63]. As a part of the RTA treatment, the cooling rate at the end of the applied industrial infrared conveyor-belt furnace influences the regeneration rate constant. Walter et al. [62] found a linear dependence in the potentially relevant temperature range

between 575°C and 625°C by a proportionality coefficient about $2.08 \times 10^{-4} \text{ }^\circ\text{C}^{-1}$ as shown in Figure 3.7.

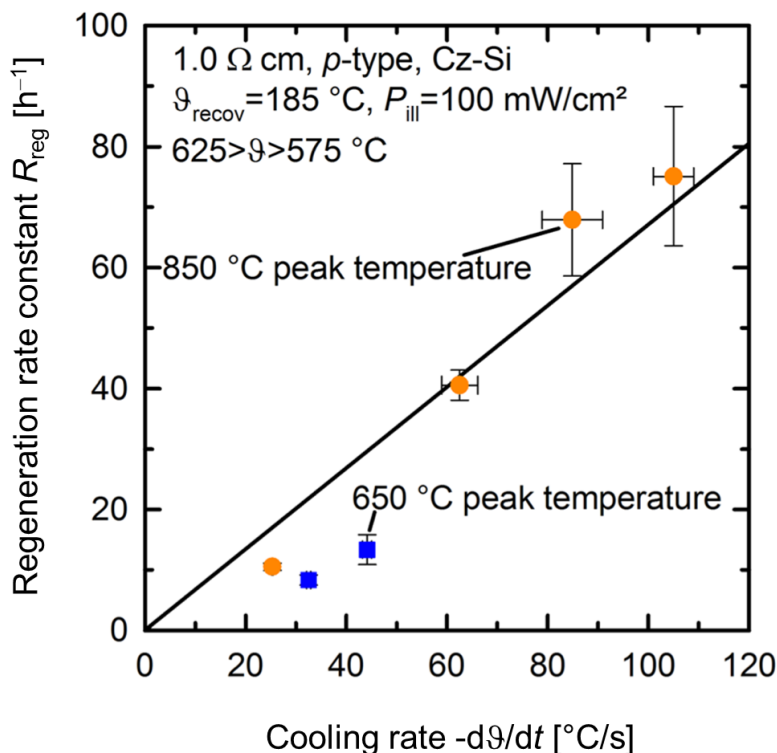


Figure 3.7: Regeneration rate constant R_{reg} in dependence on the cooling rate $-\text{d}\theta/\text{d}t$ according to Walter et al. [62].

Thus, measured temperature profiles has to be considered within regeneration experiments to compare and interpret the regeneration kinetics of identically processed samples with different layers (see Chapter 5) correctly.

All in all, the permanent deactivation process of the BO-defect is a thermally activated process. By varying the regeneration temperature with constant injected carrier concentration, Herguth et al. [60] and Lim et al. [64] determined an activation energy between 0.6 and 0.7 eV. Figure 3.8 shows experimental results from Lim et al. [64] of undiffused and phosphorus-diffused boron-doped Cz-Si samples resulting in comparable activation energies for the regeneration process.

Furthermore, it was found that the activation energy of the deactivation process depends linearly on the doping concentration N_{dop} [54].

Until now, there are contradicting statements in literature about the role of hydrogen on the permanent deactivation mechanism of the boron-oxygen defect. Therefore, we dedicate a subsection to this topic in the following.

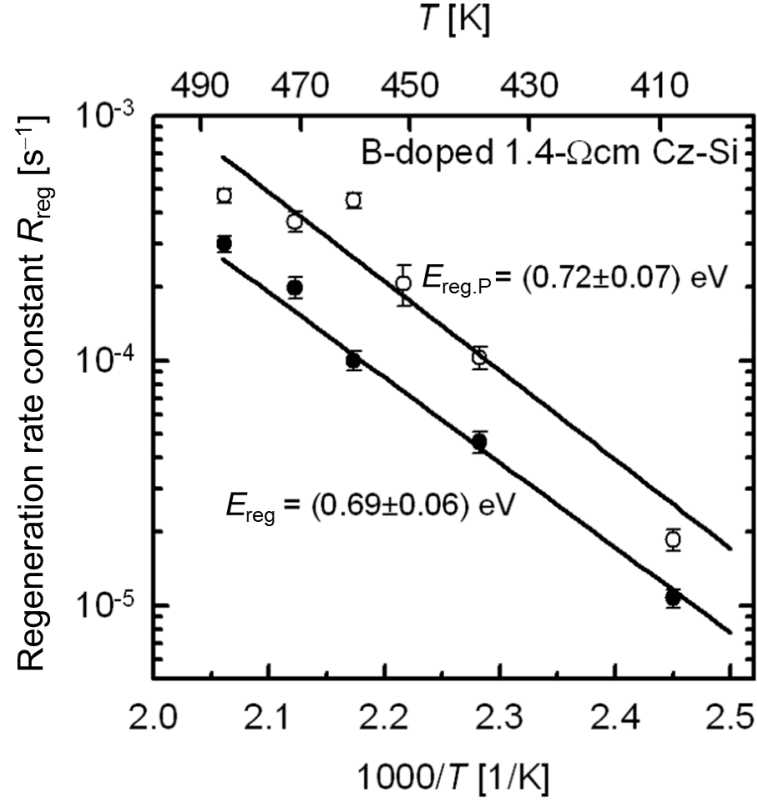


Figure 3.8: Regeneration rate constant R_{reg} versus the inverse regeneration temperature $1000/T$ according to Lim et al. [64].

3.2.1 The role of hydrogen

Münzer et al. [65] were the first who conjectured in 2009 hydrogen to be involved in the permanent deactivation of the boron-oxygen defect due to the observation that only solar cells with a hydrogen-rich plasma-enhanced chemical vapour deposited (PECVD) silicon nitride layer showed a regeneration of their performance. The results of regeneration experiments on boron-doped *p*-type Cz-Si wafers passivated with and without hydrogen-rich silicon nitride layers were interpreted similarly by Nampalli et al. [66]. They observed no complete lifetime regeneration within two hours of illumination with a light intensity of 65 mW/cm^2 at 172°C for samples with no hydrogen source present during *firing*. However, this regeneration duration was probably just not long enough, as Lim et al. [55] were able to completely regenerate *unfired* lifetime samples with hydrogen-lean Al_2O_3 layers (10 h at 185°C , 100 mW/cm^2). Walter et al. [67] confirmed these results on *fired* lifetime samples with the same structure (i.e. hydrogen-lean Al_2O_3). From these results it was concluded that hydrogen has no direct impact on the deactivation process. On the other hand, in [68, 69] it was reported that the boron-oxygen (BO) deactivation rate constant, which is often described as regeneration rate constant R_{reg} , increases with increasing hydrogen concentration in the silicon bulk, though without direct measurements of the actual hydrogen content in the silicon bulk.

In 2019, a method was introduced by Walter et al. [70] to directly measure the hydrogen concentration in the silicon bulk via simple resistivity change measure-

ments in contrast to rather difficult measurement methods like secondary ion mass spectrometry (SIMS) [71] or low-temperature Fourier-Transform Infrared (FTIR) spectroscopy [17]. Hence, in this thesis we quantitatively study the impact of hydrogen on the BO degradation and deactivation kinetics aiming at resolving the contradicting statements in the literature (see Chapter 5).

3.3 BO defect models

In this section, a short summary of previous and advanced current physical models for the observed BO-related lifetime degradation and regeneration kinetics from an atomic perspective is presented.

3.3.1 Physical models

There are three relevant models for the atomic structure of the BO defect: The first model proposes that the BO defect consists of one substitutional boron atom and two interstitial oxygen atoms (B_sO_{2i}), whereas the second model assumes rather an interstitial boron atom and an oxygen dimer (B_iO_{2i}). The third model suggests a defect consisting of both substitutional and interstitial boron atoms with only one interstitial oxygen atom ($B_iB_sO_i$).

3.3.1.1 B_sO_{2i} model

In 2002, Schmidt et al. [52] proposed a reaction between a substitutional boron atom (B_s) and a fast-diffusing oxygen dimer (O_{2i}) based on the observed linear dependence of the effective defect concentration N_t^* on the boron concentration ($[B_s] = N_{dop}$) [2, 39, 52] and the quadratic increase of N_t^* with the interstitial oxygen concentration $[O_i]$ [2]. The oxygen dimers O_{2i} are the mobile species within this model and diffuse in silicon until they are captured by immobile substitutional boron B_s to form a B_sO_{2i} complex. The O_{2i} dimers are assumed to diffuse faster in the model if electrons are injected into the silicon due to a recombination-enhanced mechanism. The B_sO_{2i} complex acts as a highly effective recombination center. The defect formation process is limited by the diffusion of the oxygen dimer, which is thermally activated process. It diffuses significantly faster than interstitial atomic oxygen in silicon [72, 73] because it does not build Si-O bonds and is just weakly coupled to the silicon lattice. A calculated migration energy in the range 0.3–1 eV by Lee et al. [74] for oxygen dimers in silicon corresponds to the experimentally determined activation energy of the degradation process of 0.4 eV [2, 44, 50, 52]. In contrast, a much higher migration energy of 2.5 eV for interstitial oxygen atoms in silicon was calculated by Lee et al. [74].

Adey et al. [51] calculated an activation energy of 0.3 eV using density functional calculations. In the proposed *Bourgoin mechanism* [75], the oxygen dimer is double-positively charged in *p*-type silicon and exists in two configurations, the squared (O_{2i}^{sq}) and the staggered (O_{2i}^{st}) configurations. For diffusion in silicon it is necessary that the squared form converts to the staggered form. The energy for this transition is about 0.86 eV in the double-positively charged state, as shown by the blue line in

Figure 3.9. Hence, oxygen dimers are immobile at room temperature without any carrier injection (e.g. illumination).

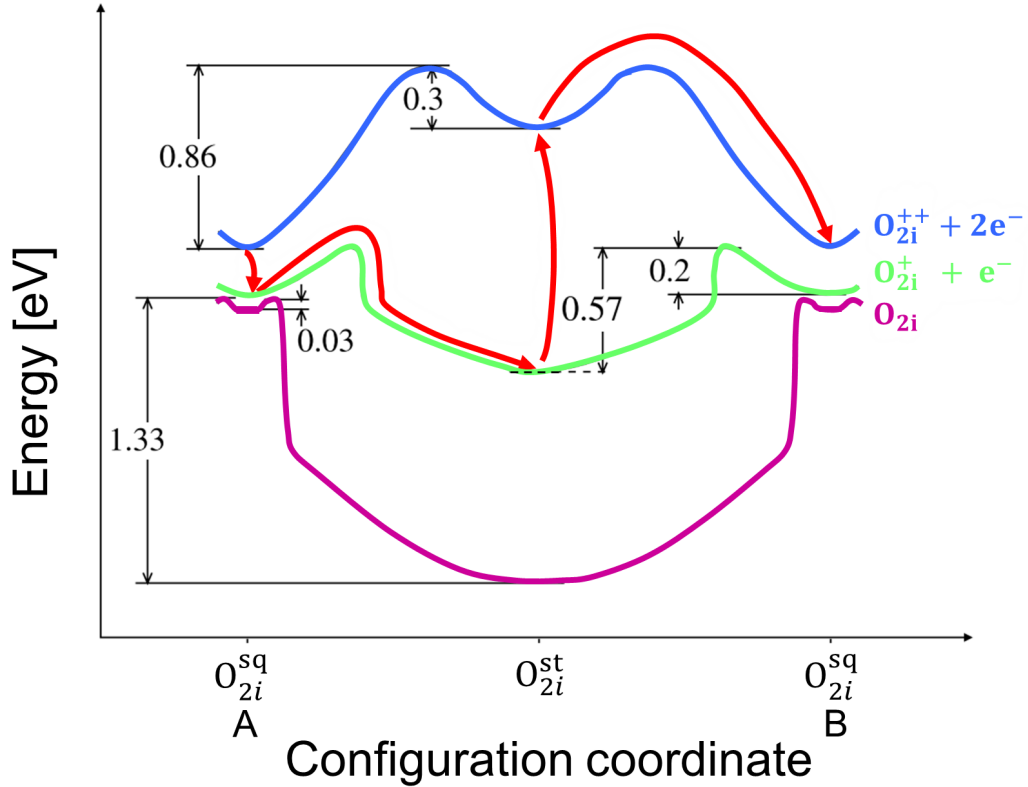
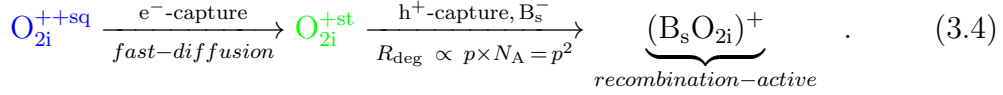


Figure 3.9: Energy profile for the oxygen dimer diffusion in different configurations according to Adey et al. [51]. The red arrows describe the diffusion via a *Bourgoin mechanism*.

If O_{2i}^{++sq} (position A, blue line) can capture an electron, it becomes O_{2i}^{+sq} (green line) with a reduced energy to 0.2 eV for conversion to O_{2i}^{+st} . After emitting an electron, respectively capturing a positive hole, the configuration O_{2i}^{+st} performs a diffusion jump with an energy barrier of 0.3 eV to O_{2i}^{++sq} (position B). In general, the oxygen dimers move randomly from one site in the silicon lattice to an adjacent equivalent site in the silicon lattice by successive atomic rearrangements and charge-state changes. This process repeats until the oxygen dimer is captured by negatively charged substitutional boron atom B_s^- forming $B_sO_{2i}^+$ due to Coulomb attraction.

Besides the Coulomb attraction, the kinetics of the defect formation depends on the lattice-jump rate of the dimers, which in itself is controlled by the hole concentration p . In addition, it depends on the probability that a diffusing dimer becomes trapped by a boron atom [44]. The oxygen dimer has to be in a specific radius of the substitutional boron atom B_s to be captured. The concentration of boron atoms available for defect generation corresponds to the total boron concentration N_A (i.e. the doping concentration) in the case of uncompensated silicon. Equation (3.4) shows schematically the defect generation mechanism in the B_sO_{2i} defect model proposed by Palmer et al. [44] and Adey et al. [51] based on a detailed theoretical model for the kinetics of the diffusion reaction and density functional calculations in the context of experimental data.



The proportionality of the hole capture and the number of possible substitutional boron atoms for defect formation to the boron concentration is consistent with the observed quadratic dependence of the degradation rate R_{deg} on the doping concentration [44, 50]. As suggested by the experimental results [2, 76], the defect formation is a recombination-enhanced process showing a proportionality of the degradation rate on the injected excess carrier concentration at very low illumination intensities ($< 1 \text{ mW/cm}^2$) [2] or applied forward-bias voltages in the dark in the case of solar cells [76]. This fits well into the model of Schmidt et al. [2], which assumes a recombination-enhanced oxygen dimer diffusion mechanism. The degradation process ceases when all the existing oxygen dimers have been captured by substitutional boron atoms.

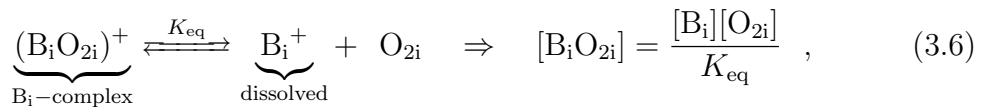
The model discussed so far was developed based on the experimental results of degradation experiments on oxygen-rich and non-compensated boron-doped p -type Czochralski-silicon samples. However, this model cannot explain the experimental results of degradation experiments on p -type Cz-Si samples compensated with phosphorus [45, 46], which show a linear dependence of the defect concentration N_t^* on the net doping concentration p_0 and not on the total boron concentration N_A . The net doping concentration p_0 is given by $p_0 = N_A - N_D$ with N_A being the acceptor concentration (usually boron) and N_D being the donor concentration (usually phosphorus). Due to the contradictions with the model discussed above, a new defect model had to be proposed.

3.3.1.2 B_iO_{2i} model

In 2010, Voronkov and Falster [77] proposed a defect model with one interstitial boron atom B_i and an interstitial oxygen dimer O_{2i} , forming a recombination-active complex B_iO_{2i} . In this model, it is assumed that the interstitial boron atoms B_i (single-positive in p -type silicon [78]) are generated during ingot cooling by growing oxygen precipitates via a kick-out mechanism and congregate to boron nano-precipitates (B_i -NPs) upon lowering the temperature. By capturing a hole h^+ , B_i^+ atoms are released from the neutral B_i -NPs in an established equilibrium:



The highly mobile B_i^+ atoms migrate in the lattice and are mostly trapped in B_i -clusters such as B_iO_{2i} , B_iO_i or B_iB_s . These B_i -complexes are in equilibrium with their reactants as exemplarily shown in the Equation



with K_{eq} being the equilibrium constant, or more precisely in this case the dissociation constant of the B_iO_{2i} complex. The concentration $[\text{B}_i\text{O}_{2i}]$ is proportional to

3.3 BO defect models

the product of the concentrations of the still dissolved isolated boron atoms $[B_i^+]$ in equilibrium and of the frozen-in oxygen dimers $[O_{2i}]$. The latter is proportional to the quadratic monomeric oxygen concentration $[O_i]^2$ and, as shown in Equation (3.5), $[B_i^+]$ is proportional to the hole concentration $[h^+]$, which equals the net doping concentration p_0 in a temperature range below $\sim 350^\circ\text{C}$ (i.e., the intrinsic point) [77]. Thus, the concentration $[B_iO_{2i}]$ is proportional to $p_0 \times [O_i]^2$, which also describes the experimental dependence of the effective defect concentration. In addition at a temperature well below 350°C (e.g. at room temperature) it is assumed that the B_i -clusters are frozen-in with no equilibrium reaction with the dissolved species anymore [77]. The frozen-in B_iO_{2i} is considered as a latent center (LC) of the boron-oxygen defect with a low recombination activity, which is reconstructed into a slow-forming recombination-active center (SRC) of the boron-oxygen defect. Figure 3.10 shows possible free energy diagrams for the reconstruction $LC \rightleftharpoons SRC$ according to Reference [77].

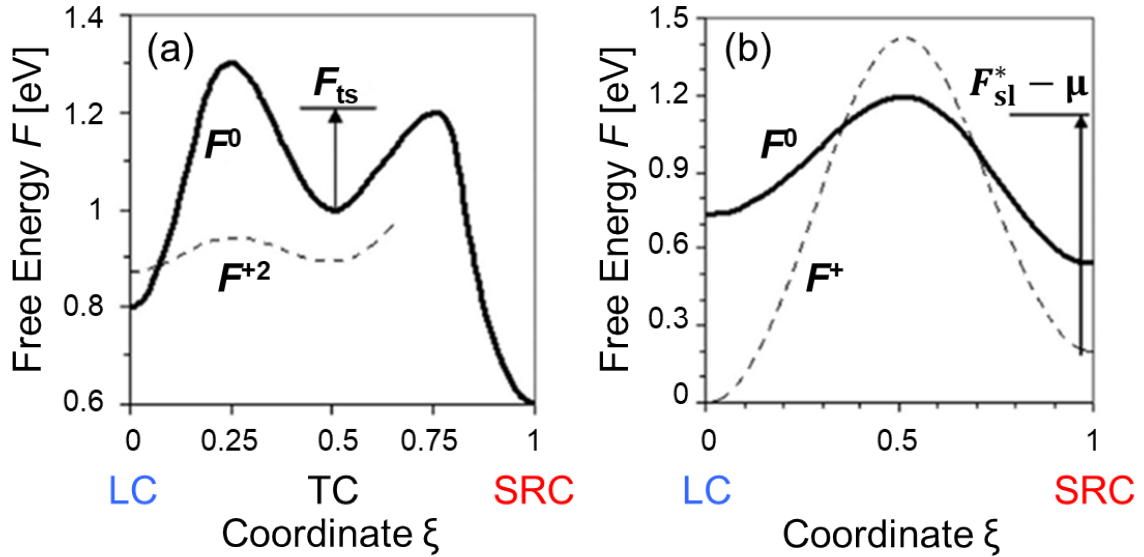


Figure 3.10: Free energy diagrams of the latent centre (LC) and the slowly formed recombination-active center (SRC) of the B_iO_{2i} defect in different charge states within the B_iO_{2i} defect model proposed by Voronkov and Falster [77]. The black arrows describe the model of transition (a) from a double-positive charge state through a transient configuration (TC) by overcoming the free energy barrier F_{ts} (defect activation) and (b) from an initial single-positive charge state to a neutral state by overcoming the transition barrier $F_{sl}^* - \mu$ (defect deactivation).

According to the quadratic dependence of the degradation rate constant R_{deg} on the substitutional boron concentration $R_{deg} \propto [B_s]^2$ [2, 44, 50], the reconstruction from LC to SRC has to involve the capture of two holes. Figure 3.10(a) describes the case of defect activation over a double-positive charged state (dashed line) with a transient center (TC) as an intermediate configuration at different structural coordinates ξ [77]. For transition from LC^0 to TC^0 , a large free energy barrier in the neutral state has to be overcome, but a low free energy barrier ($F^{+2}(TC) - F^{+2}(LC)$) in the double-positive state for the transition from LC^{+2} to TC^{+2} followed by a free energy barrier about F_{ts} (black arrow in Figure 3.10(a)) for the transition from TC^0 to SRC^0 after capturing two electrons. The neutral state LC^0 captures two holes h^+ ,

recharges to a double positive state LC^{+2} and converts to the intermediate configuration TC^{+2} , which captures afterwards two electrons becoming TC^0 and transforms to SRC^0 , i.e. the recombination-active form of the B_iO_{2i} defect [77].

For defect deactivation in darkness, an inverse dependence of the deactivation rate R_{de} on the hole concentration ($R_{de} \propto 1/p_0$) was found by dark-annealing at different temperatures of two Cz-Si samples with different doping concentrations (see Figure 13 in Ref. [41]). Therefore, Voronkov and Falster [77] propose a transition path under the emission of a hole from the SRC state to the LC state within their defect model. Figure 3.10(b) shows the free energy diagram for this process. By carrier injection (i.e. illumination) almost a complete transformation from LC^0 to SRC^0 takes place. In darkness, the single-positive charge state SRC^+ is the dominant form, which is moving along the structural coordinates of the free energy profile F^+ through thermal activation. An energy barrier of $F_{si}^* - \mu$ (black arrow in 3.10(b)) has to be overcome. The SRC^+ is supposed to recharge to the neutral state SRC^0 by emitting a hole at the coordinate $\xi \approx 0.7$ (intersection of the two energy curves F^0 and F^+), which considerably reduces the energy barrier to the LC^0 state. After the transformation to the LC^0 state by thermal activation, the defect center in the LC^0 form recharges back (intersection of the two energy curves F^0 and F^+ , $\xi \approx 0.3$) to the single-positive charged latent center LC^+ and moves to its free energy minimum ($\xi = 0$).

Figure 3.11 shows schematically the defect activation and deactivation mechanisms within the B_iO_{2i} defect model. The described B_iO_{2i} model provides a consistent explanation for the experimental results of degradation experiments on *p*-type silicon samples compensated with phosphorus [45, 46].

However, this model cannot explain the later observed results obtained on boron-doped Czochralski-silicon samples co-doped with gallium [47], which showed a proportional dependence of the defect concentration N_t^* on the boron concentration $[B_s]$ rather than on the net doping concentration $p_0 = [B_s] + [Ga_s]$. In addition, one year later, doubts arose on the participation of oxygen dimers in formation of the lifetime-degrading centres based on experiments of a prolonged annealing step [79], which is known to significantly reduce the oxygen dimer concentration. However, the anneal did not significantly reduce the lifetime degradation. This led to the suggestion of a $B_iB_sO_i$ model.

3.3.1.3 $B_iB_sO_i$ model

In 2013, Voronkov and Falster [80] developed a modification of their previously presented B_iO_{2i} defect model (see 3.3.1.2) with the main change on the latent center (LC) suggested to be a $B_iB_sO_i$ defect. The central assumptions of the previous model, however, remained: The latent center is already present after silicon crystal growth before illumination and is not formed by carrier injection. However, the latent center is now assumed to be of the form $B_iB_sO_i$ excluding participation of oxygen dimers [79] and including the participation of substitutional and interstitial boron atoms [47]. In order to discriminate this latent center from the previously described defect model, it will be denoted as LCS in the following instead of LC.

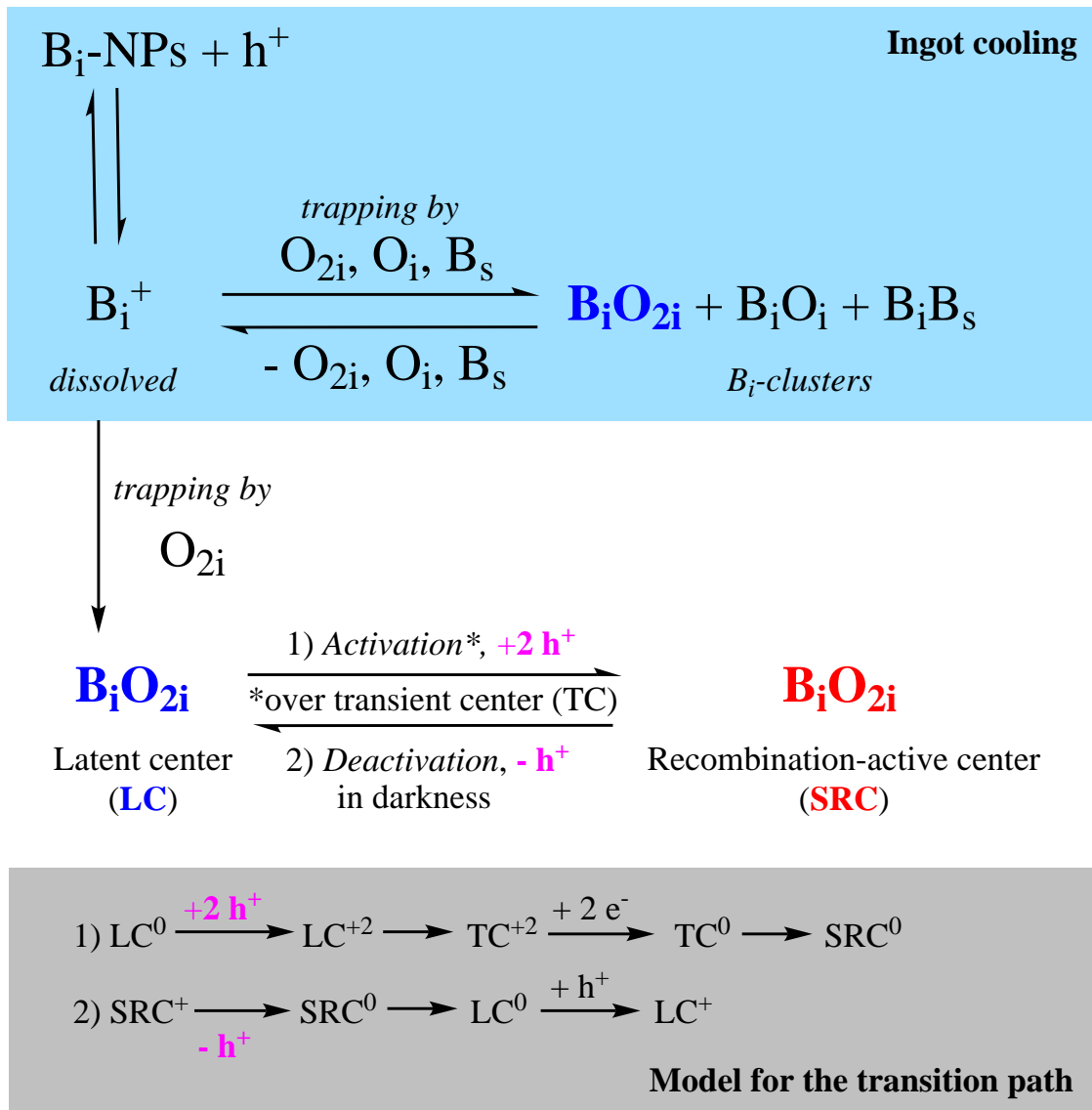
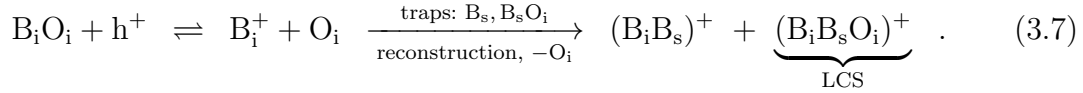


Figure 3.11: Schematic of the defect activation and deactivation mechanism in the B_iO_{2i} defect model proposed by Voronkov and Falster [77]. The latent complex $B_iO_{2i}^+$ recharges into the neutral state LC^0 in the presence of excess electrons, which is the starting state in the transition path of activation. The transition path of deactivation in darkness starts with the defect complex in the single-positive charge state.

The $B_iB_sO_i$ concentration is assumed to be proportional to $[B_s][O_i]^2$. The LCS defects are formed from two different frozen-in defects B_sO_i and B_iO_i [80]. The first one is frozen-in at relatively high temperatures around 600°C with a concentration proportional to $[B_s][O_i]$, whereas the second one is frozen-in at relatively low temperature below 350°C with a concentration proportional to $p_0[O_i]$. The interstitial boron atoms B_i are supposed to redistribute at still lower temperature from the initially dominant traps O_i to the traps B_s and B_sO_i , which have a larger binding energy:



The B_iB_s defect is the dominant state after this redistribution with a concentration proportional to $p_0[O_i]$ ($[B_iB_s] \equiv [B_iO_i]_{\text{initial}}$). With this proportionality in mind, the concentration of $B_iB_sO_i$ is given as follows:

$$\frac{[B_iB_sO_i]}{[B_iB_s]} \propto \frac{[B_sO_i]}{[B_s]} \propto [O_i] \Rightarrow [B_iB_sO_i] \propto [B_iB_s] \times [O_i] \Rightarrow [B_iB_sO_i] \propto p_0[O_i]^2 . \quad (3.8)$$

The proportionality of $B_iB_sO_i$ in Equation (3.8) on the squared interstitial oxygen concentration $[O_i]^2$ and hole concentration p_0 agrees with the observed dependencies of the effective defect concentration in boron-only and compensated p -type material. The reconstruction from the LCS to SRC is supposed to be the same as in the B_iO_{2i} model (see Figures 3.10 and 3.11) [77].

In Cz-Si material co-doped with B and Ga, the interstitial boron atoms B_i can be trapped by B_s or Ga_s with the same probability. Therefore, the concentration of the B_iB_s defect is reduced in comparison to boron-only doped samples by $[B_iB_s]/([B_iB_s] + [B_iGa_s])$, which equals the fraction $[B_s]/([B_s] + [Ga_s])$. Because the $B_iB_sO_i$ defects are in equilibrium with the B_iB_s defects, their concentration is reduced by the same fraction:

$$[B_iB_sO_i] \propto p_0[O_i]^2 \times \frac{[B_s]}{([B_s] + [Ga_s])} \xrightarrow{p_0=[B_s]+[Ga_s]} [B_iB_sO_i] \propto [O_i]^2[B_s] . \quad (3.9)$$

Since $p_0 = [B_s] + [Ga_s]$ is valid for B and Ga co-doped samples, the LCS concentration $[B_iB_sO_i]$ becomes proportional to $[B_s]$, which is in agreement with the reported results from Forster et al. [47].

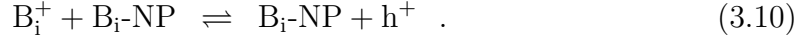
In general, the mobile interstitial boron atom B_i in this model could be any fast-diffusing interstitial impurity X_i , which is single-positively charged (such as interstitial metal impurities), since the concentration of any impurity of this kind would be proportional to p_0 . Hence, other involved impurities, such as Cu_i , involved in the LID mechanism could be possible.

3.3.1.4 Permanent deactivation model

In the permanent deactivation model proposed by Voronkov and Falster [80], the defects B_iB_s and $B_iB_sO_i$ are assumed to dissociate under illumination at elevated temperature, releasing highly mobile B_i^+ atoms. Subsequently, the fast-diffusing

3.3 BO defect models

B_i^+ atoms are captured by B_i -NPs as an irreversible loss mechanism (see Equation (3.10)).



The concentration of B_i -containing defects is permanently reduced and thus the lifetime permanently regenerated. In the model of Voronkov and Falster [9] describing the permanent deactivation of the BO centre (i.e. the regeneration of lifetime), the regeneration rate constant R_{reg} is assumed to linearly depend on the injected excess carrier concentration Δn , which is assumed to be constant during illuminated annealing. In addition, the lifetime is assumed to be constant during regeneration [9]. By investigating the regeneration rate constant R_{reg} as a function of Δn we can either find further support for the above statement (if the linear dependence can be confirmed) or refute it in this work. Our experimental investigations will be presented in Chapter 4.

The regeneration rate constant R_{reg} can be expressed with a simple Arrhenius-type factor $R(T)$ as:

$$R_{\text{reg}} = n R(T) . \quad (3.11)$$

Thus, the complicated dependence of R_{reg} on temperature T and material parameters comes just from the effect of these parameters on the electron concentration n [9] or rather the injected excess carrier concentration during regeneration in the case of low-hydrogen p -Si material.

In the presence of hydrogen, the electron concentration n is additionally strongly increased due to partial passivation of the major recombination centers (BO defects) by hydrogen and thus the regeneration rate constant is increased according to [9]:

$$R_{\text{reg}} = n R(T) + [H^-] R_H(T) , \quad (3.12)$$

with the concentration of negatively charged hydrogen $[H^-]$ and R_H being a simple Arrhenius-type factor for hydrogen-related complexes. It is assumed that in boron-doped samples, hydrogen is partly trapped by boron after firing upon cooling into neutral hydrogen-boron pairs HB, whereas the major part of the hydrogen is present in the form of dimers [9, 81]. The HB pairs are assumed to be the main source of hydrogen during permanent deactivation, releasing some free H^+ ions, which are recharged into H^- in the presence of excess electrons. The negatively charged H^- ions passivate SRC^+ and form H^-SRC^+ complexes, leading to a SRC loss. The dependence of the regeneration rate constant on the hydrogen concentration in the silicon bulk is investigated systematically in this thesis to verify or falsify the hypothesis of the involvement of hydrogen in the regeneration mechanism. Our experimental investigations will be presented in Chapter 5.

4 In-situ characterization of electron-assisted regeneration of Cz-Si solar cells

We examine the regeneration kinetics of passivated emitter and rear solar cells (PERCs) fabricated on boron-doped p -type Czochralski-grown silicon wafers in darkness by electron injection via application of a forward bias voltage at elevated temperature (140 °C). Based on these dark regeneration experiments, we address the existing inconsistency regarding the measured linear dependence of the regeneration rate constant on the excess carrier density. Using the method of dark regeneration by current injection into the solar cell, we are able to measure the total recombination current of the solar cell at the actual regeneration temperature under applied voltage, i.e., at the physically relevant regeneration conditions. This current is proportional to the overall recombination rate in the cell and, hence, reflects the changing bulk recombination during the regeneration process. From the measured time-dependent cell current, we determine the regeneration rate constant R_{reg} of the boron-oxygen defect. Measuring the EL signal emitted by the solar cell during regeneration, we are able to directly determine Δn during regeneration for each applied voltage. Our experimental results unambiguously show that R_{reg} increases proportionally with Δn during the regeneration process.

4.1 Introduction

The boron-oxygen(BO)-related defect center limits the efficiency of silicon solar cells fabricated on boron-doped Czochralski-grown silicon (Cz-Si) after light-induced degradation (LID). As previously shown, however, the BO defect can be permanently deactivated, i.e. the efficiency can be fully regenerated, if the solar cell is exposed to illumination or, alternatively, if electrons are injected by application of a forward bias voltage at elevated temperatures [4, 53, 59, 60]. For the regeneration under illumination, a dependence of the regeneration rate constant R_{reg} on the average excess carrier density Δn_{avg} in the bulk of the silicon base, determined from room-temperature measurements, has been reported by several research groups [57, 58]. The excess carrier density actually injected during regeneration is not reflected.

The only statement that can be made is: R_{reg} increases proportionally with the illumination intensity [57, 58] (see Figure 4.1) and different applied illumination intensities correspond to different injected excess carrier concentrations. However, the excess carrier concentration and the lifetime at a fixed excess carrier density (Figure 4.2(a)) changes strongly over time during regeneration at room temperature

until regeneration is completed. This becomes clearer in the injection-dependent lifetime evolution shown in Fig. 4.2(b).

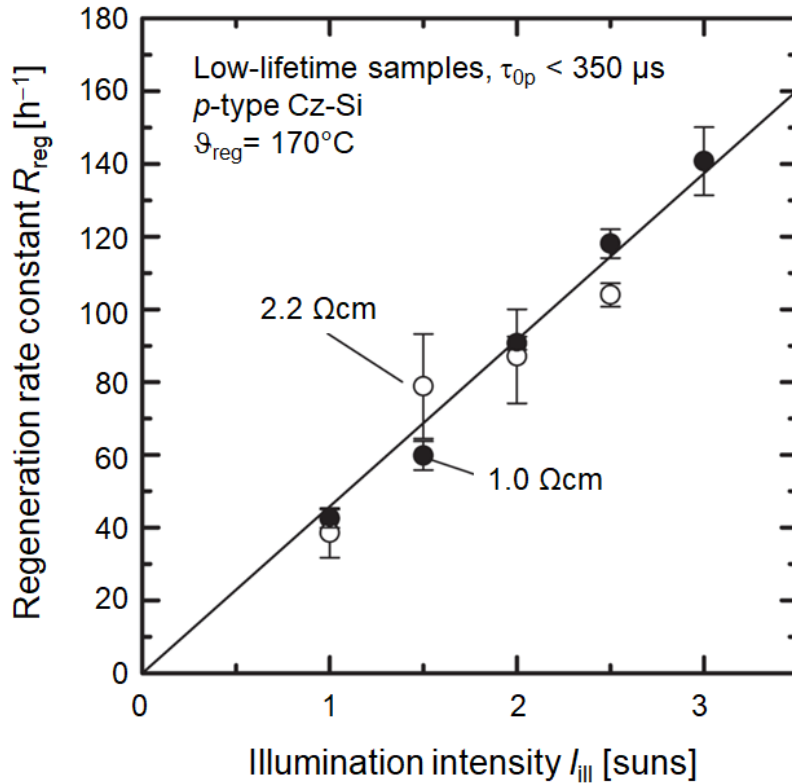


Figure 4.1: Regeneration rate constant R_{reg} measured as a function of illumination intensity I_{ill} for boron-doped Cz-Si wafers with a linear fit of the data points (black line), taken from [57].

The excess carrier concentration increases strongly during the regeneration process due to a loss of the BO recombination centers. A constant regeneration rate constant, determined by a mono-exponential rise-to-maximum function at a selected injection density of $\Delta n = 1 \times 10^{15} \text{cm}^{-3}$ (see Fig. 4.2(a)), seems to be inconsistent under the assumption that the regeneration rate constant is proportional to the excess carrier density and consequently to the effective lifetime. One possible explanation would be that the lifetime is in fact constant at the increased temperature applied during regeneration [9], which would result in a constant Δn value at the regeneration temperature.

In the following, we investigate the kinetics of regeneration for the first time at a well-defined constant excess carrier density directly at the regeneration conditions. In order to examine the regeneration at a well-defined Δn and to isolate the impact of the electron injection on the regeneration kinetics, we measure the current flow through PERC solar cells at varying applied forward bias voltages in the dark at elevated temperatures. Thus, our experiments allow for the first time to find out the reason for the discrepancy discussed above.

4.2 Experimental details

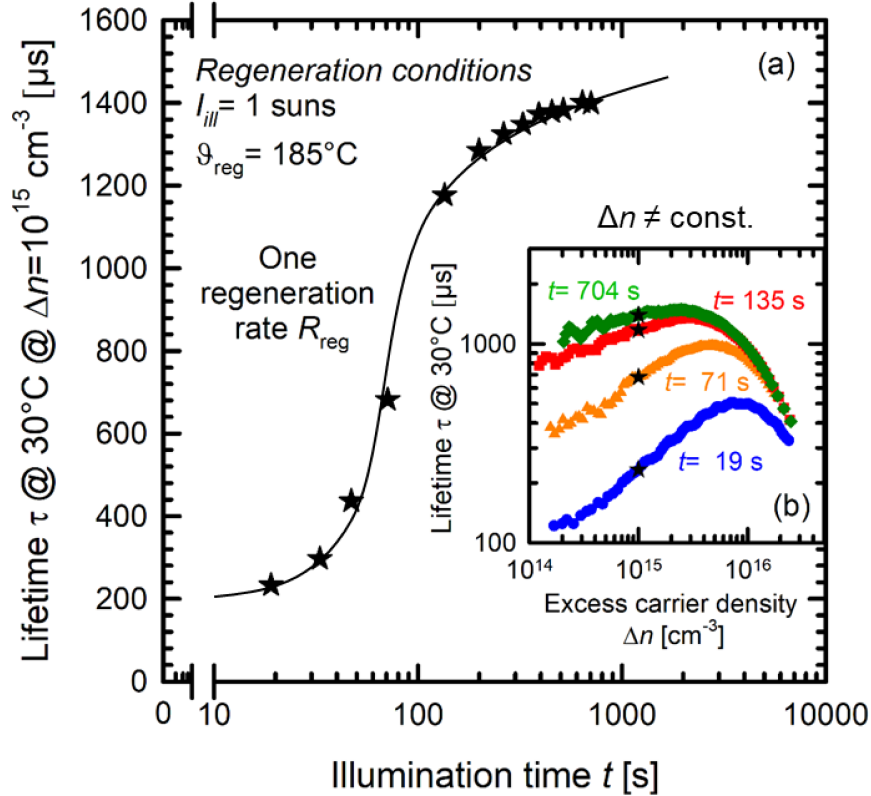


Figure 4.2: Typical lifetime evolution of an 1.6 Ωcm boron-doped p -type Cz-Si sample with an $\text{Al}_2\text{O}_3/\text{SiN}_x$ -stack, which is regenerated by an illumination intensity of 1 sun at 185°C and measured at 30°C . (a) The lifetime evolution at a fixed excess carrier density of $\Delta n = 1 \times 10^{15} \text{ cm}^{-3}$ can be described by an exponential rise to maximum function with one regeneration rate constant R_{de} . The effective lifetimes are extracted from (b) the injection-dependent lifetime during the regeneration process (marked by star symbols). Differently colored curves correspond to different times of illumination at elevated temperature before the lifetime measurement at room temperature.

4.2 Experimental details

All examined solar cells in this chapter are passivated emitter and rear cells (PERCs) fabricated on 2.0-2.5 Ωcm boron-doped p -type Cz-Si wafers, with boron concentrations in the range $(5.7 - 7.2) \times 10^{15} \text{ cm}^{-3}$ and oxygen concentrations in the range $(6 - 7) \times 10^{17} \text{ cm}^{-3}$, using an industrial-type screen-printing process [82]. The $156 \times 156 \text{ mm}^2$ sized solar cells have an efficiency in the range of $(20.52 \pm 0.22) \%$ before they were laser-cut into $25 \times 25 \text{ mm}^2$ cells to increase the number of nominally identical cells and to reduce the total current flow through the cell during current injection in darkness. First, we characterize all cells by measuring their I - V characteristics (LOANA tool, pv-tools GmbH, Hamelin, Germany) in the fully degraded and the dark-annealed states, respectively. The solar cells are degraded at room temperature using a halogen lamp with an illumination intensity of $I_{\text{ill}} = 10 \text{ mW/cm}^2$ for 65 h (fully degraded state). Dark annealing is performed under ambient environment on a hot plate at 200°C for 10 min (annealed state). The measured efficiencies in the fully degraded state are $(19.06 - 19.35) \%$, whereas the efficiencies after dark annealing, which temporarily deactivates the BO defect, are in the range $(19.43 - 19.85) \%$.

Directly after dark annealing, we place the particular solar cell between two brass plates connected with Teflon screws, as shown in Fig. 4.3. This setup has been especially developed in the framework of this thesis.

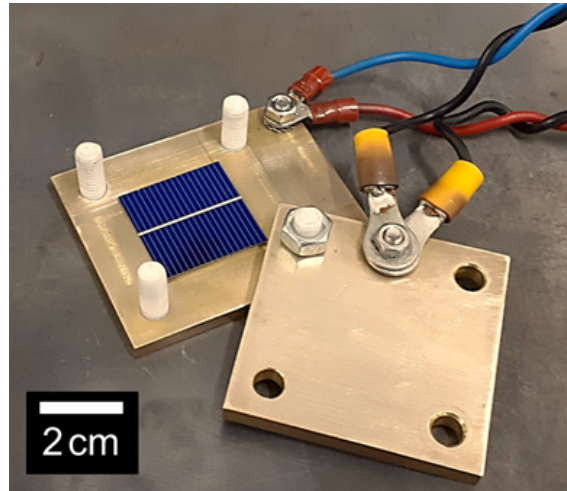


Figure 4.3: Photo of the clamped solar cell placed on the hot plate.

This sandwich-like structure is then put onto a conventional hot plate (Präzitherm TR 28-3 T, *Harry Gestigkeit*). After 30 mins, the thermal equilibrium is reached and a voltage V_{appl} is applied, which is kept constant during the entire experiment in darkness. The cell current I_{cell} (red symbols in Fig. 4.7), which is proportional to the overall recombination rate in the cell, is measured by a voltage-drop over a resistance, which is connected in series (see Fig. 4.4).

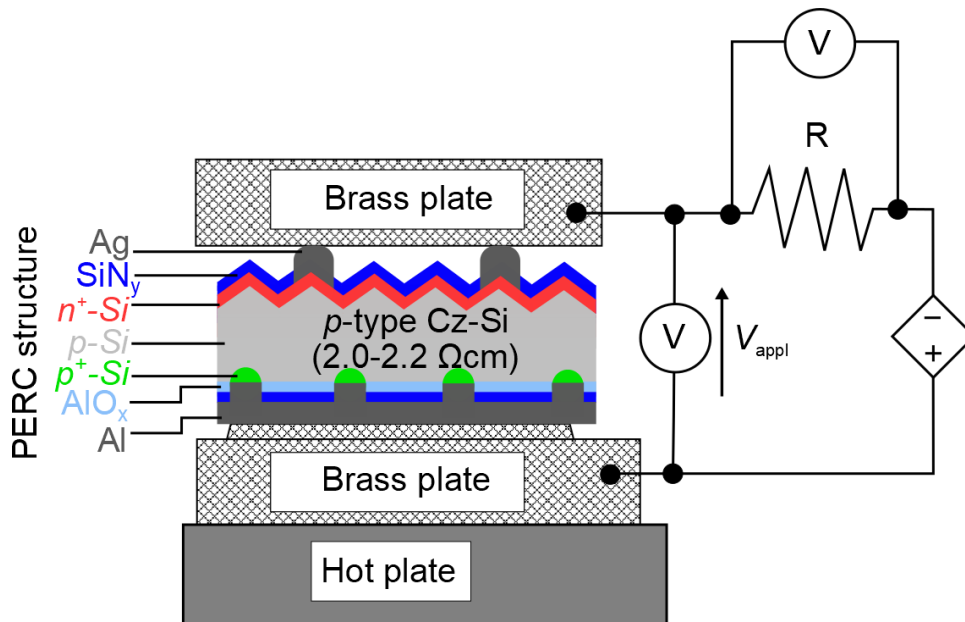


Figure 4.4: Schematic of our set-up A for the in-situ regeneration experiments in darkness.

We choose the resistance (0.1Ω or 1Ω) according to the examined current range. The initial state of the solar cells was after dark annealing and the temperature of the

4.2 Experimental details

cell on the hot plate was kept constant at 140°C during regeneration. After complete regeneration, we characterize each solar cell again by illuminated I - V measurements (25°C , AM1.5G spectrum, 1 sun) using the LOANA solar cell characterization tool (pvtools, Hamelin, Germany).

To determine the applied effective local junction voltage V_i and the injected excess carrier concentration Δn during regeneration at 140°C , we combine the regeneration by carrier injection into a solar cell by applying a forward-bias voltage V_{appl} with an *in-situ* electroluminescence (EL) characterization at regeneration conditions. For this purpose, we modified the mounting bracket by a window in the top brass plate (see Fig. 4.5).

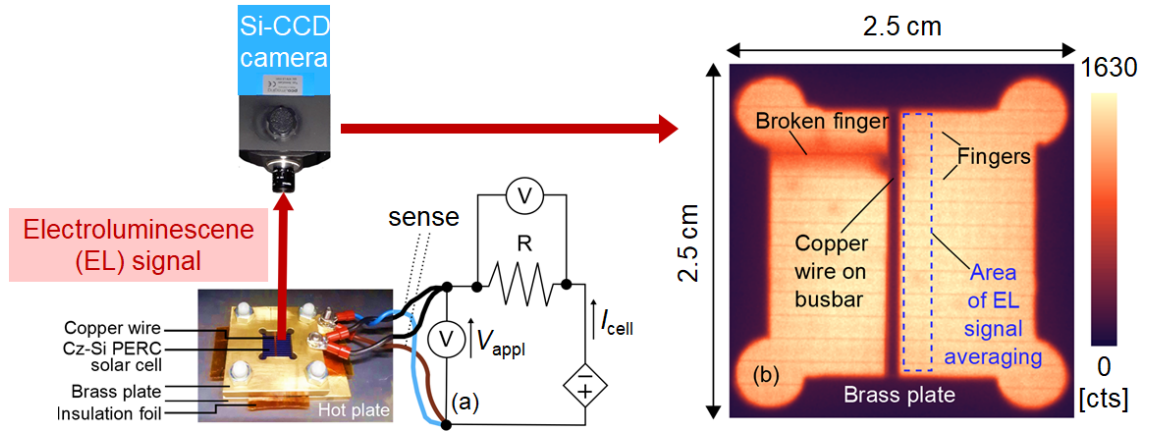


Figure 4.5: Set-up B for the in-situ measurements of the cell current I_{cell} and the EL intensity Φ_{EL} during regeneration. (a) The front side of the solar cell is contacted by a copper wire centrally inserted into the window of the top brass plate. The rear side is fully contacted by a brass plate. We apply a forward-bias voltage V_{appl} between the two brass plates and detect the resulting EL signal during regeneration using a silicon charge-coupled device (Si-CCD) camera. The cell current is measured via a voltage-drop over a resistance of $0.1\ \Omega$. (b) The EL intensity is analyzed next to the busbar, where the solar cell is contacted by a copper wire.

For contacting the front side of the solar cell, more precisely the centrally arranged busbar, a copper wire is centrally inserted into the window of the top brass plate. The rear side is fully contacted by a brass plate. To prevent a short circuit over the top and bottom brass plate, insulation foil is used. Furthermore, small scroll springs are inserted to compensate thermal expansions and to guarantee contacting of the solar cell during the regeneration process. The regeneration process is examined by performing parallel EL and I - V measurements on comparable $25 \times 25\ \text{mm}^2$ solar cells with measured efficiencies in the fully degraded state in the range of $(19.0 \pm 0.5)\%$ and efficiencies after dark annealing in the range of $(19.4 \pm 0.5)\%$. Again, each solar cell was in the dark-annealed state before it was embedded into the mounting bracket. A forward-bias voltage V_{appl} is applied to the solar cell and kept constant over sense contacts during the entire experiment after reaching the thermal equilibrium of 140°C after 30 mins. The cell current is measured by a voltage drop over a resistance R ($0.1\ \Omega$). Because of the $25 \times 25\ \text{mm}^2$ small solar cells, we can vary V_{appl} up to $580\ \text{mV}$ with the set-up B for the in-situ measurements of I_{cell} and the EL intensity Φ_{EL} , before the current limit of the power supply is reached because of the increased cell current at increased temperatures. The EL signal is measured

using a silicon charge-coupled device (Si-CCD) camera (Sensicam QE, PCO). Each regeneration run is carried out in darkness at different constant applied voltages during regeneration at a temperature of 140 °C.

4.3 In-situ measured degradation and regeneration kinetics

At first, in-situ regeneration experiments are carried out in darkness by using set-up A. Figures 4.6 and 4.7 show the time evolution of the dark-injected cell current I_{cell} , which is directly proportional to the total recombination rate versus the logarithmically plotted time at the applied voltages V_{appl} .

In Fig. 4.6, the typical degradation behavior at room temperature known from the BO defect activation under illumination is observed.

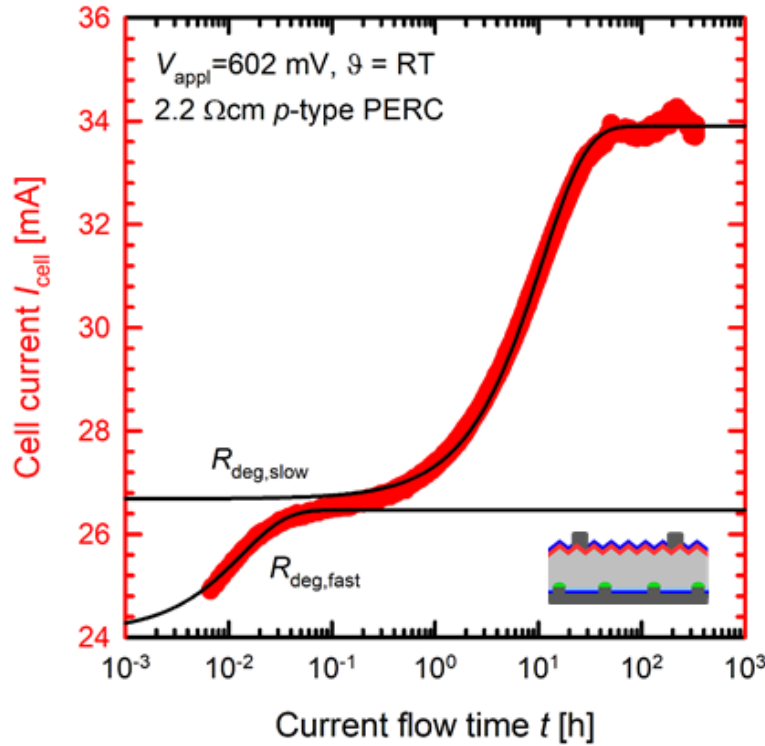


Figure 4.6: The typical two-stage degradation, as known from the literature [41], can also be observed in the dark cell current, if a constant forward-bias voltage (in this case $V_{\text{appl}} = 602 \text{ mV}$) is applied to the cell at room temperature.

For the fast initial increase of the cell current, we determine a rate constant of $R_{\text{deg,fast}} = 2.1 \times 10^{-2} \text{ s}^{-1}$ and for the second, slower rate constant we determine $R_{\text{deg,slow}} = 2.6 \times 10^{-5} \text{ s}^{-1}$. These rate constants, $R_{\text{deg,fast}}$ and $R_{\text{deg,slow}}$, are in excellent agreement with the fast and slow generation rate constants of the light-induced BO defect activation $R_{\text{deg,fast}} = 3 \times 10^{-2} \text{ s}^{-1}$ and $R_{\text{deg,slow}} = 3 \times 10^{-5} \text{ s}^{-1}$ as published in the literature [41], which is an indication of the proper functioning of our measurement setup. Interestingly, also the regeneration, as shown in Fig. 4.7 at 140 °C, proceeds with a double-exponential process with a fast and a slow component, corresponding to a decreasing cell current.

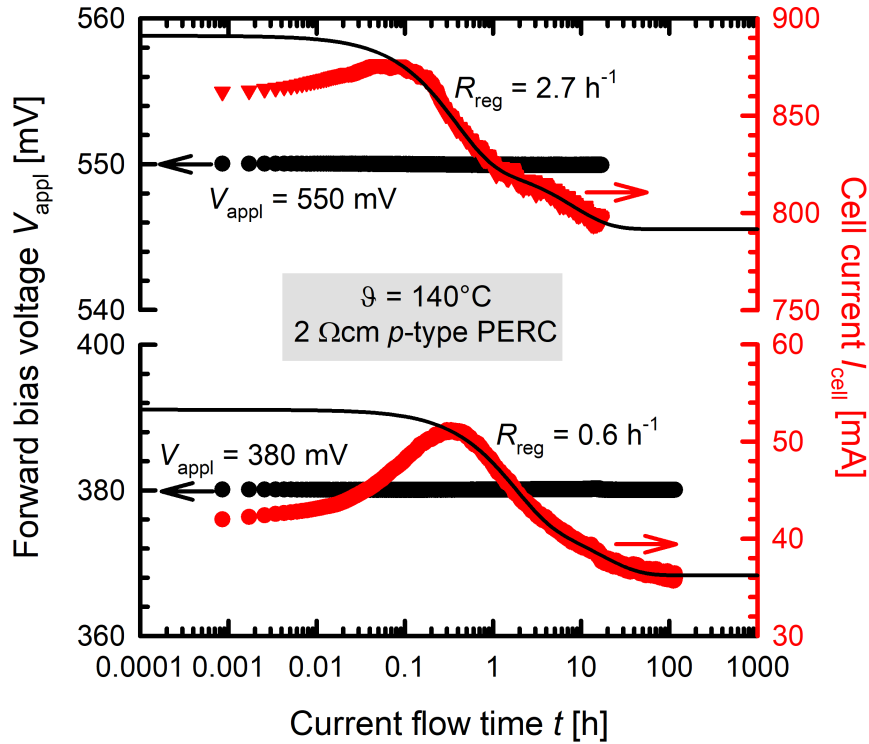


Figure 4.7: Evolution of the cell current I_{cell} under two different constant applied forward-bias voltages V_{appl} at 140°C in darkness. The solid black lines show fits of double-exponential decay functions. V_{appl} is kept constant during each regeneration experiment.

This double-exponential behavior is not observed if the regeneration is performed in the traditional way, i.e. if the I - V measurements are performed after cooling down to room temperature [83]. Only the fast component is increasing with increasing V_{appl} at the chosen regeneration temperature. The slow component shows no dependence on the forward-bias voltage and seems to be a kind of measurement artefact not related to bulk recombination. Hence, we relate only the fast component to the regeneration kinetics of the boron-oxygen defect. However, the efficiency of the solar cells is the same in the dark-annealed state and after complete dark regeneration through current feed (see Fig. 4.8), which confirms the proper functioning of our methodology. Hence, we identify the fast component of the regeneration rate with the regeneration rate constant R_{reg} of the BO-related regeneration.

Fig. 4.8 shows exemplarily the evolution of the efficiency η and the open-circuit voltage V_{oc} of one solar cell after electronically stimulated regeneration in the dark (filled blue square) during illumination with an intensity of $P_{\text{ill}} = 10 \text{ mWcm}^{-2}$ (0.1 suns) at room temperature. Also shown are the fully degraded (filled gray circle) and the dark-annealed states (filled red triangle). The direct comparison reveals that the efficiency η as well as the open-circuit voltage V_{oc} after electronic regeneration and the values after dark-annealing are practically the same. These results clearly prove for the first time that the solar cells have in fact been permanently regenerated by means of electron injection via current feeding in darkness and that photons are not a necessary prerequisite in the regeneration process, if electrons are generated alternatively.

The fast component of regeneration, in the following called regeneration rate con-

stant R_{reg} , is obtained from double-exponential fits to the in-situ-measured regeneration curves by set-up A.

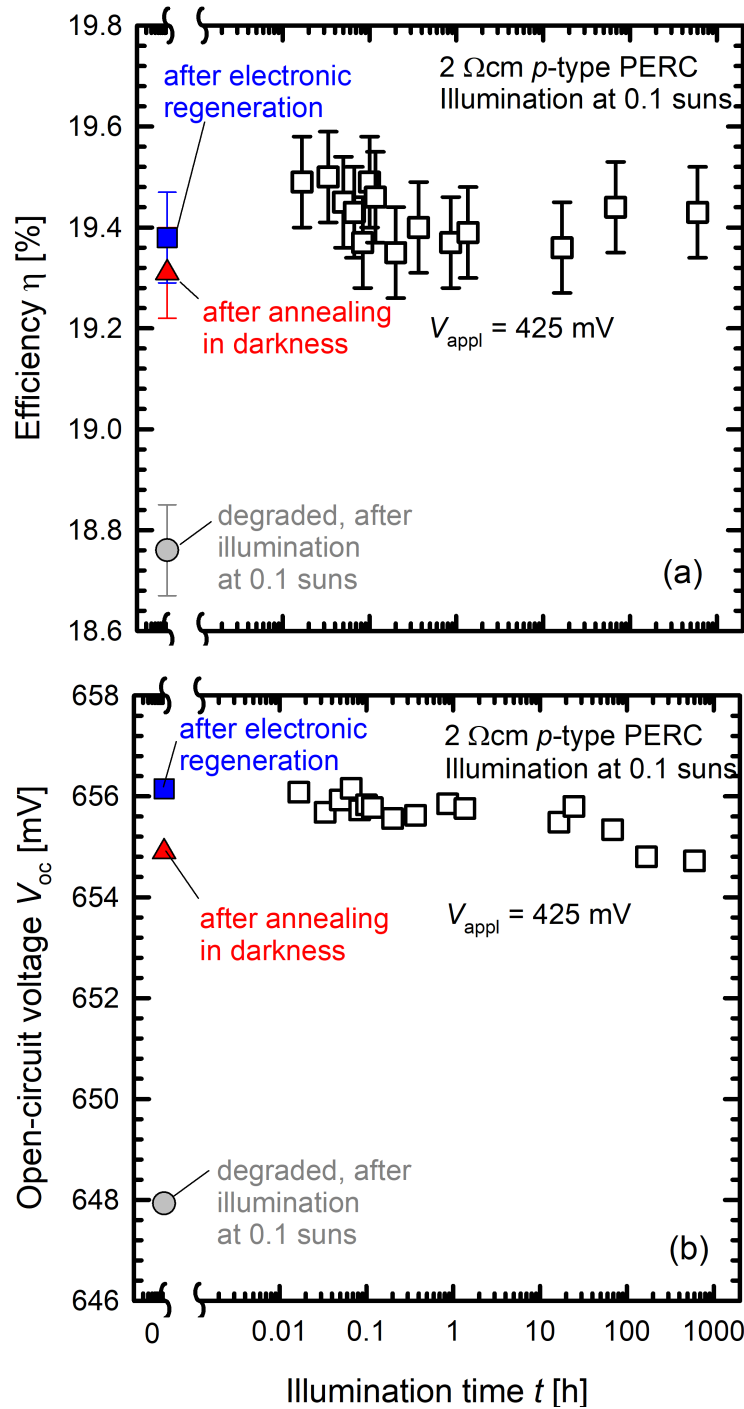


Figure 4.8: Evolution of (a) efficiency η and (b) open-circuit voltage V_{oc} after regeneration by electron injection in the dark (squares). In comparison, the degraded state (circle, gray data point) and the dark-annealed state (triangle, red data point) are shown. The scatter of measurement data refer to the reproducibility by the contacting of the solar cell.

The measured regeneration kinetics by set-up B proceeds mono-exponentially (see Fig. 4.11) until a minimum in the recombination rate (regenerated state) is reached,

4.4 Determination of the excess carrier concentration via EL

which confirms the assumption that the measured slow component by set-up A is a kind of measurement artefact. The extracted regeneration rates from current feeding by set-up A and B for low applied voltages are comparable and in the same order of magnitude, i. e. for a constant applied voltage V_{appl} of 380 mV by set-up A we obtain $R_{\text{reg}} = 0.6 \text{ h}^{-1}$ and by set-up B we obtain $R_{\text{reg}} = 0.4 \text{ h}^{-1}$. For a constant applied voltage V_{appl} of 425 mV we obtain $R_{\text{reg}}(\text{set-up A}) = 1.1 \text{ h}^{-1}$ and $R_{\text{reg}}(\text{set-up B}) = 1.5 \text{ h}^{-1}$ as another example.

Only a comparison of the rates for low applied voltages can be performed, since in this case the applied voltage V_{appl} equals the local voltage V_i at the p - n junction without an influence of the series resistance. In Fig. 4.9, dark I - V characteristics are shown of neighboured small solar cells of the same large laser-cut solar cell, measured at 140°C by set-up A and B. Above 450 mV, the series resistance R_S has an influence on the local voltage at the p - n junction V_i and V_i does not equal V_{appl} .

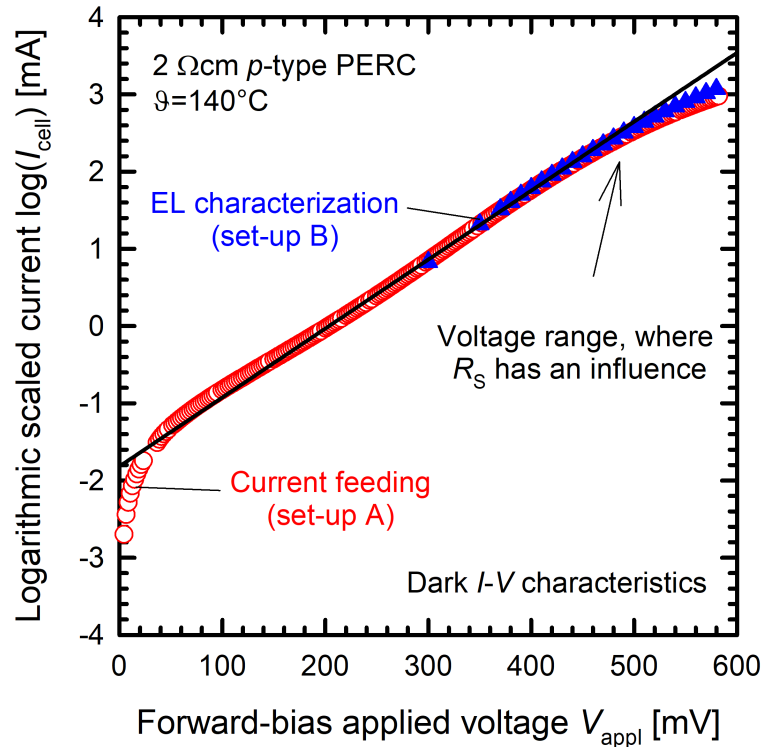


Figure 4.9: Dark I - V characteristics measured at 140°C by set-up A shown as red circles and set-up B shown as blue triangles.

In order to determine the excess carrier concentration injected in the cell base during regeneration, we directly measure the emitted EL signal at different time steps during the regeneration of the cell.

4.4 Determination of the excess carrier concentration via EL

As mentioned above (see Section 2.1.2), the camera-recorded EL intensity $\Phi_{i,\text{EL}}$ is directly proportional to the excess carrier concentration Δn in the solar cell base under low-injection conditions. We determine Δn via a calibration constant C_i and

the effective local junction voltage V_i . The calibration constant C_i is extracted from a luminescence image (see e.g. Fig. 4.5) measured at conditions, where the current is as low as possible but an EL signal with sufficiently low signal-to-noise ratio can still be measured. Under these conditions, it can be assumed that the applied voltage V_{appl} equals the local voltage V_i at the p - n junction. In these experiments, we determine C_i at a voltage of 300 mV, where our measurements showed that the series resistance has no impact on the EL image (see Fig. 4.9). The EL intensity $\Phi_{i,\text{EL}}$ is arithmetically averaged next to the busbar (see Figure 4.5(b)).

The effective local junction voltage V_i during regeneration is determined by the measured averaged EL intensity $\Phi_{i,\text{EL}}$ at each applied forward-bias voltage V_{appl} using Equ. (4.1) with the thermal voltage V_{th} (at 140 °C in these experiments, i.e., $V_{\text{th}} = 35.6$ mV) and the previously determined calibration constant C_i [84]:

$$V_i = V_{\text{th}} \times \ln(\Phi_{i,\text{EL}}/C_i) \quad . \quad (4.1)$$

In the case of the injection of charge carriers by applying a forward-bias voltage, the diode equation

$$n \times p = n_i^2 \times \left(\exp\left(\frac{V_i}{V_{\text{th}}}\right) - 1 \right) \quad (4.2)$$

with the intrinsic carrier concentration n_i and the equation

$$n \times p = (\Delta n + n_0)(\Delta p + p_0) \quad , \quad (4.3)$$

apply with $n = \Delta n + n_0$ and $p = \Delta p + p_0$ for the total electron concentration n and the total hole concentration p and n_0 and p_0 being the equilibrium concentrations of electrons and holes, respectively. Assuming that charge neutrality holds ($\Delta n = \Delta p$) and neglecting n_0 ($n_0 \ll p_0$) for a p -type silicon base, we obtain instead of Equ. (4.3)

$$n \times p = \Delta n^2 + \Delta n \times p_0 \quad , \quad (4.4)$$

with p_0 being the doping concentration N_A . Equating the Eqs. (4.2) and (4.4) and solving the resulting quadratic equation, the ratio between the effective local junction voltage V_i and the injected excess carrier concentration Δn can be described by

$$\Delta n = -N_A/2 + \sqrt{(N_A/2)^2 + n_i^2 \times (\exp(V_i/V_{\text{th}}) - 1)} \quad , \quad (4.5)$$

where we use the intrinsic carrier concentration n_i according to Misiakos and Tsamakis [85] and $N_A = p_0$ is the doping concentration.

By using Eqs. (4.1) and (4.5), the injected charge carrier concentration is determined via the measured EL signal of one of the p -type PERC solar cells at different applied forward-bias voltages V_{appl} at elevated temperature. The EL intensities $\Phi_{i,\text{EL}}$ next to the busbar are plotted versus V_{appl} , respectively the local junction voltage V_i , as filled triangles in Fig. 4.10(a) and refer to the left y-axis. As can be seen from Fig. 4.10, the EL intensity increases proportionally to the applied voltage. An increasing V_{appl} means an increasing injected excess carrier concentration Δn . The lower x-axis in Fig. 4.10 corresponds to the applied forward-bias voltage V_{appl} and the upper x-axis to the local voltage V_i at the p - n junction. Using Eqs. (4.1) and (4.5), the excess carrier concentration Δn corresponding to each applied voltage is

4.4 Determination of the excess carrier concentration via EL

calculated. The resulting Δn values obtained from the measured EL are shown as filled circles in Fig. 4.10(a), referring to the right y-axis.

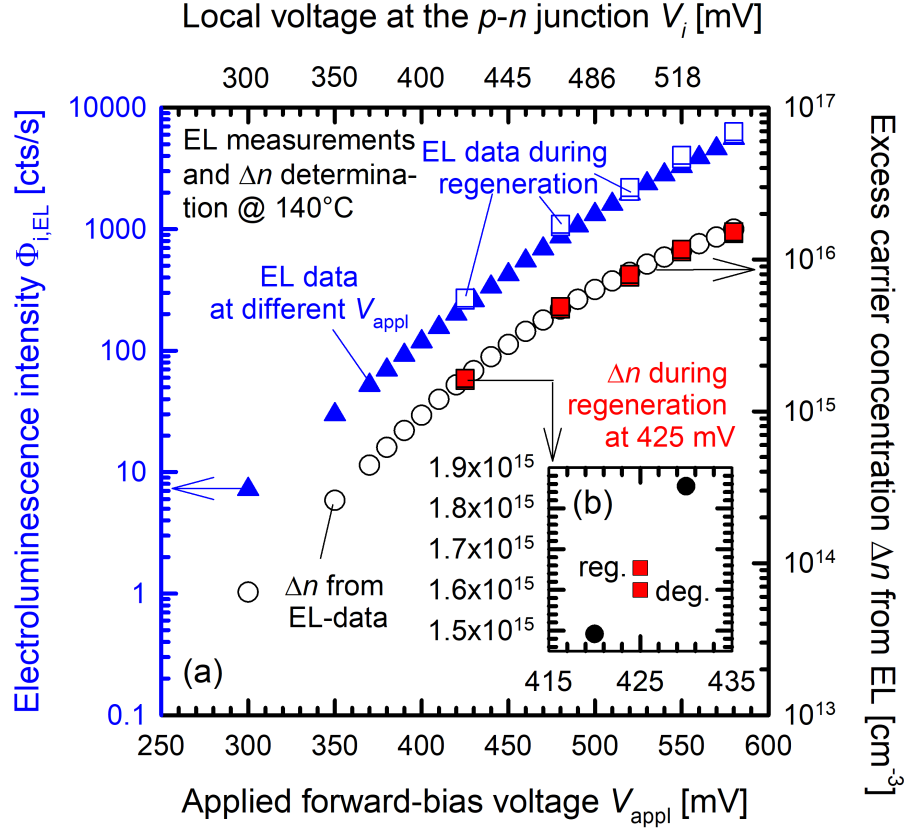


Figure 4.10: (a) Left y-axis shows the measured EL intensities $\Phi_{i,EL}$ at different applied voltages V_{appl} at 140°C and of three exemplary regeneration curves. The lower x-axis corresponds to the voltage applied to the solar cell during regeneration, which is kept constant over sense contacts. The upper x-axis corresponds to the locally applied voltage at the p - n junction V_i . From the measured EL intensities (filled triangles), the injected excess carrier concentration Δn (open circles) can be determined in dependence of the applied voltages. These data refer to the right y-axis. (b) Excess carrier concentration Δn is practically constant during regeneration (filled squares). The Δn value is in the regenerated state (reg.) slightly higher than in the degraded state (deg.).

By the same method, we determine Δn during regeneration. As shown in Fig. 4.11(a), the EL signal, emitted by the solar cell during regeneration ($V_{appl} = \text{const.}$), is measured under regeneration conditions in darkness and shows an opposite kinetics to the cell current I_{cell} (which is proportional to the overall recombination rate in the cell). In the beginning, the cell current is rising and the EL intensity is decreasing because of the activation of the BO defect (degradation) prior to deactivation [86]. The regeneration starts at a high cell current, which corresponds to the completely degraded state of the solar cell and, hence, the maximum recombination rate. The regeneration kinetics proceeds monoexponentially until a minimum in the recombination rate is reached, which corresponds to the fully regenerated state. This evolution can be described by a monoexponential fit with a single regeneration rate constant R_{reg} : $I_{cell} = I_{cell,0} \times \exp(-R_{reg} \times t) + c$.

The cell current after full regeneration by current injection is lower than after an-

nealing in darkness, which means that the regeneration has improved the solar cell performance compared with the dark-annealed state. This seems to be an effect at increased measurement temperature, which needs to be further investigated. If the solar cells are characterized at room room temperature, the measured efficiencies and EL intensities of the solar cells are the same in the annealed initial state and after dark regeneration through current feeding, which confirms the proper functioning of our methodology. EL and I - V measurements were carried out at various constant applied forward-bias voltages V_{appl} during regeneration of several solar cells.

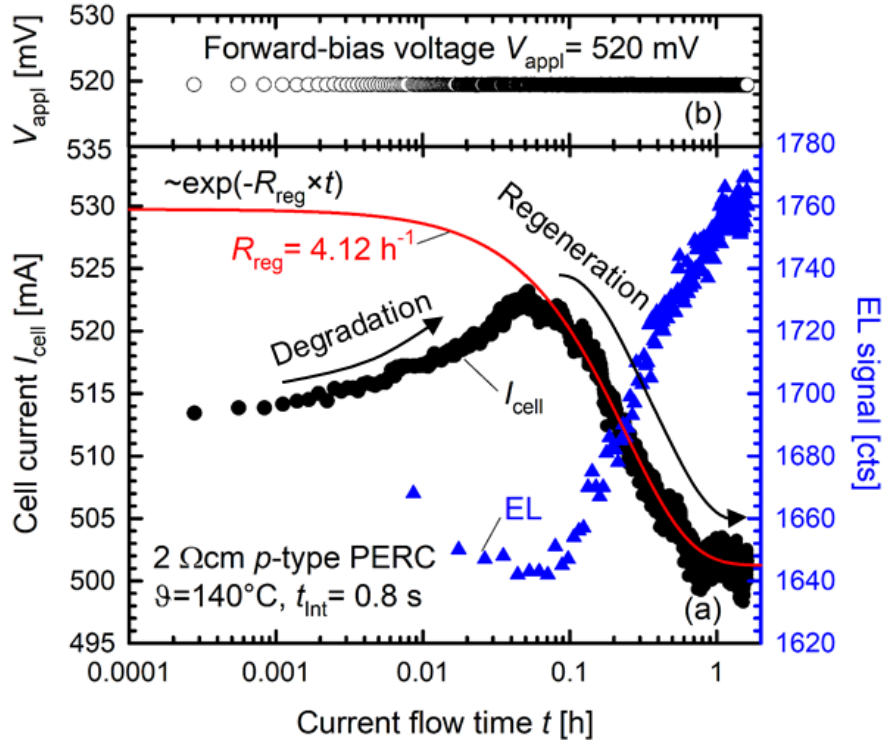


Figure 4.11: *In-situ* EL and I - V measurements during regeneration at elevated temperatures. (a) Current through the cell I_{cell} (filled circles) measured at 140°C and an applied voltage of $V_{\text{appl}} = 520\text{ mV}$ proceeds in the opposite direction to the EL curve (filled triangles). In this case, the exposure time t_{Int} of the voltage is about 0.8 s . The regeneration curve (red line) can be described by one regeneration rate constant R_{reg} . (b) Forward-bias voltage (open circles) is constantly applied.

In Figure 4.10(a), the measured EL data during regeneration are exemplarily shown for five regeneration experiments carried out at five different applied voltages (425 , 480 , 520 , 550 and 580 mV) as open squares. The extracted Δn values from the measured EL intensities using Eqs. (4.1) and (4.5) are shown as filled squares in Figure 4.10(a). Exemplarily for each regeneration experiment, the inset of Figure 4.10(b) shows the minimum (degraded state) and the maximum (regenerated state) of Δn for a regeneration carried out at 425 mV . In the degraded state, the recombination rate is increased resulting in a lower Δn (and hence a lower EL signal). In the regenerated state, a reduced recombination rate and, hence, an increased EL signal are obtained. These two values indicate that the variation in Δn during the regeneration process is smaller than 10% and hence, can be regarded as almost constant. In the logarithmic plotting in Figure 4.10(a), this small difference is not resolved.

4.5 Regeneration rate constant as a function of excess carrier concentration

In Fig. 4.12, the measured regeneration rate constants R_{reg} are plotted versus the excess carrier concentrations Δn deduced from the EL measurements for regenerations at various applied voltages (red squares for $2\ \Omega\text{cm}$ and green diamonds for $2.5\ \Omega\text{cm}$ Cz-Si PERC cells). Exemplarily, the effective local junction Voltage V_i is shown for some data points, as determined by the measured averaged EL intensity using Equ. (4.5).

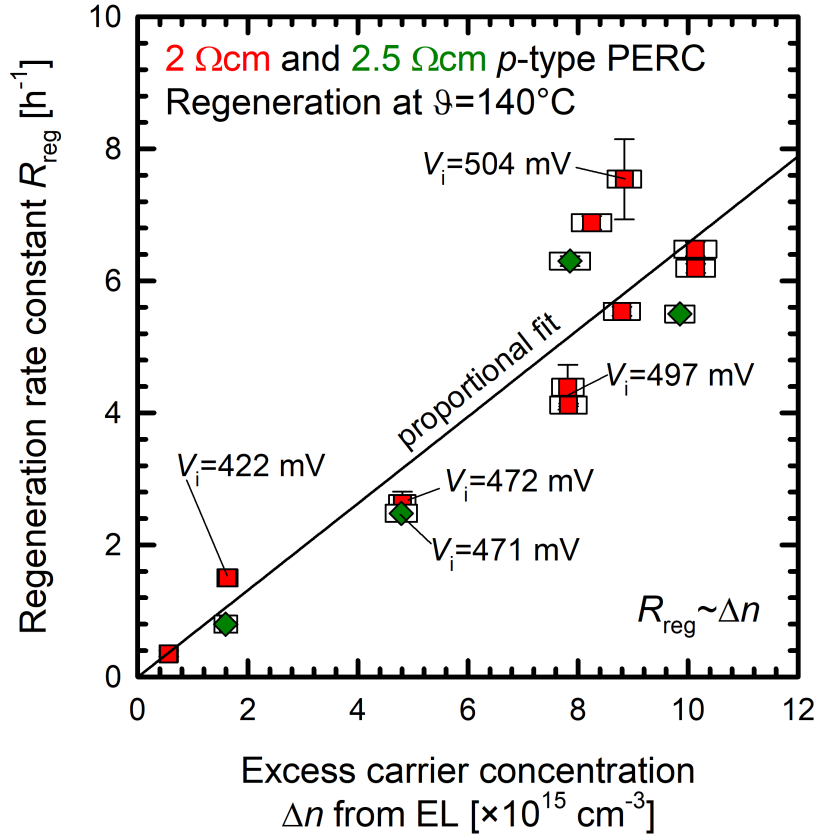


Figure 4.12: Determined regeneration rate constant R_{reg} versus the excess carrier concentration Δn (symbols) from EL shows a proportional increase. The red squares show measurements on $2\ \Omega\text{cm}$ and the green diamonds on $2.5\ \Omega\text{cm}$ PERC cells.

As already discussed earlier, there is a certain Δn range during regeneration according to the degraded and regenerated state (see Fig. 4.10(b)). This Δn range is shown as white bars in Fig. 4.12 for each applied voltage. The white bars clearly show that the injected Δn is almost constant during regeneration by applying a constant voltage. By applying the same local junction voltage V_i to nominally identical solar cells (stemming from one wafer, e.g., filled squares), the regeneration proceeds with almost the same R_{de} , as exemplarily shown for $V_i = 497\ \text{mV}$. This is because of the fact that the same voltage corresponds to the same injected carrier concentration Δn . With an increasing applied voltage, we inject an increasing excess carrier concentration Δn . Fig. 4.12 shows that our measurement data indeed follow a proportional dependence of R_{reg} on the injected Δn . The solid line in Fig. 4.12 corresponds to the following proportional fit to the measured data:

$$R_{\text{reg}}[\text{h}^{-1}] = 0.66[\text{cm}^3 \times \text{h}^{-1}] \times \frac{\Delta n}{10^{15}}[\text{cm}^{-3}] \quad . \quad (4.6)$$

Equ. (4.6) is valid for the $2.0 \Omega\text{cm}$ PERC solar cells (see red squares in Fig. 4.12), which were fired in an industrial-type belt furnace [87] with a belt speed of 5.6 m/min . In addition, we examined some $2.5 \Omega\text{cm}$ Cz-Si PERC solar cells (see green diamonds in Fig. 4.12), which were fired with a belt speed of 6.8 m/min . In this doping range and with this small difference in the belt speeds, the cells seem to behave similarly in their regeneration kinetics, as exemplarily shown for $V_i \approx 470 \text{ mV}$. The same proportional relation between R_{reg} and Δn applies. Note that the $2.0 \Omega\text{cm}$ and $2.5 \Omega\text{cm}$ Cz-Si samples have similar oxygen concentrations in the range of $(6 - 7) \times 10^{17} \text{ cm}^{-3}$.

4.6 In-situ regeneration experiments of lifetime samples

In additional experiments, lifetime measurements were carried out directly at the regeneration temperature using the WCT-120TS measurement system of Sinton Instruments with a temperature-controlled sample stage [88].

As can be seen in Figure 4.13(b) at the actual regeneration conditions of 1.3 suns at 170°C , the lifetime is almost constant. This is consistent with the proportional dependence of R_{reg} on the excess carrier density and consequently the lifetime: $R_{\text{reg}} \propto I_{\text{ill}} \propto \Delta n \propto \tau$. The excess carrier concentration and the lifetime are not changing during illuminated annealing, clearly agreeing with the prediction of Voronkov and Falster [9] from their permanent deactivation model.

Thus the real physical conditions of the regeneration have to be considered to solve the inconsistency of a constant regeneration rate constant and changing excess carrier densities and lifetimes at room temperature.

4.7 Chapter summary

In this chapter, we have for the first time investigated the regeneration process in boron-doped p -type Czochralski-grown silicon (Cz-Si) by current injection into solar cells in darkness at elevated temperature, under actual regeneration conditions. Typical industrial PERC solar cells were examined in darkness at different applied forward bias voltages V_{appl} , which define the electron concentration injected into the solar cell base via the p - n junction. The in-situ measurements of the total recombination current of the cells combined with the illuminated I - V characteristics showed a successful permanent regeneration.

Based on EL measurements, we have experimentally determined the excess carrier concentrations Δn in Cz-Si PERC solar cells during regeneration at 140°C for different applied forward-bias voltages. The regeneration kinetics of the solar cells were

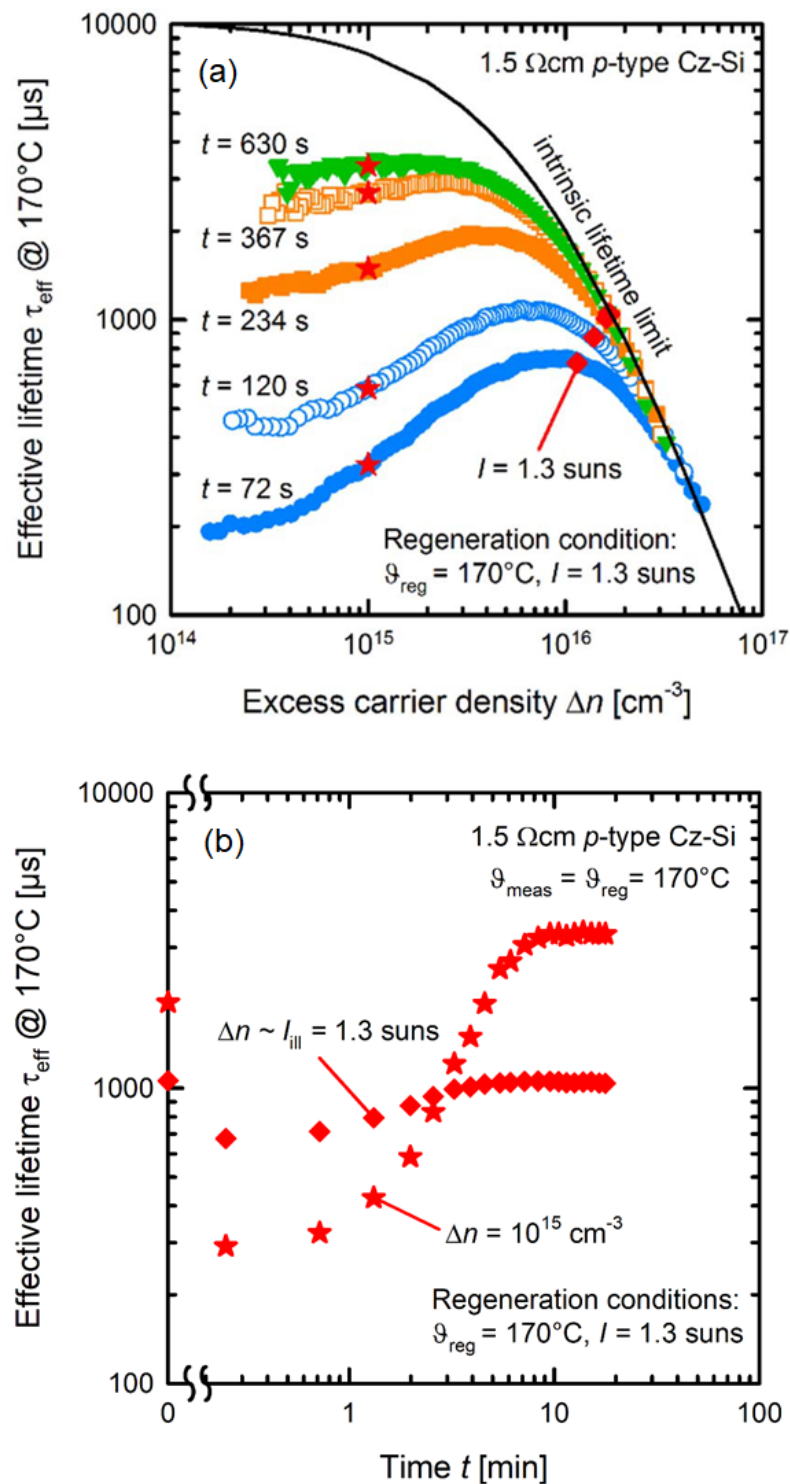


Figure 4.13: Lifetime evolution during regeneration measured at the regeneration temperature. (a) Injection-dependent lifetime measurements after different times of illuminated annealing with stars indicating lifetimes at $\Delta n = 1 \times 10^{15}$ cm⁻³ and diamonds indicating lifetimes at a constant illumination intensity of 1.3 suns. (b) Extracted lifetime evolutions at $\Delta n = 1 \times 10^{15}$ cm⁻³ and $I_{\text{ill}} = 1.3$ suns, taken from [88].

in-situ measured by recording the time-dependent electrical cell current during regeneration. From the latter measurements, the regeneration rate constant R_{reg} was determined by mono-exponential fitting to the measured data. A proportional increase of R_{reg} on Δn was observed, clearly agreeing with the prediction of Voronkov and Falster [9] from their permanent deactivation model showing that the regeneration rate constant is controlled by the injected excess carrier concentration Δn alone and photons are not required.

5 Impact of hydrogen on the boron-oxygen-related lifetime degradation and regeneration kinetics

Stacks of hydrogen-lean aluminum oxide, deposited via plasma-assisted atomic-layer-deposition, and hydrogen-rich plasma-enhanced chemical vapor-deposited silicon nitride (SiN_x) are applied to boron-doped float-zone silicon wafers. A rapid thermal annealing (RTA) step is performed in an infrared conveyor-belt furnace at different set-peak temperatures. The hydrogen content diffused into the crystalline silicon during the RTA step is quantified by measurements of the silicon resistivity increase due to hydrogen passivation of boron dopant atoms. These experiments indicate that there exists a temperature-dependent maximum in the introduced hydrogen content. The exact position of this maximum depends on the composition of the SiN_x layer. The highest total hydrogen content, exceeding 10^{15} cm^{-3} , is introduced into the silicon bulk from silicon-rich SiN_x layers with a refractive index of 2.3 (at a wavelength $\lambda = 633 \text{ nm}$) at an RTA peak temperature of 800°C , omitting the Al_2O_3 interlayer. Adding an Al_2O_3 interlayer with a thickness of 20 nm reduces the hydrogen content by a factor of four, demonstrating that Al_2O_3 acts as a highly effective hydrogen diffusion barrier. Measuring the hydrogen content in the silicon bulk as a function of Al_2O_3 thickness at different RTA peak temperatures provides the hydrogen diffusion length in Al_2O_3 as a function of measured temperature.

We examine the impact of hydrogen on the boron-oxygen-related lifetime degradation and regeneration kinetics in boron-doped *p*-type Czochralski-grown silicon wafers. We introduce the hydrogen into the silicon bulk by rapid thermal annealing. The hydrogen source are hydrogen-rich silicon nitride ($\text{SiN}_x : \text{H}$) layers. Aluminum oxide (Al_2O_3) layers of varying thickness are placed in-between the silicon wafer surfaces and the $\text{SiN}_x : \text{H}$ layers. By varying the Al_2O_3 thickness, which acts as an effective hydrogen diffusion barrier, the hydrogen bulk content is varied over more than one order of magnitude. The hydrogen content is determined from measured wafer resistivity changes. In order to examine the impact of hydrogen on the degradation kinetics, all samples are illuminated at a light intensity of 0.1 suns near room temperature. We observe no impact of the in-diffused hydrogen content on the degradation rate constant, confirming that hydrogen is not involved in the boron-oxygen degradation mechanism. The regeneration experiments at 160°C and 1 sun, however, show a clear dependence on the hydrogen content with a linear increase of the regeneration rate constant with increasing bulk hydrogen concentration. However, extrapolation of our measurements toward a zero in-diffused hydrogen content shows that the regeneration is still working even without any in-diffused hydrogen. Hence, our measurements demonstrate that there are two distinct regeneration processes

taking place. This is in good agreement with a recently proposed defect reaction model and is also in agreement with the finding that the permanent boron-oxygen deactivation also works on non-fired solar cells, though at a lower rate.

5.1 Introduction

Münzer et al. [65] were the first who assumed hydrogen to be involved in the permanent deactivation of the boron-oxygen defect, others followed [66, 89]. Gläser et al. [69] and Wilking et al. [68] reported that the boron-oxygen (BO) deactivation rate constant, or rather the regeneration rate constant R_{reg} , increases with increasing hydrogen concentration in the silicon bulk. However, in other studies [55, 67] no direct impact of hydrogen on the deactivation was observed. All studies had in common that no direct measurements of the actual hydrogen content in the silicon bulk had been performed. In 2019, a method was introduced by Walter et al. [70] to directly measure the hydrogen concentration in the silicon bulk via simple resistivity measurements. This enables now to quantitatively study the impact of hydrogen on the BO activation and deactivation kinetics. These experiments, carried out for the first time in this thesis, are suitable to resolve the contradicting statements reported in the literature with respect to the impact of hydrogen on the regeneration of the boron-oxygen-limited lifetime in boron-doped Cz-Si, as used in a large fraction of industrial silicon solar cells today.

In silicon-based solar cells, the introduction of Al_2O_3 surface passivation layers was a crucial step towards higher efficiencies of industrial solar cells in recent years. The metal contacts in today's industrial silicon solar cells are made by screen-printing of metal pastes in combination with a subsequent rapid thermal annealing (RTA) step, frequently called "fast-firing", at set-peak temperatures in the range between 750 and 850 °C for a few seconds [82]. To preserve the excellent passivation quality of the atomic-layer deposited (ALD) Al_2O_3 layers on the silicon surface during the RTA step, the Al_2O_3 layers are capped by silicon nitride ($\text{SiN}_x\text{:H}$) layers. These top layers are grown by means of plasma-enhanced chemical vapor deposition (PECVD) resulting in amorphous $\text{SiN}_x\text{:H}$ layer with very high hydrogen content (typically in the range of 10–20 at%)[90]. In contrast, ALD- Al_2O_3 layers have a hydrogen content in the range of only 1–2 at% [27]. During the RTA step, hydrogen partly diffuses from the hydrogen-rich SiN_x layer [91] through the Al_2O_3 layer to the interface and also into the crystalline silicon bulk, where it is able to passivate defects [92–94]. Interestingly, the hydrogen was also found to be able to create new recombination centers in the silicon bulk, in some cases leading to a severe degradation in solar cell efficiency during illumination [3, 95–98]. Therefore, in photovoltaics, the control of the amount of hydrogen diffusing into the crystalline silicon bulk has turned out to be of utmost importance. There have been conjectures in the literature that Al_2O_3 layers might severely hamper the in-diffusion of hydrogen from $\text{SiN}_x\text{:H}$ into the silicon bulk [68, 99]. However, these studies did not provide any quantitative measurements on how effective Al_2O_3 actually is as a hydrogen barrier.

In the following, we will quantify the amount of hydrogen diffused into the silicon bulk from hydrogen-rich silicon nitride layers $\text{SiN}_x\text{:H}$ with and without Al_2O_3 inter-

5.2 Experimental details

layers. This study allows us to introduce defined concentrations of hydrogen into the silicon bulk, enabling us to quantitatively examine the dependence of R_{reg} on the in-diffused hydrogen concentration for the first time.

5.2 Experimental details

We use (100)-oriented 300 μm thick 1.3 and 1.4 Ωcm boron-doped Float-zone silicon (Fz-Si) wafers as well as 1.1 Ωcm boron-doped Czochralski-grown silicon (Cz-Si) wafers. The $15.6 \times 15.6 \text{ cm}^2$ Cz-Si wafers and 6" Fz-Si wafers are first cleaned with a surface-active agent followed by an RCA cleaning sequence. To remove possible remaining metallic contaminants in the silicon bulk, the wafers are then phosphorus gettered in a quartz tube furnace (TS 81004, Tempres Systems) at 850 $^\circ\text{C}$ using POCl_3 . The resulting phosphosilicate glass layers and the n^+ -regions (n^+ sheet resistance 80 – 90 Ωsq^{-1}) on both wafer surfaces are removed by hydrofluoric acid and potassium hydroxide etching, respectively, so that the final wafer thickness amounts to $(141 \pm 2) \mu\text{m}$. The final thickness of both materials is identical to guarantee comparability between Cz- and Fz-Si samples. After laser-cutting the wafers into $2.49 \times 2.49 \text{ cm}^2$ large samples and another RCA cleaning, the samples are symmetrically passivated either by single layers of $\text{SiN}_x\text{:H}$ or by $\text{Al}_2\text{O}_3/\text{SiN}_x\text{:H}$ stacks on both surfaces. In addition, some samples are only passivated by 10 nm of aluminum oxide (Al_2O_3) on both wafer surfaces.

Silicon nitride ($\text{SiN}_x\text{:H}$) layers are deposited by remote plasma-enhanced chemical vapour deposition (remote PECVD) at 400 $^\circ\text{C}$ in a Plasmalab 80 Plus System (Oxford Instruments). The ammonia gas flow was set constant at 200 sccm and the nitrogen gas flow was set at 100 sccm. To vary the composition of the $\text{SiN}_x\text{:H}$ layers, and hence their refractive index n (measured by ellipsometry at a wavelength of $\lambda = 633 \text{ nm}$) to examine its impact on the hydrogen diffusion into the silicon bulk (see Section 5.4), we applied different silane gas flows. A silane gas flow of 1.2 sccm results in a refractive index of $n=1.9$, 8.5 sccm in $n=2.3$ and 15 sccm in $n=2.7$. All $\text{SiN}_x\text{:H}$ films had the same thickness of $(132 \pm 4) \text{ nm}$ by adjusting the deposition time. The Al_2O_3 layers are deposited by means of plasma-assisted atomic layer deposition (PA-ALD) in a FlexAL system (Oxford Instruments) at 200 $^\circ\text{C}$ using trimethylaluminum (TMA) and an oxygen plasma for oxidation in each cycle. By varying the number of cycles, the Al_2O_3 thickness is adjusted between 5 and 25 nm under a silicon-rich $\text{SiN}_x\text{:H}$ layer ($n=2.3$) to systematically examine the impact of the Al_2O_3 thickness on the hydrogen diffusion into the silicon bulk during the RTA step (see Section 5.5).

In the final process step, all samples received an RTA step on an underlay wafer (see Fig. 5.1(a)) in an industrial infrared conveyor-belt furnace (DO-FF-8.600-300, centrotherm AG) at different set-peak temperatures at a belt speed of 6.8 m min^{-1} . The actual sample temperature was measured by a type-K thermocouple (KMQXL-Imo50G-300, Omega) in combination with a temperature tracker (DQ1860A) from Datapaq. Figure 5.1(b) shows a typical temperature profile measured on a sample with $\text{Al}_2\text{O}_3/\text{SiN}_x\text{:H}$ stack. The measured peak temperature ϑ_{peak} was varied between 606 and 860 $^\circ\text{C}$.

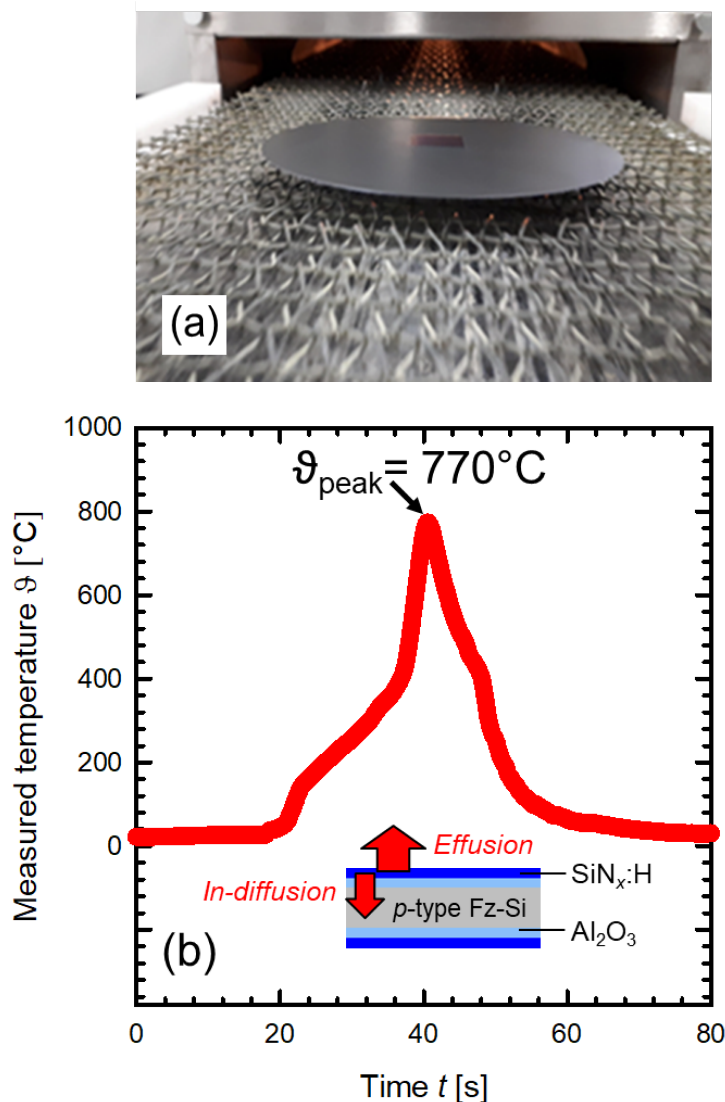


Figure 5.1: (a) Lifetime sample on an underlay wafer, which passes through the industrial belt-furnace. (b) Temperature profile measured on a sample with $\text{Al}_2\text{O}_3/\text{SiN}_x\text{:H}$ stack present during RTA, using a type-K thermocouple and temperature tracker from Datapaq.

5.3 Determination of hydrogen concentration via resistivity measurements

As already mentioned above, fast-firing (i.e. RTA) introduces hydrogen from the hydrogen-rich silicon nitride layer into the silicon bulk. Directly after RTA, the hydrogen is mainly present in the form of hydrogen dimers H_2 in the silicon bulk [81]. These H_2 dimers dissociate during low-temperature annealing in darkness (e.g., at 160°C) and the hydrogen atoms subsequently passivate the negatively charged boron dopant atoms [17]. As a consequence, the bulk resistivity ρ of the sample increases as a function of time during dark annealing at 160°C on a hotplate (see Fig. 5.2). We measure the resistivities in-between the periods of 160°C -dark annealing using the eddy-current method by inductive coupling of the sample to a WCT-

120 bridge (Sinton Instruments). The sample temperature is recorded during each measurement and the resistivities are extrapolated to 25 °C (see Section 2.1.4), as described in detail by Walter et al.[70]. The higher the saturation value of the measured base resistivity, the higher is the hydrogen-boron (HB) pair concentration and thus the hydrogen concentration in the silicon bulk. Walter et al. showed that for silicon material of the used boron concentration, the saturated HB concentration can be identified with the total hydrogen content $[H_{\text{tot}}]$ in the silicon bulk [70]. The saturated hydrogen-boron concentration in the bulk $[HB]_{\text{sat}}$ can be calculated according to

$$[HB]_{\text{sat}} = p_0 - p_{\text{sat}} \quad (5.1)$$

with p_0 being the hole concentration before firing and p_{sat} being the saturated hole concentration after dark-annealing at 160 °C [70].

Figure 5.2 shows exemplary resistivity measurements for three samples with $\text{SiN}_x\text{:H}$ films of different compositions with refractive indices between 1.9 and 2.7, fired at a measured RTA peak temperature of (792 ± 10) °C.

5.4 Impact of RTA treatment and silicon nitride composition on hydrogen in-diffusion

Silicon-rich $\text{SiN}_x\text{:H}$ layers with $n=2.3$ result in the highest resistivity increase and hence the highest hydrogen concentration in the silicon bulk. Figure 5.3 shows the measured saturated hydrogen-boron concentration $[HB]_{\text{sat}}$ in the silicon bulk, which can be identified with the total hydrogen concentration for the silicon wafers of the examined resistivities, for three SiN_x layers with different compositions (corresponding to refractive indices of $n=1.9$, 2.3 and 2.7) as a function of the measured peak temperature ϑ_{peak} of the RTA step.

Whereas the nearly stoichiometric SiN_x layer with a refractive index of $n=1.9$ results in the lowest saturated hydrogen-boron concentration $[HB]_{\text{sat}}$ within the silicon bulk, increasing the silicon content in the SiN_x layer and thereby its refractive index to $n=2.3$ significantly increases $[HB]_{\text{sat}}$. A further increase in the silicon content of the SiN_x layers to $n=2.7$, however, decreases $[HB]_{\text{sat}}$ again. The maximum amount of hydrogen is hence introduced into the silicon bulk for the silicon-rich SiN_x layers with a refractive index of $n=2.3$, in agreement with the recent findings of Bredemeier et al. [19]. In addition, Fig. 5.3 demonstrates that the total hydrogen concentration in the silicon bulk critically depends on the peak temperature: At low peak temperatures, the hydrogen in-diffusion increases with increasing ϑ_{peak} , whereas at higher peak temperatures, the hydrogen in-diffusion decreases with increasing ϑ_{peak} . The maximum of the in-diffused total hydrogen concentration into the bulk as a function of ϑ_{peak} depends on the silicon content of the SiN_x layer. With increasing silicon content of the SiN_x layers, the maximum hydrogen content in the silicon bulk is detected at decreasing ϑ_{peak} values. Note that for the nearly stoichiometric SiN_x layers ($n=1.9$), the maximum seems to lie outside of our experimental peak temperature window. The maximum total hydrogen concentration of $1.5 \times 10^{15} \text{ cm}^{-3}$ is obtained at a peak temperature of (792 ± 10) °C for a silicon-rich SiN_x layer with $n=2.3$.

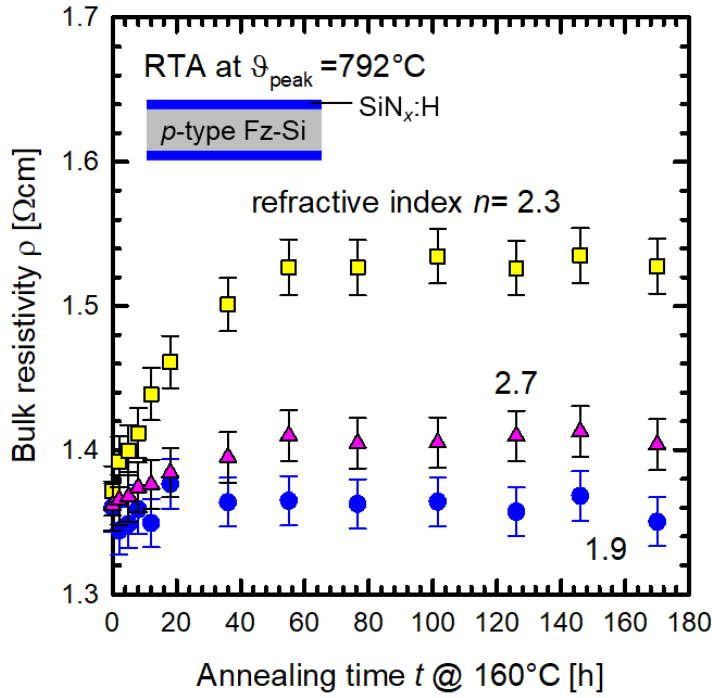


Figure 5.2: Measured evolution of the bulk resistivity ρ versus the annealing time at 160°C in the dark of $\text{SiN}_x\text{:H}$ -coated $1.4\ \Omega\text{cm}$ boron-doped Fz-Si samples, RTA-treated at a measured peak temperature ϑ_{peak} of $(792\pm 10)^\circ\text{C}$. The refractive index n of the SiN_x layer is varied between 1.9 (nearly stoichiometric SiN_x) and 2.7 (very silicon-rich SiN_x).

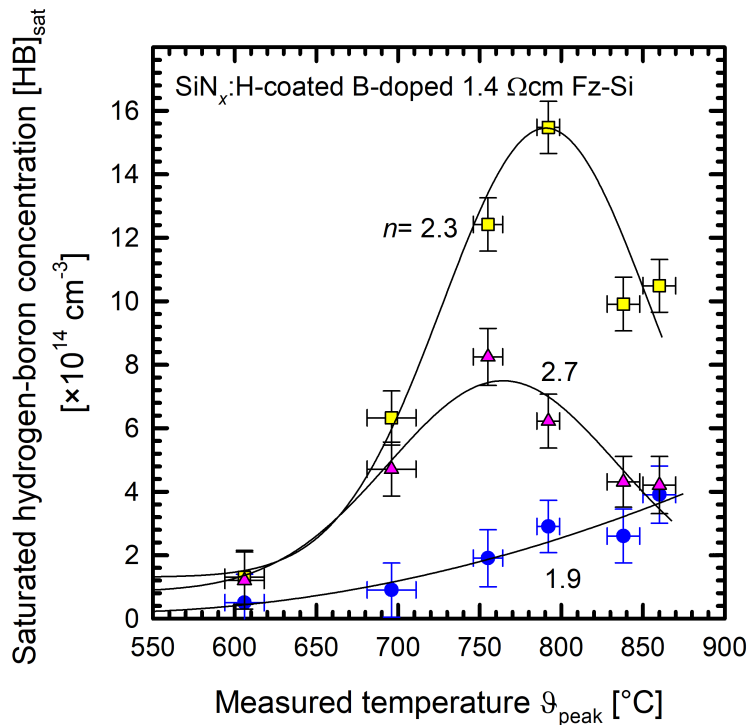


Figure 5.3: Saturated hydrogen-boron concentration $[\text{HB}]_{\text{sat}}$, which can be identified with the total hydrogen concentration, of SiN_x -coated $1.4\ \Omega\text{cm}$ boron-doped Fz-Si wafers after RTA treatment as a function of the peak temperature ϑ_{peak} measured during rapid thermal annealing (RTA). The solid lines are guides to the eyes.

To understand the temperature dependencies shown in Figure 5.3, we have performed Fourier-Transform Infrared Spectroscopy (FTIR, see Section 2.1.3) measurements of the different bondings in the SiN_x layers with $n=2.3$ before and after RTA. We use a Bruker VERTEX 70 FTIR spectrometer to measure the Si–N peaks at wave numbers $\bar{\nu}$ of 880 and 1030 cm^{-1} , the Si–H peak at $\bar{\nu} = 2180\text{ cm}^{-1}$, and the N–H peak at $\bar{\nu} = 3320\text{ cm}^{-1}$ [18]. The evaluation of the peaks is performed by using calibration constants from Yin and Smith [18] (see Table 2.1) based on the MATLAB program from Bredemeier et al. [16]. Figure 5.4 shows the relative losses of Si–H and N–H bond concentrations and the total hydrogen content within the SiN_x :H layers (see Equations (2.18)-(2.20)) as a function of the RTA peak temperature.

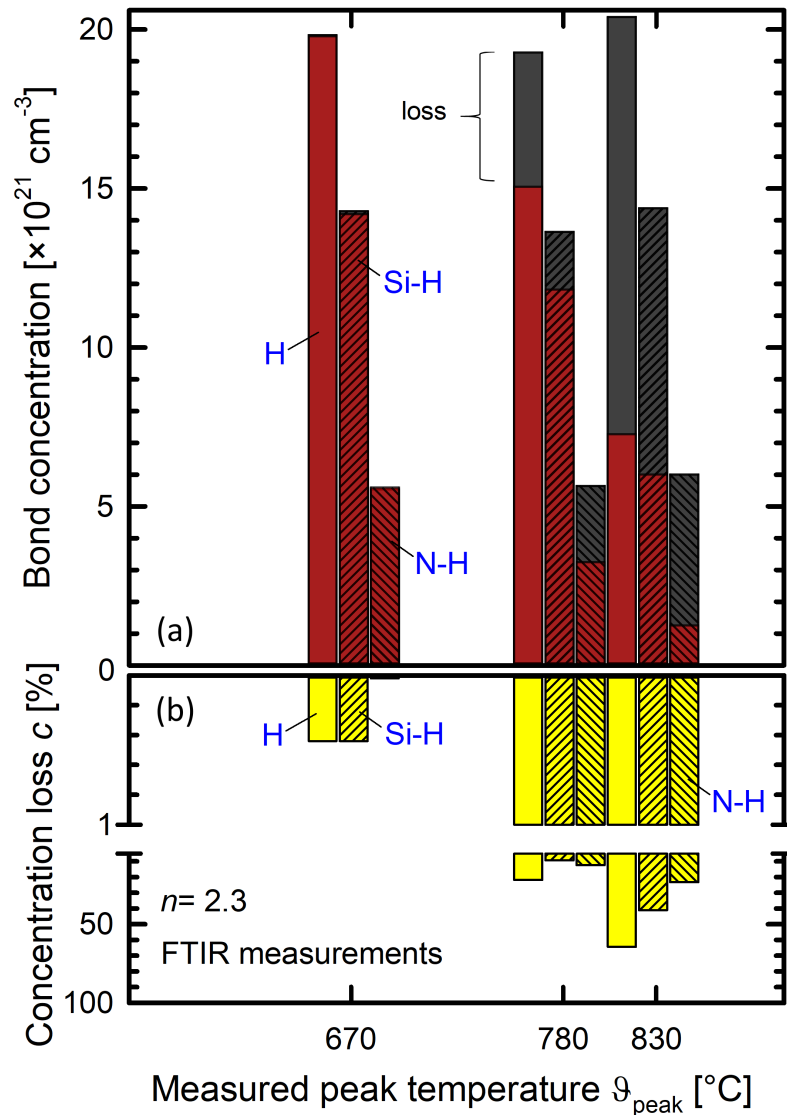


Figure 5.4: (a) Bond concentrations before (in black) and after firing (in red) in the SiN_x :H layers. (b) Percentage loss of Si–H (middle bar) and N–H bonds (right bar) in the SiN_x :H layers ($n=2.3$), and the total hydrogen (left bar) loss (sum of Si–H and N–H losses, solid) versus ϑ_{peak} . All concentrations are calculated from FTIR measurements.

After the RTA step at a measured peak temperature of $(670 \pm 10)^\circ\text{C}$, only a negligibly small loss in the Si–H bond concentration (-0.4%) is observed, whereas the N–H

bond concentration remains unchanged. Therefore, we can identify the total hydrogen loss in the $\text{SiN}_x\text{:H}$ layer with the loss in the Si–H bonds. After the RTA step at $\vartheta_{\text{peak}} = (780 \pm 10)^\circ\text{C}$, which is very close to the maximum hydrogen in-diffusion into the silicon bulk (see yellow squares in Figure 5.3), the N–H bond concentration in the $\text{SiN}_x\text{:H}$ film shows a pronounced decrease (-12.5%) as does the Si–H bond concentration (-9.4%). The overall hydrogen loss in the $\text{SiN}_x\text{:H}$ layer amounts therefore to -21.9% , which is two orders of magnitude larger than the hydrogen loss measured at 670°C . An RTA step at 830°C peak temperature results in the highest overall hydrogen concentration loss of -64.3% . Both, the Si–H and the N–H bond concentrations show a pronounced decrease by -41.0% and -23.3% , respectively. Despite these huge hydrogen losses in the $\text{SiN}_x\text{:H}$ layers during the RTA step, it should be kept in mind that the vast majority of hydrogen effuses into the atmosphere [34, 100] and only a very small portion diffuses into the silicon bulk. Nevertheless, our FTIR measurements demonstrate that at low temperatures ($<700^\circ\text{C}$), the dissociation of the weaker Si–H bonds governs the overall hydrogen out-diffusion and therefore also the diffusion into the silicon bulk. The relative loss of hydrogen in the $\text{SiN}_x\text{:H}$ layers is, however, very low ($<1\%$) at the low peak temperatures, which in turn also results in low hydrogen concentrations introduced into the silicon bulk. At higher peak temperatures ($>750^\circ\text{C}$), Si–H and N–H bonds dissociate in significant amounts as shown in Figure 5.4, leading to large hydrogen contents which are set free. This hydrogen mainly effuses out of the $\text{SiN}_x\text{:H}$ layers into the atmosphere, however, a small fraction also diffuses into the silicon bulk. For example at a measured peak temperature of $(780 \pm 10)^\circ\text{C}$ the total hydrogen loss in the $\text{SiN}_x\text{:H}$ layer by firing is about $4.22 \times 10^{21} \text{ cm}^{-3}$ (see Fig. 5.4(a)) and only $1.55 \times 10^{15} \text{ cm}^{-3}$ diffuses into the silicon bulk (see Fig. 5.3). At the maximum applied peak temperature of 830°C , the hydrogen loss is maximal, despite a reduction of hydrogen introduced into the silicon bulk (see Fig. 5.3). This hydrogen loss can probably be assigned to the reduction of the atomic density of the $\text{SiN}_x\text{:H}$ layer during RTA, because the nitrogen atoms make a greater contribution to the atomic density [101]. Our FTIR measurements show that after the RTA step at 830°C , the Si–N bond concentration decreases by 39.4% and so does the atomic density. As a consequence, the equilibrium shifts to the side of the effusion of the hydrogen into the atmosphere (hydrogen loss) and less hydrogen diffuses into the silicon bulk. This is also consistent with an increased blistering at firing temperatures exceeding 800°C , as can be seen in Figure 5.5.

Blistered area fractions (BAF) of the different $\text{SiN}_x\text{:H}$ layers were determined from light microscopy images for the different applied peak temperatures. The decrease in the measured bulk hydrogen content as a function of peak temperature for ϑ_{peak} values beyond the maximum hydrogen content (see Fig. 5.3) can be obviously correlated with an increased blistering (see Fig. 5.5) of the $\text{SiN}_x\text{:H}$ layers. Consequently, blistering seems to be a hydrogen loss mechanism occurring in our samples at the highest peak temperatures.

To examine the hydrogen barrier properties of Al_2O_3 films in-between the hydrogen-rich $\text{SiN}_x\text{:H}$ layer and the crystalline silicon bulk, in the following we apply the SiN_x layer with $n=2.3$, which led to the largest hydrogen content in the silicon wafer after RTA (in Fig. 5.3).

5.5 Impact of aluminum oxide thickness on hydrogen in-diffusion

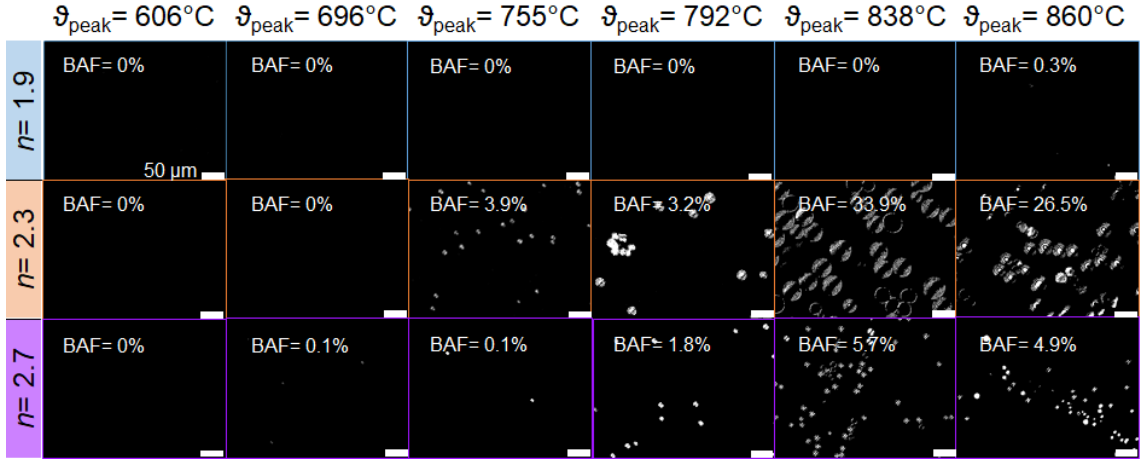


Figure 5.5: Light microscopy images (dark field) of the fired samples of Figure 5.3 for $\text{SiN}_x\text{:H}$ layers of three different refractive indices n and at different applied peak temperatures ϑ_{peak} . The blistered area fraction (BAF) of the different $\text{SiN}_x\text{:H}$ is obtained from light microscopy images for different applied different applied ϑ_{peak} .

5.5 Impact of aluminum oxide thickness on hydrogen in-diffusion

The Al_2O_3 layer thickness is varied in the range between 5 and 25 nm. To determine the total hydrogen concentration in the silicon bulk, the fired (i.e. RTA-treated) Fz-Si samples are dark-annealed at 160°C and their resistivity change is measured until saturation, from which the saturated hydrogen-boron concentration in the silicon bulk is calculated (see Section 5.3).

Figure 5.6 shows the evolution of the bulk resistivity ρ versus the annealing time for exemplary samples with an $\text{Al}_2\text{O}_3/\text{SiN}_x\text{:H}$ stack, fired at 770°C . The sample with 5 nm thick Al_2O_3 saturates at the highest resistivity, demonstrating that the highest hydrogen content is diffused into the silicon bulk with the thinnest Al_2O_3 layer. Increasing the thickness of the Al_2O_3 layer reduces the resistivity increase due to a lower hydrogen content diffusing into the silicon bulk. Above a layer thickness of 20 nm, the resistivity increase lies within the measurement uncertainty and therefore only negligible hydrogen diffuses into the silicon bulk, clearly proving that ALD- Al_2O_3 acts as a highly effective hydrogen diffusion barrier.

Figure 5.7 shows the saturated hydrogen-boron concentrations $[\text{HB}]_{\text{sat}}$ as a function of the Al_2O_3 thickness for three different applied peak temperatures ϑ_{peak} during RTA. Without an Al_2O_3 interlayer, we measure total hydrogen concentrations of $0.5 \times 10^{15} \text{ cm}^{-3}$ for an RTA peak temperature of 680°C , $1.4 \times 10^{15} \text{ cm}^{-3}$ for $\vartheta_{\text{peak}} = 770^\circ\text{C}$, and $2 \times 10^{15} \text{ cm}^{-3}$ for $\vartheta_{\text{peak}} = 800^\circ\text{C}$. Inserting only a 5 nm thin ALD- Al_2O_3 interlayer already drastically reduces $[\text{HB}]_{\text{sat}}$ by a factor of five at $\vartheta_{\text{peak}} = 680^\circ\text{C}$. Thicker Al_2O_3 layers practically completely prevent hydrogen from diffusing through the Al_2O_3 layer at $\vartheta_{\text{peak}} = 680^\circ\text{C}$. The higher applied peak temperatures of $\vartheta_{\text{peak}} = 770^\circ\text{C}$ and 800°C require thicker Al_2O_3 layers to lead to the same degree of preventing hydrogen from diffusing into the silicon bulk. To reduce $[\text{HB}]_{\text{sat}}$ by a factor of ~ 5 at a peak temperature of 770°C , an ~ 15 nm thick Al_2O_3 layer is required, and at $\vartheta_{\text{peak}} = 800^\circ\text{C}$, an ~ 20 nm thick Al_2O_3 layer is necessary.

Without any SiN_x layer on top of the Al_2O_3 (which itself contains about 1–2 at% hydrogen [27]), a very low hydrogen content diffuses from the Al_2O_3 layer into the silicon bulk, as shown in Figure 5.7 for a sample with 20 nm Al_2O_3 fired at a peak temperature of 800 °C (red open square).

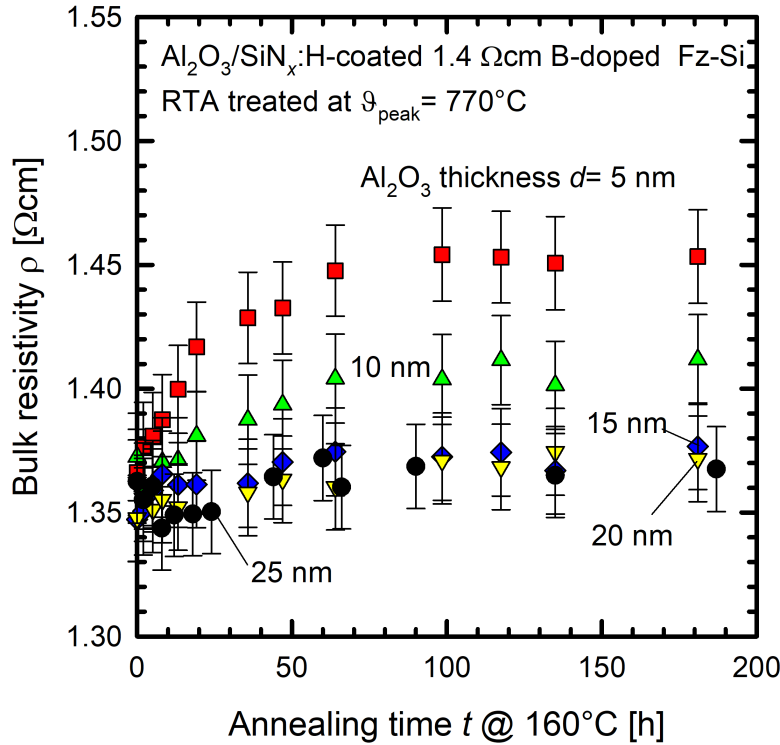


Figure 5.6: Evolution of the bulk resistivity ρ of $\text{Al}_2\text{O}_3/\text{SiN}_x\text{:H}$ -coated 1.4 Ωcm boron-doped float-zone silicon (Fz-Si) samples with different Al_2O_3 thicknesses d between 5 and 25 nm as a function of the annealing time at 160 °C in the dark after rapid thermal annealing (RTA). The composition of the SiN_x layers (refractive index $n=2.3$) and the RTA peak temperature ($\vartheta_{\text{peak}} = 770^\circ\text{C}$) are the same for all samples. The sample with 5 nm thick Al_2O_3 layer shows the highest resistivity increase and hence the highest hydrogen content in the silicon bulk. With increasing Al_2O_3 thickness, the hydrogen content in the silicon bulk shows a pronounced decrease.

Fitting exponential decay curves (lines in Figure 5.7) to the measured data, the effective diffusion length L of hydrogen in Al_2O_3 is determined for each applied temperature ϑ_{peak} . At the higher RTA peak temperatures about 800 and 770 °C, the in-diffused hydrogen content as a function of Al_2O_3 thickness saturates at a non-zero hydrogen concentration, because the Al_2O_3 layer provides some hydrogen itself. We measured an in-diffused hydrogen content for a sample coated only with 20 nm of Al_2O_3 (data point “only Al_2O_3 ”) treated at an RTA peak temperature of ~800 °C. The 680 °C RTA peak temperature is too low for the hydrogen in-diffusion from the Al_2O_3 into the silicon bulk, leading to a hydrogen content below the detection limit of our method. Therefore, the exponential decay fit for the inverted triangles saturates for $\text{Al}_2\text{O}_3 > 10$ nm at zero. At the highest applied ϑ_{peak} of 800 °C, the effective diffusion length of hydrogen in Al_2O_3 amounts to (9.3 ± 0.3) nm. The hydrogen diffusion length is reduced to $L = (7.6 \pm 0.4)$ nm by reducing ϑ_{peak} by only 30 °C and the lowest ϑ_{peak} of 680 °C leads to a diffusion length of only (2.4 ± 0.1) nm, demonstrating that already

5.5 Impact of aluminum oxide thickness on hydrogen in-diffusion

ultrathin Al_2O_3 layers of only a few nm can be applied as a highly effective hydrogen diffusion barrier.

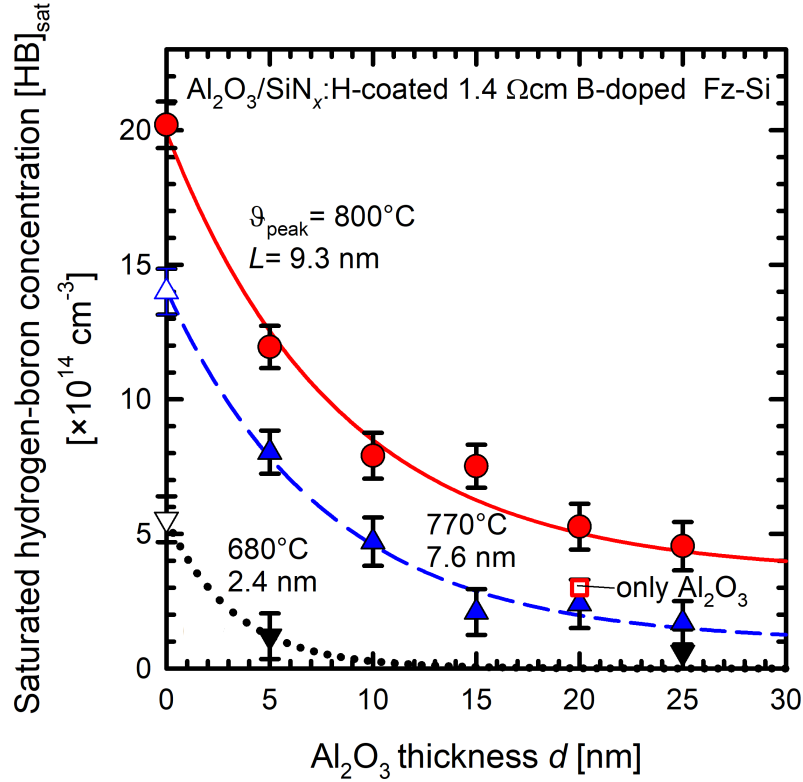


Figure 5.7: Saturated hydrogen-boron concentration $[\text{HB}]_{\text{sat}}$ of $\text{Al}_2\text{O}_3/\text{SiN}_x$ ($n=2.3$) coated $1.4\ \Omega\text{cm}$ boron-doped float-zone silicon (Fz-Si) samples after rapid thermal annealing (RTA) treatment as a function of Al_2O_3 thickness for three different peak temperatures ϑ_{peak} (uncertainty of measured peak temperatures is $\pm 10^\circ\text{C}$). The solid lines are exponential decay fits to extract the diffusion length L of hydrogen in Al_2O_3 . The open triangles are taken from Figure 5.3 and the open square is measured on a wafer coated only by $20\ \text{nm}$ of Al_2O_3 and omitting the $\text{SiN}_x\text{:H}$.

The effective diffusion length describes the average distance that the hydrogen diffuses through the aluminum oxide during firing step, which takes place under non-equilibrium conditions. The effective diffusion length L is proportional to the square root of the effective diffusion coefficient D [102], which itself can be described by an Arrhenius equation:

$$D = D_0 \exp(-E_A/kT) \quad , \quad (5.2)$$

with D_0 being the pre-exponential factor, E_A being the activation energy and k is the Boltzmann constant. Please note that D is not equal to the equilibrium diffusion coefficient of hydrogen in Al_2O_3 , since our RTA step is taking place under non-equilibrium conditions. With $L \propto \sqrt{D}$, the effective diffusion length correlates with the activation energy E_A by

$$L^2 \propto \exp(-\frac{E_A}{kT}) \leftrightarrow 2 \ln(L) \propto -\frac{E_A}{k} \times \frac{1}{T} \quad . \quad (5.3)$$

The higher the diffusion length, the higher the diffusion coefficient of the hydrogen through aluminum oxide. If Equ. (5.3) is plotted (see Fig. 5.8), the activation energy E_A for the diffusion of hydrogen through aluminum oxide in c-Si, which is a non-equilibrium process, can be determined with a value of (2.04 ± 0.2) eV.

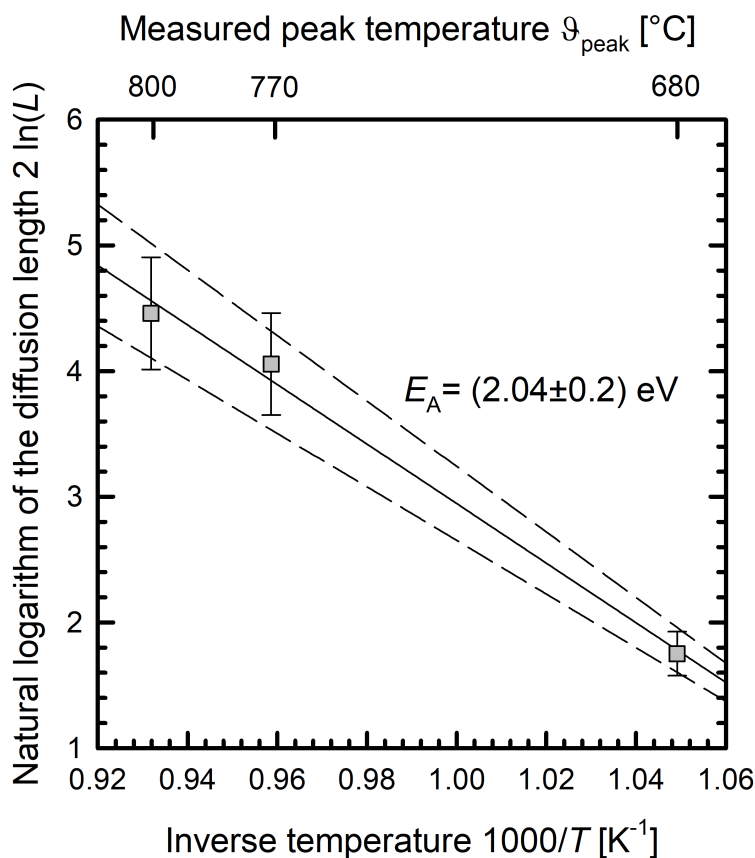


Figure 5.8: The diffusion length is proportional to the square root of the diffusion coefficient. Therefore, the activation energy E_A of hydrogen diffusion through aluminum oxide in c-Si can be determined by linear fit over the Arrhenius relation (solid lines; dashed lines indicate the uncertainties).

The experimental results, obtained in this thesis, have for the first time unambiguously shown that Al_2O_3 is a highly effective diffusion barrier and can as such be applied in the industrial Si solar cell production. It has recently been shown that introduction of hydrogen into the silicon bulk during the contact firing step can lead to a severe light and elevated temperature-induced degradation (LeTID) effects of silicon solar cells [3, 103]. The results presented in this thesis can therefore be applied to avoid hydrogen in-diffusion by implementing Al_2O_3 layers optimized as hydrogen barriers.

5.6 Impact of firing temperature on the effective lifetime

On the one hand, we intend to achieve the highest possible detectable variation of the hydrogen concentration in the silicon bulk to investigate the impact of the in-diffused hydrogen concentration on the boron-oxygen-related lifetime degradation

5.7 Impact of silicon material on hydrogen in-diffusion

and regeneration kinetics of Czochralski-silicon samples. On the other hand, the firing temperature must not be too high to the disadvantage of the overall lifetime level. Hence, we fired $\text{Al}_2\text{O}_3/\text{SiN}_x\text{:H}$ -coated $1.1\ \Omega\text{cm}$ boron-doped Cz-Si samples at different measured peak temperatures ϑ_{peak} at a belt speed of $6.8\ \text{m}\ \text{min}^{-1}$ and measured their effective lifetimes directly after the process (see Figure 5.9(a)).

Due to decreasing surface passivation quality, the measured lifetime is decreasing with increasing measured peak temperature. At a measured peak temperature of $\vartheta_{\text{peak}} = 615^\circ\text{C}$, the measured lifetime is with $730\ \mu\text{s}$, which is sufficiently large enough to perform degradation and regeneration experiments. However, the hydrogen diffusion barrier function of the Al_2O_3 layer is too effective. After firing at a measured peak temperature of 699°C , only the in-diffused hydrogen concentration through a $5\ \text{nm}$ thick Al_2O_3 layer is high enough to be detected by our resistivity change method (see Figure 5.7) and no function of dependence can be investigated with only one known hydrogen concentration in the silicon bulk. Measured firing peak temperature of 773°C and 791°C are the potentially most interesting firing temperatures with detectable different hydrogen concentrations according to Figure 5.7. However, the measured lifetimes are at first view almost too low for degradation and regeneration experiments. However, dark-annealing at 200°C and illumination at room temperature with an illumination intensity about 0.1 suns of RTA-treated Cz-Si lifetime samples at 773°C showed that the lifetime is in fact large enough to observe the boron-oxygen related lifetime degradation and regeneration (see Figure 5.9(b)) as a function of the saturated hydrogen-boron concentration (upper x-axis), which can be identified with the total hydrogen concentration. The in-diffused hydrogen concentration seems not to have an influence on the absolute value of the measured lifetimes.

Due to the identified optimal measured peak firing temperature of 773°C to achieve sufficiently high effective lifetimes with known hydrogen concentrations in the silicon bulk, we are now able to examine the BO-related lifetime degradation and regeneration kinetics as a function of detectable hydrogen concentrations in the silicon bulk. However, up to now, we have only examined the H concentration of Fz-Si material and we have hence to demonstrate that our new methodology works also on actual Cz-Si.

5.7 Impact of silicon material on hydrogen in-diffusion

After firing at a measured peak temperature of $(765 \pm 10)^\circ\text{C}$, we determine the hydrogen concentrations introduced into Fz- and Cz-Si samples. The measured temperature profiles on identically processed sister samples show comparable cooling rates (see Table 5.1) in the potentially relevant temperature range between 575°C and 625°C [62].

Figures 5.10(a) and (b) show exemplary resistivity measurements for two different Al_2O_3 thicknesses in an $\text{Al}_2\text{O}_3/\text{SiN}_x\text{:H}$ stack for Fz-Si and Cz-Si samples, which were fired at the same measured RTA peak temperature to guarantee comparability. The sample with $5\ \text{nm}$ thick Al_2O_3 saturates at the highest resistivity and with increasing Al_2O_3 thickness the saturation value decreases, as already demonstrated in Section 5.5.

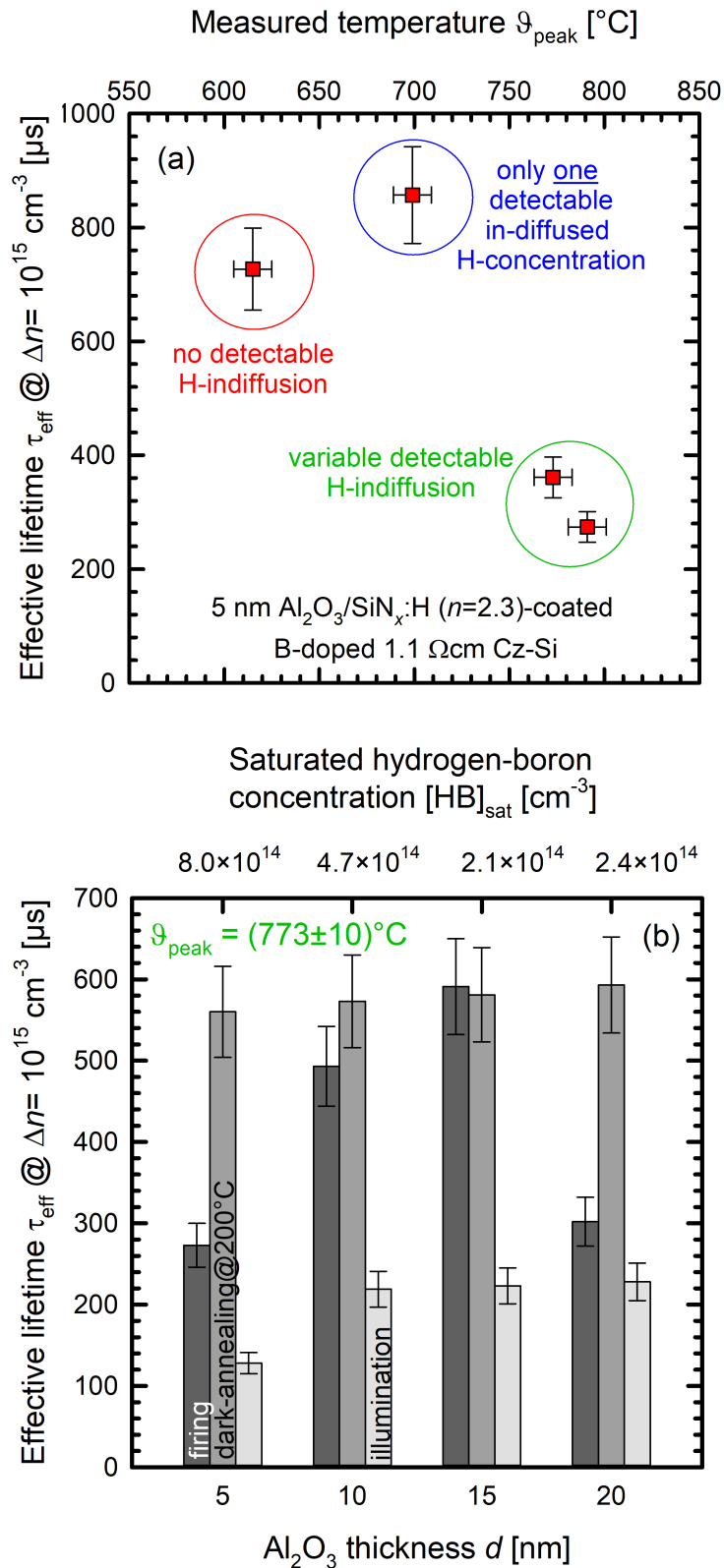


Figure 5.9: Lifetime measurements on Al₂O₃/SiN_x:H-coated 1.1 Ωcm boron-doped Cz-Si samples at a fixed injection density of $\Delta n = 1 \times 10^{15} \text{ cm}^{-3}$. The SiN_x layers have a refractive index n about 2.3. (a) Measured lifetimes after firing versus the measured peak temperature ϑ_{peak} . The Al₂O₃ layers are 5 nm thick. (b) Measured lifetimes after RTA-treatment at a measured peak temperature ϑ_{peak} of $(773 \pm 10)^\circ\text{C}$ with a belt speed of 6.8 mm min^{-1} and subsequent dark-annealing at 200°C on a hot-plate as well as subsequent illumination at room temperature versus the Al₂O₃ thickness d (lower x-axis) and the saturated hydrogen-boron concentration $[\text{HB}]_{\text{sat}}$ (upper x-axis).

5.7 Impact of silicon material on hydrogen in-diffusion

Table 5.1: Measured cooling rates of fired Cz-Si lifetime samples with different Al_2O_3 thicknesses in $\text{Al}_2\text{O}_3/\text{SiN}_x$ stacks or with only- Al_2O_3 layers in a temperature range between 575°C and 625°C .

	w $\text{SiN}_x\text{:H}$ capping layer					w/o $\text{SiN}_x\text{:H}$
Al_2O_3 thickness [nm]	5	8	10	12	15	10
Cooling rate [$^\circ\text{C}/\text{s}$]	59^{+2}_{-1}	66^{+1}_{-1}	60^{+2}_{-2}	61^{+4}_{-3}	$59^{+1.0}_{-0.1}$	63^{+3}_{-4}

Importantly, we observe an increase in the base resistivity for both examined materials, Fz-Si and Cz-Si, upon dark annealing. Figures 5.10(c) and (d) show the saturated hydrogen-boron concentrations $[\text{HB}]_{\text{sat}}$ for both materials as a function of the Al_2O_3 thickness d . The open symbols correspond to samples without SiN_x capping layer.

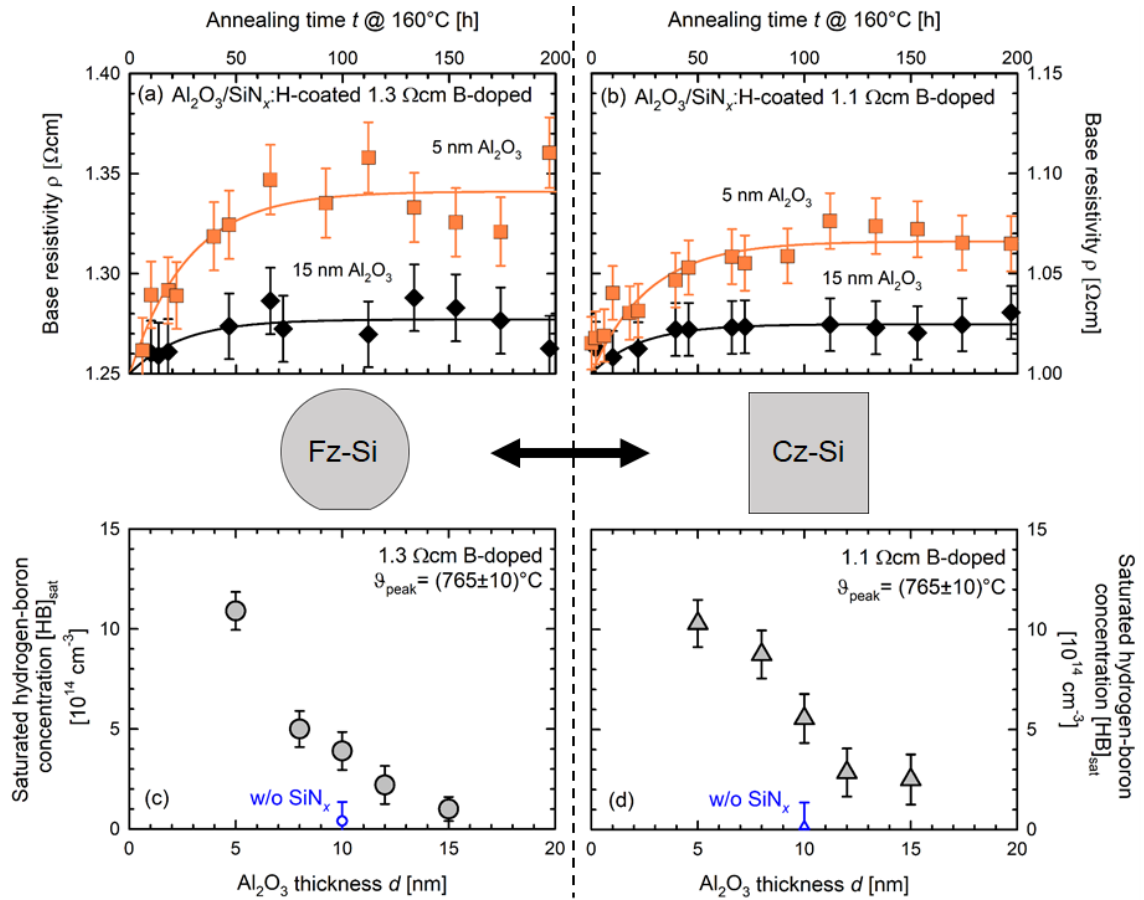


Figure 5.10: Determination of the saturated hydrogen-boron concentration $[\text{HB}]_{\text{sat}}$ by resistivity change measurements. Evolution of the bulk resistivity ρ of $\text{Al}_2\text{O}_3/\text{SiN}_x\text{:H}$ -coated (a) $1.3\ \Omega\text{cm}$ boron-doped Fz-Si samples and (b) $1.1\ \Omega\text{cm}$ Cz-Si samples with two different Al_2O_3 thicknesses d as a function of the dark-annealing time at 160°C after firing. The measured peak-temperature is $\vartheta_{\text{peak}} = (765 \pm 10)^\circ\text{C}$ and the composition of the SiN_x layers (refractive index $n = 2.3$) is the same for all samples. The sample with 5 nm thick Al_2O_3 layer shows the highest resistivity change and hence the highest hydrogen content in the silicon bulk as shown in (c) and (d), where the saturated hydrogen-boron concentration $[\text{HB}]_{\text{sat}}$ is plotted versus the Al_2O_3 thickness for (c) Fz-Si and (d) Cz-Si samples. The samples without any silicon nitride layer (opened symbols) show the lowest hydrogen content in the silicon bulk.

Comparing the saturation values in both materials, we find identical concentrations within the uncertainty margins. This result demonstrates for the first time that the HB formation is the same in defect-lean Fz-Si as in Cz-Si, known to contain significantly higher defect concentration, e.g. oxygen-related ones. Note that in previous studies [70, 104] the hydrogen concentration was only determined in Fz-Si wafers. Our new results now clearly prove that the resistivity change method is also suitable to detect hydrogen directly in the relevant Cz-Si material. The lowest hydrogen concentration according to Figures 5.10(c) and (d) is below 10^{14} cm^{-3} and is obtained for the 10 nm Al_2O_3 single layer (open symbol) without SiN_x capping. The highest hydrogen content in this section of $\sim 10^{15} \text{ cm}^{-3}$, is obtained for the stack consisting of 5 nm Al_2O_3 and 133 nm $\text{SiN}_x\text{:H}$.

Because we are now capable of determining the in-diffused hydrogen concentration into the silicon bulk of actual Cz-Si lifetime samples, we are for the first time able to directly examine the BO-related lifetime degradation and regeneration as a function of the in-diffused hydrogen concentration in the same material.

5.8 Impact of hydrogen on the boron-oxygen-related lifetime degradation

After firing, lifetime samples are first illuminated at room temperature at an illumination intensity I_{ill} of 0.1 suns. The lifetime of p -type Fz-Si samples (see Figure 5.11(a)) is fully stable over the entire period of illumination at room temperature, which indicates that the surface passivation is stable under degradation conditions. Figure 5.11(b) shows the degradation behaviour of Cz-Si lifetime samples (two per Al_2O_3 thickness) with different hydrogen contents in the silicon bulk, as shown in the previous Section, under illumination at $I_{\text{ill}} = 0.1$ suns near room temperature (temperature range $(25 \pm 5)^\circ\text{C}$). Please note that because the lifetime samples are annealed in darkness at 200°C for 10 minutes before degradation, only a small fraction of hydrogen-boron pairs is present during degradation. The lifetime samples with the 5 nm Al_2O_3 interlayer and a SiN_x capping layer correspond to the highest hydrogen concentration in the bulk ($[\text{HB}]_{\text{sat}} = 10.3 \times 10^{14} \text{ cm}^{-3}$) and the lifetime samples with only 10 nm Al_2O_3 without SiN_x capping layer correspond to the lowest hydrogen concentration ($[\text{HB}]_{\text{sat}} = 0.2 \times 10^{14} \text{ cm}^{-3}$) in these experiments.

From the measured lifetimes $\tau(t)$ and the lifetime τ_0 measured directly after annealing in darkness at 200°C for 10 min, the effective defect concentration is calculated: $N_t^* = 1/\tau(t) - \tau_0$. The data can be well fitted by an exponential rise-to-maximum function $N_t^*(t) = c + N_{t,\text{max}}^*[a - \exp(-R_{\text{deg}} \times t)]$ to the measured $N_t^*(t)$ data. From the fits we obtain the degradation rate constant R_{deg} as well as the maximum effective defect concentration $N_{t,\text{max}}^*$ and plot them versus the saturated hydrogen-boron concentration $[\text{HB}]_{\text{sat}}$.

As can be seen from Figures 5.12(a) and (b), no dependence of R_{deg} and $N_{t,\text{max}}^*$ on the bulk hydrogen content is observed, proving that hydrogen has no impact on the BO degradation kinetics.

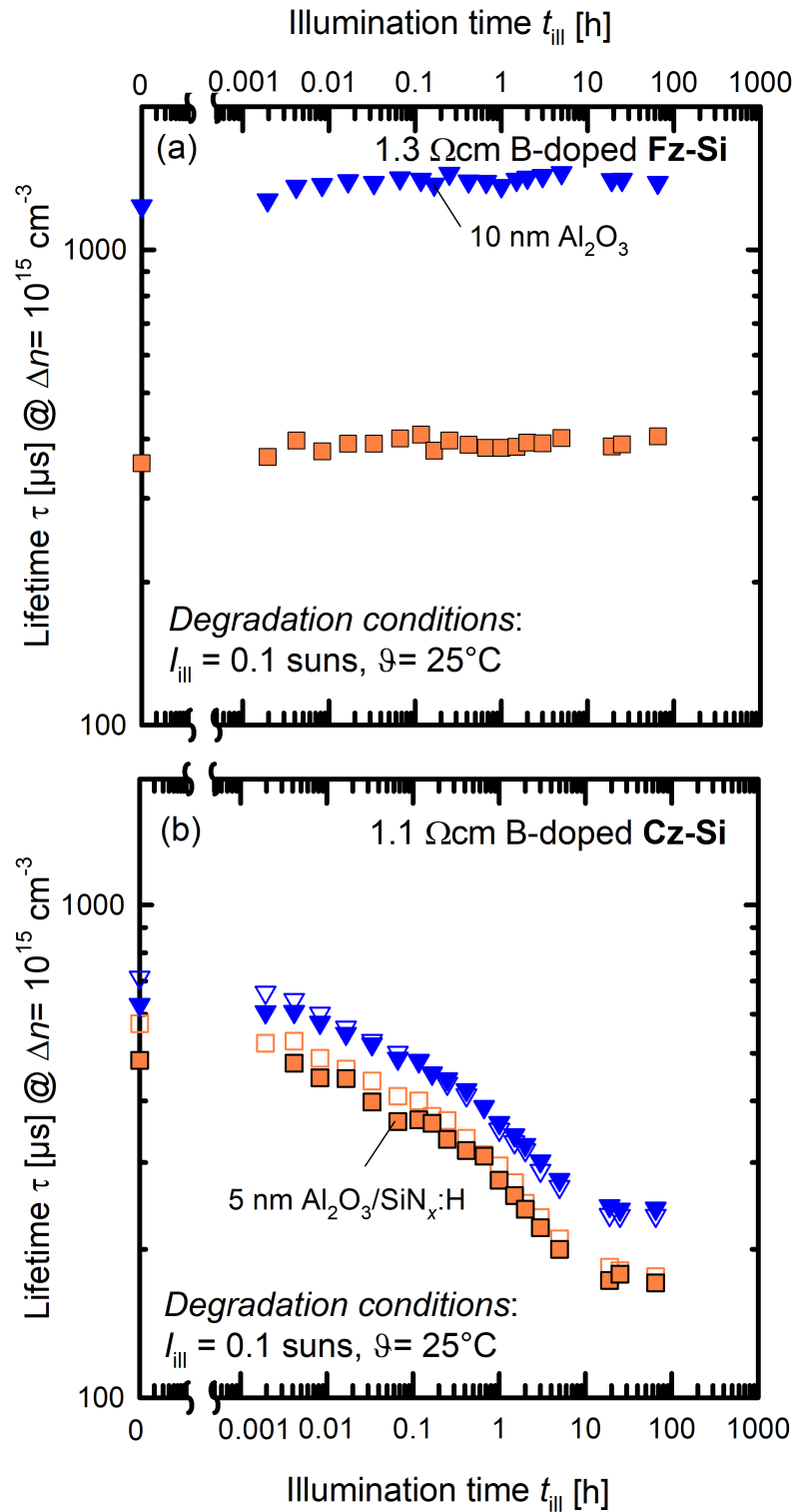


Figure 5.11: Degradation behaviour under illumination with an illumination intensity I_{ill} of 0.1 suns at room temperature. (a) Evolution of the lifetime at an excess carrier density of $\Delta n = 10^{15} \text{ cm}^{-3}$ for *p*-type Fz-Si reference lifetime samples. (b) Evolution of the lifetime at $\Delta n = 10^{15} \text{ cm}^{-3}$ for Cz-Si lifetime samples with different hydrogen concentrations (10 nm Al_2O_3 =lowest hydrogen concentration, 5 nm $\text{Al}_2\text{O}_3/\text{SiN}_x\text{:H}$ = highest hydrogen concentration in these experiments) in the silicon bulk. Two samples (filled and opened symbols) per hydrogen concentration are shown. Comparable degradation curves are obtained for the other Cz-Si samples.

The extracted R_{deg} values are $(1.11 \pm 0.15) \times 10^{-4} \text{ s}^{-1}$ for our fast-fired samples. In the literature, for boron-doped Cz-Si wafers of comparable doping concentrations, R_{deg} values of around $\approx 1 \times 10^{-4} \text{ s}^{-1}$ have been reported for non-fired non-hydrogenated lifetime samples [41]. The similarity of these rates with those measured on our hydrogenated samples is another indication that hydrogen is not involved in the BO defect activation process, in full agreement with previous defect models [2, 9].

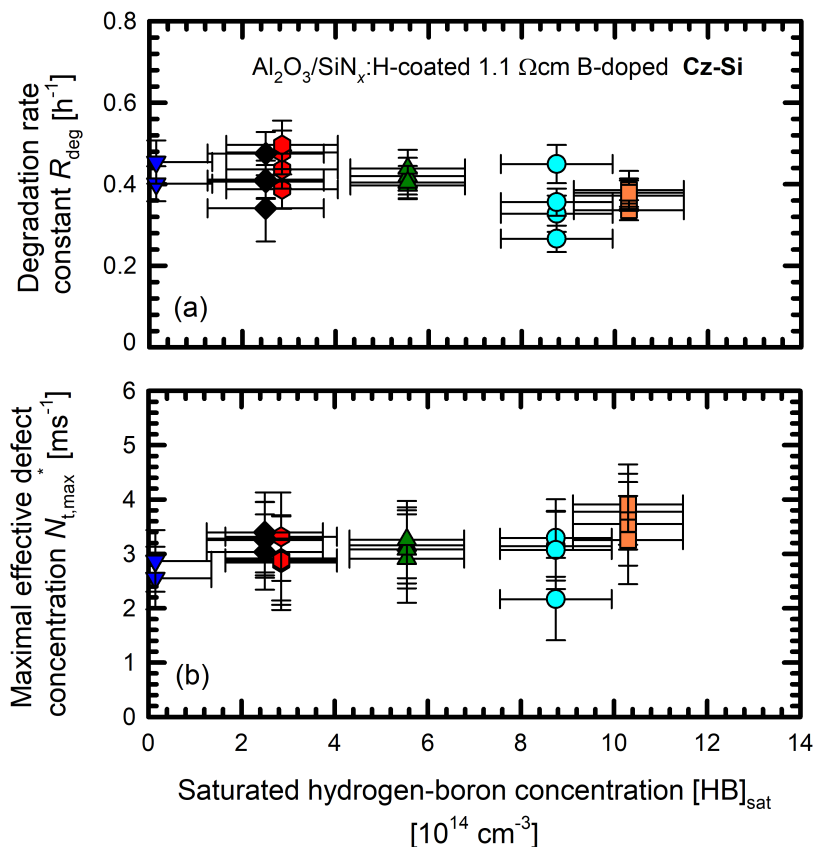


Figure 5.12: Impact of hydrogen on the BO-related lifetime degradation kinetics. (a) Degradation rate constant R_{deg} versus the hydrogen concentration in the bulk of the investigated samples. (b) Maximum effective defect concentration $N_{t,\text{max}}^*$ versus the hydrogen concentration. Each data point corresponds to a single sample.

After complete degradation, the lifetime samples are annealed in darkness at 200°C for 10 minutes and directly afterwards regenerated at 160°C and $I_{\text{ill}} = 1 \text{ suns}$ (see Figure 5.13).

5.9 Impact of hydrogen on the boron-oxygen-related lifetime regeneration

All in all the lifetime samples are annealed in darkness for 20 minutes, so only a certain fraction of hydrogen-boron pairs is present during regeneration, which we can hardly detect by our resistivity change method [70]. Over the entire regeneration process, the lifetime of the p -type Fz-Si samples (see Figure 5.13(a)) are again fully stable over the entire regeneration process, which indicates that the surface passivation is stable during illumination at elevated temperature.

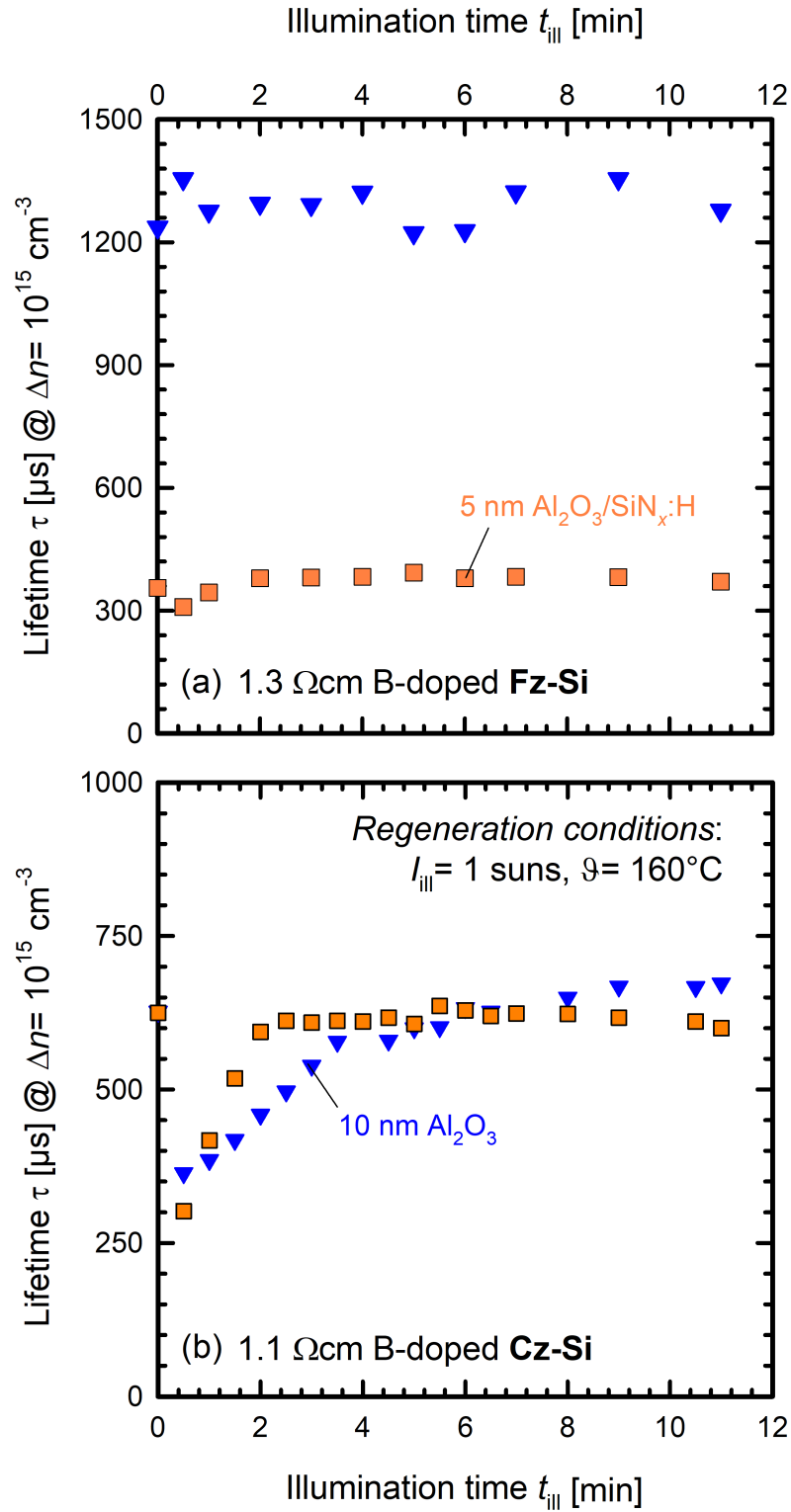


Figure 5.13: Regeneration behaviour under illumination at an illumination intensity I_{ill} of 1 suns at 160 °C. (a) Evolution of the lifetime at $\Delta n = 10^{15} \text{ cm}^{-3}$ for *p*-type Fz-Si reference lifetime samples. (b) Evolution of the lifetime at $\Delta n = 10^{15} \text{ cm}^{-3}$ for Cz-Si lifetime samples with different hydrogen concentrations (10 nm Al₂O₃ =lowest hydrogen concentration, 5 nm Al₂O₃/SiN_x:H=highest hydrogen concentration in these experiments) in the silicon bulk.

Figure 5.13(b) shows lifetime evolution curves under regeneration conditions of two

Cz-Si samples with different bulk hydrogen concentrations. We determine the regeneration rate constants R_{reg} by fitting the determined $N_t^*(t)$ evolution during regeneration by an exponential decay function $N_t^*(t) = c + N_{t,\text{max}}^*[\exp(-R_{\text{reg}} \times t)]$. Figure 5.14 shows the extracted regeneration rate constant R_{reg} as a function of $[\text{HB}]_{\text{sat}}$, i.e. the in-diffused bulk hydrogen content.

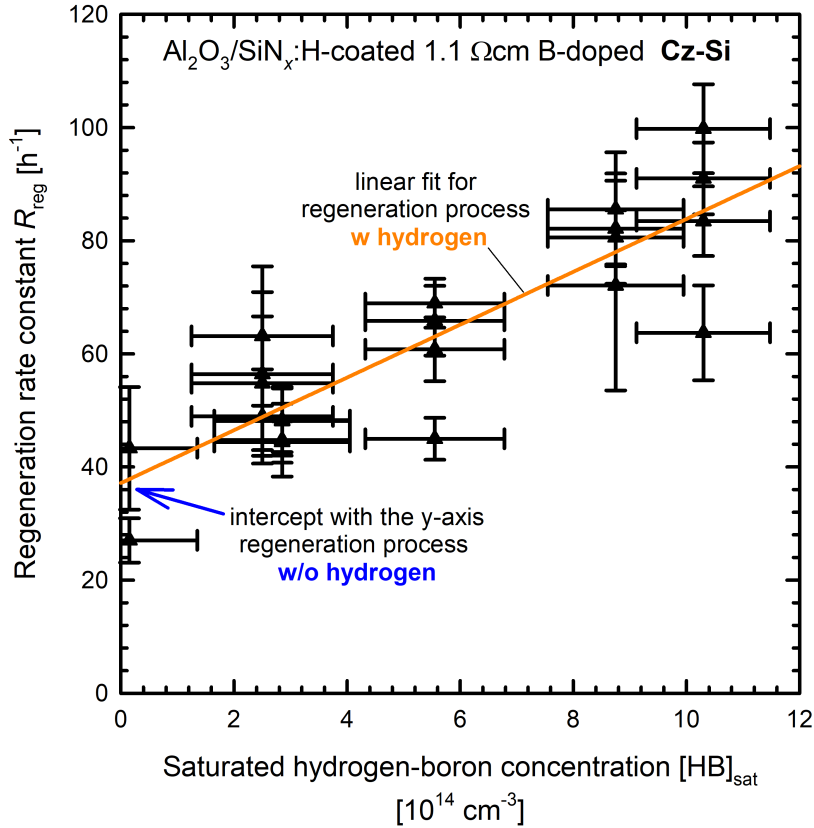


Figure 5.14: The determined regeneration rate constants R_{reg} from the $N_t^*(t)$ evolutions plotted versus the saturated hydrogen-boron concentration $[\text{HB}]_{\text{sat}}$, which is a measure for the total hydrogen concentration in the silicon bulk. Each data point corresponds to one Cz-Si sample. The straight orange line is a linear fit to the data, clearly showing a non-zero intercept with the y-axis.

Each data point is determined from a single regeneration curve of a Cz-Si lifetime sample. The regeneration rate constants can be directly compared, because the cooling rates were identical during the RTA (see Table 5.1). Despite some scatter, the regeneration rate constant increases linearly with increasing hydrogen concentration in the silicon bulk.

If we fit the dependence of R_{reg} on $[\text{HB}]_{\text{sat}}$ by a linear function, there is a non-zero intersection with the y-axis at $\sim 30 \text{ h}^{-1}$, implying that even with negligible in-diffusion of hydrogen lifetime regeneration occurs. Hence, our experiments clearly prove the beneficial effect of in-diffusing hydrogen into the silicon bulk. However, even if hardly any hydrogen is introduced into the bulk during processing, a permanent regeneration occurs under the applied regeneration conditions, i.e. hydrogen is not a necessary precondition for permanent regeneration, but accelerates the process. Please note that in order to obtain high hydrogen concentrations in the silicon bulk, in these experiments a very dense SiN_x layer ($n=2.3$) is applied in contrast to some

5.10 Chapter summary

earlier publications [55, 67, 68]. Typically, for the best surface passivation quality, $\text{SiN}_x\text{:H}$ layers with a lower refractive index ($n=2.05$) are applied which, however, introduce far less hydrogen into the silicon bulk during firing [105].

Our experimental results suggest that two different mechanisms for permanently deactivating the BO complex do exist, one with the involvement of hydrogen and one without hydrogen. This finding is in agreement with the proposed regeneration model of Voronkov and Falster [9] of the permanent BO deactivation. It is also in agreement with the result of a previous experimental study by Walter et al. [67], which intentionally avoided any introduction of hydrogen into the silicon bulk and still were able to permanently regenerate the lifetime of a Cz-Si sample.

5.10 Chapter summary

In the first part of this chapter, we have presented measurements of the total hydrogen concentration diffused into crystalline silicon from hydrogen-rich $\text{SiN}_x\text{:H}$ layers during RTA as a function of the RTA peak temperature, $\text{SiN}_x\text{:H}$ composition, and Al_2O_3 thickness in an $\text{Al}_2\text{O}_3/\text{SiN}_x\text{:H}$ stack. The total hydrogen concentration diffused into the silicon bulk was found to show a maximum as a function of the RTA peak temperature ϑ_{peak} . The ϑ_{peak} position of the maximum depends on the composition of the SiN_x layer, as characterized by the refractive index n measured by ellipsometry at a wavelength of 633 nm. The largest total hydrogen concentration of $2 \times 10^{15} \text{ cm}^{-3}$ was detected for a silicon-rich SiN_x layer with a refractive index of $n=2.3$ at $\vartheta_{\text{peak}} = 800^\circ\text{C}$. Increasing the peak temperature above 800°C led to a decrease in the in-diffused hydrogen concentration due to a decrease in the atomic density of the SiN_x layer, as shown by FTIR measurements. A drastic reduction of the hydrogen in-diffusion was achieved by introducing an ALD- Al_2O_3 layer in-between the silicon-rich $\text{SiN}_x\text{:H}$ layer and the crystalline silicon surface. A 5 nm thick Al_2O_3 layer led to a reduction of the in-diffused hydrogen concentration by a factor of ~ 5 at $\vartheta_{\text{peak}} = 680^\circ\text{C}$ and even thicker Al_2O_3 layers practically completely prevented hydrogen from diffusing through the Al_2O_3 layer. Thicker Al_2O_3 layers were found to be necessary at higher RTA peak temperatures for preventing hydrogen from diffusing into the silicon bulk. For example, to reduce the in-diffused hydrogen concentration in the bulk by a factor of 4 at $\vartheta_{\text{peak}} = 800^\circ\text{C}$, a 20 nm thick Al_2O_3 layer was required. The results presented in this thesis hence prove for the first time that ultrathin Al_2O_3 layers of only a few nm are highly effective hydrogen diffusion barriers during contact firing processes. The adaption of such diffusion barriers could prove extremely use in the production of silicon solar cells, where hydrogen in-diffusion into the silicon bulk has recently been identified as one major reason for detrimental light-induced degradation effects [3, 103, 106].

In the second part of this chapter, resistivity measurements on Czochralski-silicon (Cz-Si) and Float-zone silicon (Fz-Si) samples were applied to verify that the hydrogen-boron pair formation is the same in defect-lean Fz-Si as in Cz-Si, known to contain significantly higher defect concentration, e.g. oxygen-related ones. Thereby, we were able to quantify the BO-related lifetime degradation and regeneration as a function of the in-diffused hydrogen concentration for the first time. Cz-Si lifetime sam-

ples were coated with Al_2O_3 layers, acting as effective hydrogen barriers, of varying thickness and silicon-rich $\text{SiN}_x\text{:H}$ capping layers, acting as hydrogen sources. Rapid thermal annealing in a conveyor-belt furnace was used to hydrogenate the samples. By varying the Al_2O_3 thickness, different hydrogen concentrations were realized. On one type of sample, the $\text{SiN}_x\text{:H}$ capping layer was omitted, leading to a minimum hydrogen bulk content. Under degradation conditions ($I_{\text{ill}} = 0.1$ suns, room temperature), all samples showed comparable degradation curves. We have extracted the degradation rate constants R_{deg} for the various introduced hydrogen concentrations by fitting the time evolution of the effective defect concentration $N_t^*(t)$. The values for R_{deg} and the maximum effective defect concentration $N_{t,\text{max}}^*$ are independent of the hydrogen content, implying that hydrogen has no direct impact on BO-related lifetime degradation process. On the other hand, our measurements showed that the regeneration rate constant R_{reg} increases linearly with increasing bulk hydrogen concentration. Extrapolation to zero hydrogen content, however, did still result in a finite R_{reg} of $\sim 30 \text{ h}^{-1}$, suggesting that two different regeneration mechanisms exist: one with hydrogen involvement and one without. These results agree with a previous defect model of the permanent BO deactivation [9]. Our experimental results have hence for the first time quantified the impact of hydrogen on the BO activation and permanent deactivation.

6 Carrier lifetime stability of boron-doped Cz-Si materials for years after regeneration in an industrial belt furnace

We examine the long-term stability of the carrier lifetime in boron-doped Czochralski-grown silicon materials with different boron and oxygen concentrations, which were regenerated in an industrial belt furnace. After firing and subsequent regeneration in an industrial conveyor-belt furnace, the silicon samples are exposed to long-term illumination at an intensity of 0.1 suns and a sample temperature of about 30°C for more than two years. After regeneration, we observe a minor re-degradation (30-71% reduced compared to the degradation observed without regeneration step). We attribute this re-degradation to a non-completed regeneration within the belt furnace due to the short regeneration period. Our results show that the industrial process consisting of firing with subsequent regeneration in the same unit is very effective for industrially relevant silicon materials. Typical industrial silicon wafers with a resistivity of $(1.75 \pm 0.03) \Omega\text{cm}$ and an interstitial oxygen concentration of $(6.9 \pm 0.3) \times 10^{17} \text{cm}^{-3}$ show lifetimes larger than 2 ms after regeneration and two years of light exposure.

6.1 Introduction

In boron-doped Czochralski-grown silicon (Cz-Si), the carrier lifetime degrades severely under illumination near room temperature due to the activation of a boron-oxygen (BO) defect center [1–3], as already mentioned above. A brief anneal in the dark at increased temperatures (e.g. 200°C) was found to deactivate the BO center [1], however, this deactivation is not permanent and illumination at room temperature leads again to the full activation of the BO defect. If the samples are, however, illuminated during annealing, it was found that the BO defect can be permanently deactivated [4]. This permanent BO deactivation process, which is accompanied by a permanent regeneration of the carrier lifetime, is triggered by the presence of excess carriers and not by photons. Hence, the regeneration process was found to depend critically on the illumination intensity [57]. In addition, it depends on the detailed thermal pre-treatment [62] of the sample. By the permanent deactivation of the BO defect, the efficiency of solar cells based on *p*-type boron-doped Cz-Si can be improved by up to 3% absolute [5, 6].

Until now, only the lifetime stability after lab-type regeneration treatment on a hotplate and with a halogen lamp was investigated of fast-fired lifetime samples [107, 108]. The longest illumination duration was about 10,000 h (~1 year) [108].

Sperber et al. [108] investigated 2.0 Ωcm Cz-Si lifetime samples with different applied surface passivation and diffusion processes with the focus on surface-related degradation at 60 °C with an illumination intensity of 0.1 suns or at 80 °C with an illumination intensity of 1 sun after regeneration. Walter et al. [107] investigated 1.0 Ωcm $\text{Al}_2\text{O}_3/\text{SiN}_x$ -passivated Cz-Si lifetime samples after regeneration over 1000 hours with the focus on bulk-related degradation due to the boron-oxygen-related defect center. Walter et al. [107] could show a weak impact of the regeneration temperature ϑ_{reg} on the lifetime stability after regeneration. The re-degradation increases slightly with increasing ϑ_{reg} . Additionally, they observed no dependence of the lifetime stability after regeneration on the belt speed during firing prior to regeneration.

In this chapter, commercially available boron-doped, *p*-type Cz-Si wafers from different manufacturers with different boron and oxygen concentrations are regenerated in a combined industrial fast-firing and regeneration belt furnace in less than 70 s [109], which is of high economical relevance and is implemented into industrial solar cell production lines. The industrial belt furnace was already beneficially used for solar cells [110]. In the following, it is used to examine the long-term stability of the carrier lifetime of Cz-Si lifetime samples over more than 2 years of illumination at an intensity of 0.1 suns at a sample temperature of about 30 °C with regard to the stability of surface passivation and occurring degradation processes after industrial BO deactivation. Our experiments clearly demonstrate the benefits of adding the regeneration step to lifetime samples, which underwent an industrial cell process sequence.

6.2 Experimental details

We examine four different boron-doped Cz-Si materials with different boron and oxygen concentrations (see Table 6.1) originating from various manufacturers.

Table 6.1: Resistivities ρ and interstitial oxygen (O_i) concentrations of the investigated boron-doped Cz-Si materials of various manufacturers. The ρ values are obtained from 4-point-probe measurements and the O_i concentrations from FTIR measurements.

Material	Resistivity [Ωcm]	O_i concentration [$\times 10^{17} \text{cm}^{-3}$]	
		Center	Corner
A	1.75 ± 0.03	6.9 ± 0.3	7.1 ± 0.5
B	1.76 ± 0.02	7.7 ± 0.5	8.3 ± 0.1
C	1.08 ± 0.09	8.4 ± 0.2	6.8 ± 0.2
D-1	1.73 ± 0.02	10.5 ± 0.7	9.6 ± 0.3

As a reference, also boron-doped Fz-Si material is included in the experiment. Whereas materials A and B in Table 6.1 are typical present-day industrial Cz-Si materials with homogeneously distributed oxygen concentrations over the wafer (center and corner), material C is a standard Cz-Si material from the early 2000s with a relatively inhomogeneously distributed oxygen concentration. Material D is stemming from the top region of a silicon crystal (seed end). According to the manufacturer's

6.2 Experimental details

data, wafers from different heights of this seed end have the same oxygen concentration, so we investigate material D-1 representatively for the three different heights in the following. The oxygen concentrations are determined via Fourier-Transform-Infrared (FTIR) spectroscopy (see Section 2.1.3) on sister samples using a *VERTEX 70* (Bruker) FTIR spectrometer. As calibration factor $K = 3.14 \times 10^{17} \text{ cm}^{-1}$ is used within the evaluation of the measured oxygen-related absorption peaks (see Section 2.1.3). According to the measured resistivities ρ , material A, B and D-1 have a similar boron concentration about $8.3 \times 10^{15} \text{ cm}^{-3}$ and material C has a doping concentration about $1.4 \times 10^{16} \text{ cm}^{-3}$.

All wafers undergo a phosphorus diffusion step using POCl_3 in a quartz-tube furnace (830°C , 3 h). Afterwards, the resulting phosphosilicate glass layers and the n^+ -regions on both wafer surfaces are removed by hydrofluoric acid and potassium hydroxide solution. The final wafer thickness of all materials amounts to $(164 \pm 10) \mu\text{m}$ (error refers to the wafer-to-wafer scattering) to ensure comparability. Both surfaces of each wafer are passivated using $\text{Al}_2\text{O}_3/\text{SiN}_x$ stacks. The aluminum oxide Al_2O_3 (10 nm) is deposited via plasma-assisted atomic layer deposition (PA-ALD) in a FlexAL system (see Section 2.2.1) from Oxford Instruments and the silicon nitride SiN_x (70 nm) via plasma-enhanced chemical vapour deposition (PECVD) in a SiNA system (see Section 2.2.2) from Meyer Burger Technology AG. The SiN_x layer has a refractive index of $n = 2.05$ as determined by ellipsometry at a wavelength of 633 nm. An RCA cleaning sequence is applied before each process step.

The lifetime samples, Fz- and Cz-Si wafers, are then submitted to a combined firing-regeneration process in an industrial infrared conveyor-belt furnace of type *c.FIRE.REG* 9600 from centrotherm international AG [109] and fired at a belt speed of 7.2 m min^{-1} .



Figure 6.1: Photograph of the *c.FIRE.REG* furnace from Centrotherm International AG with a high-temperature zone for fast-firing (*c.FIRE*) and a low-temperature zone with an illumination unit for regeneration of the lifetime (*c.REG*) [109].

For the regeneration treatment, we choose a regeneration temperature of 232°C (measured) and an illumination intensity of 7-9 suns with a duration less than 70 s. Within regeneration experiments on a hot-plate, a regeneration rate constant R_{reg} of 144 h^{-1} was determined for a regeneration temperature of 220°C and an illumination intensity about 1 suns [111]. Thus, the regeneration process is significantly accelerated by industrial regeneration.

Additionally, lifetime samples made of the same p -type Cz-Si materials and, in

addition, Fz-Si lifetime samples are just fast-fired (FF) without the subsequent regeneration process in the industrial infrared conveyor-belt furnace DO-FF-8.600-300 from centrotherm international AG again at a belt speed of 7.2 m min^{-1} . An adapted firing profile (set-peak-temperature $\vartheta_{\text{set,peak}} = 850 \text{ }^\circ\text{C}$, measured peak-temperature $\vartheta_{\text{peak}} \approx 750 \text{ }^\circ\text{C}$) according to the temperature treatment in the *c.FIRE REG* was used. These firing conditions are chosen according to the identified optimum for lifetimes exceeding 1 ms in [111]. All in all, for the combined firing-regeneration treatment, we choose a profile as illustrated in [109], green curve, but higher measured peak-temperatures, and lifetime samples were processed equivalent to the blue curve in [109]. Firing profiles were measured by a type-K thermocouple (KMQXL-Imo50G-300, Omega) in combination with a temperature tracker (DQ1860A) from Datapaq. The cooling rate of each RTA-treatment was about $60 \text{ }^\circ\text{C/s}$ in the potentially relevant temperature range between $575 \text{ }^\circ\text{C}$ and $625 \text{ }^\circ\text{C}$ [62].

After firing, all lifetime samples are illuminated at room temperature (sample temperature $\sim 30 \text{ }^\circ\text{C}$) at an illumination intensity of $I_{\text{ill}} = 0.1 \text{ suns}$ (10 mW/cm^2 using halogen lamps). The illumination intensity is adjusted to the equivalent generated current density of the sun's spectrum using a calibrated reference silicon solar cell. In-between the periods of illumination the lifetime is measured in the center of the samples using a WCT-120 lifetime tester from Sinton Instruments [7]. If not stated otherwise, carrier lifetimes are reported at an excess carrier concentration of $\Delta n = 10^{15} \text{ cm}^{-3}$ with a relative uncertainty of 10 % [112]. Photoconductance decay (PCD) measurements are taken in the center of the lifetime samples if not mentioned otherwise. In addition, spatially resolved lifetime measurements are performed by lifetime imaging (PC-PLI) technique [11]. The lifetime samples on which the regeneration process was omitted are annealed in darkness at $200 \text{ }^\circ\text{C}$ on a hotplate for 10 min prior to light exposure (see $t_{\text{ill}} = 0 \text{ h}$ in Figure 6.2(a)) to determine the BO-related lifetime limitations. The industrially regenerated samples are illuminated for more than 2 years to examine the long-term lifetime stability after industrial regeneration.

6.3 Lifetime measurements and analysis

Figure 6.2 shows the evolution of the carrier lifetime during illumination at 0.1 suns as a function of time at room temperature for the materials A-D as well as for the reference Fz-Si material ($\rho = 1.2 \text{ } \Omega\text{cm}$). Figure 6.2(a) includes the samples that were just fired in the industrial belt furnace and Figure 6.2(b) shows the samples that were fired and subsequently regenerated in the *c.FIRE REG* furnace. Lifetime samples of materials A-C reach at least as high lifetimes (in the range of milliseconds) after firing and subsequent regeneration as directly after firing and dark-annealing. The dark-annealing step is necessary to temporarily deactivate the boron-oxygen defect. The lifetime of material D is only $450 \text{ } \mu\text{s}$ after firing and subsequent regeneration, which is significantly lower than the lifetime measured after firing and dark-annealing, which amounts to $700 \text{ } \mu\text{s}$. This finding might indicate that additional background defects are present in material D after the regeneration treatment. The lifetime of the only-fired lifetime samples of all Cz-Si materials degrades by $\sim 90\%$ (fully activated BO defect) in relation to the lifetime after 10 min of annealing at $200 \text{ }^\circ\text{C}$ in the dark (temporarily deactivated BO defect, see $t_{\text{ill}} = 0 \text{ h}$ in Figure 6.2(a)).

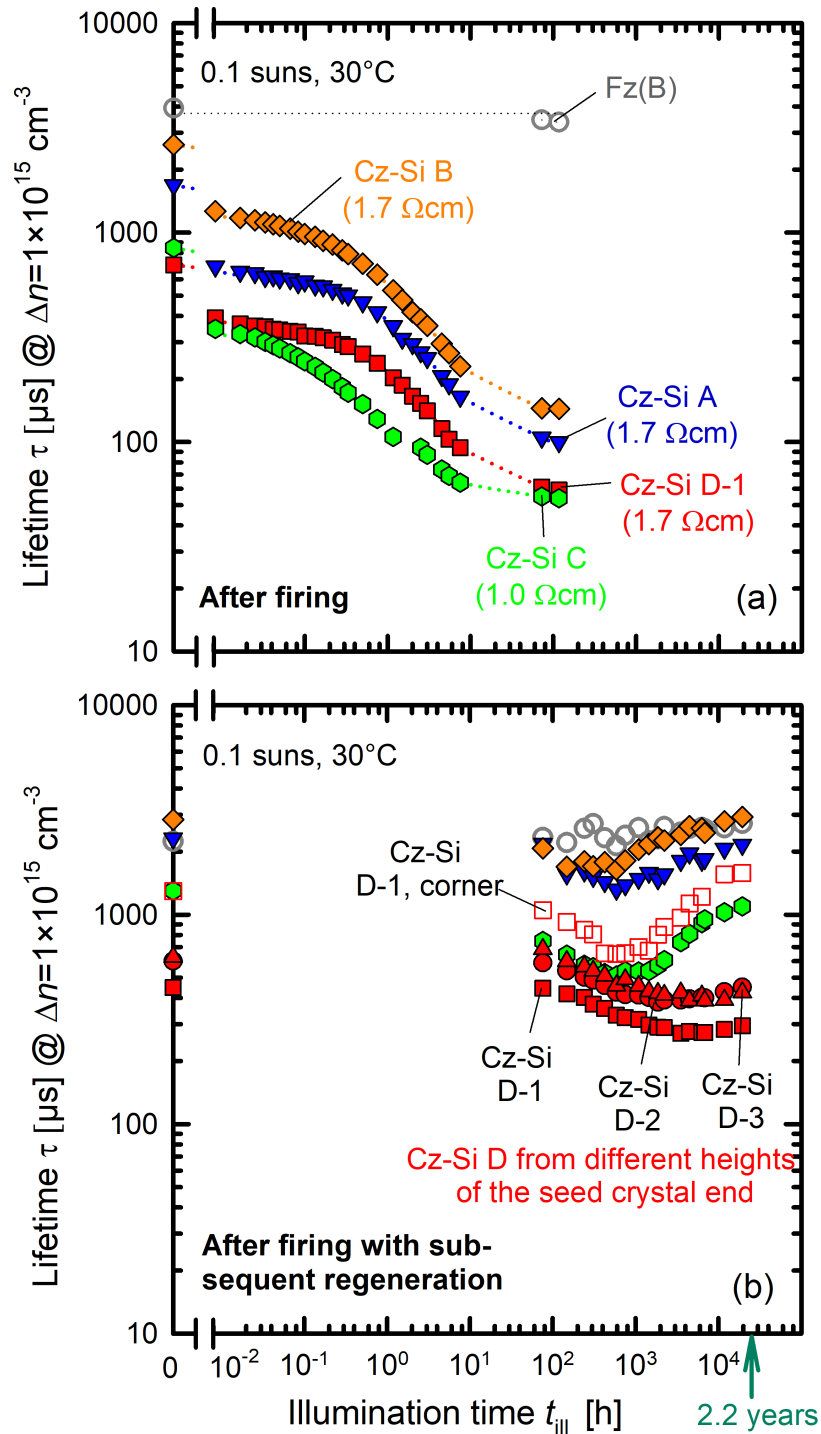


Figure 6.2: Lifetime evolution, measured in the wafers' center, of *p*-type Cz-Si materials A, B, C and D from different manufacturers (filled symbols) and an Fz reference sample (open circles) under illumination at 0.1 suns at 30°C after (a) firing in an industrial belt furnace and (b) after firing with subsequent regeneration in an industrial belt furnace. The measured lifetimes in the corner of D-1 are added as open squares.

In detail, material A degrades from 1690 μs to 100 μs , material B from 2630 μs to 150 μs , material C from 850 μs to 50 μs and material D-1 from 700 μs to 60 μs . PCD measurements of the fired and subsequently regenerated Cz-Si wafers are shown

in Figures 6.2(b). The lifetime after the permanent deactivation of the BO defect initially decreases under illumination at room temperature. Only the lifetime of the *p*-type Fz-Si reference sample is fully stable over the entire period of illumination, which indicates that the surface passivation is stable under these conditions. In addition, we calculated the time-resolved saturation current density J_0 for all samples [113]. The J_0 values (not shown here) are stable within the scattering, which supports the statement that the surface passivation quality stays stable during illumination.

The degradation extent of the *p*-type Cz-Si lifetime samples is significantly reduced after regeneration compared to the lifetime samples, which only underwent the firing step without regeneration. The subsequent industrial regeneration reduces the subsequent lifetime degradation by at least 30% (material D, center) and in the best case by 72% (material A). The samples made from material D degrade after firing with subsequent regeneration to 270 μs compared to 60 μs for the only-fired case. Samples made from material A degrade only to 1320 μs after regeneration instead of 110 μs for the only-fired case. The samples show hence a significantly improved lifetime stability by firing with a subsequent regeneration step compared to without the regeneration step.

After complete degradation of the regenerated samples, the lifetime increases again with different time constants for the different materials. The lifetimes of the materials A-C increases back to their initial lifetimes within ~ 2 years of illumination near room temperature. These materials have a lower oxygen concentration of $(7 - 8) \times 10^{17} \text{ cm}^{-3}$ than material D ($[\text{O}_i] \approx 10 \times 10^{17} \text{ cm}^{-3}$, see Table 6.1). The lifetime of material D does not regenerate in the center within the time scale of our experiment. In a previous study of material C [107], the fired samples of material C were regenerated at 200 °C on a hotplate by 1 sun illumination intensity for several minutes. Subsequent room temperature illumination resulted in a lifetime degradation with a minimum reached only after 2000 h before recovery set in. It seems that the lifetime recovery was almost twice as fast as in our samples from material C, which were regenerated in the industrial belt furnace, possibly due to the increased regeneration temperature of 230 °C in the industrial regeneration furnace.

Figure 6.3 shows PC-PLI measurements (see Section 2.1.2) of the fired and subsequently regenerated Cz-Si materials A, C and D-1 for three different times of illumination near room temperature. The left column shows lifetime images recorded directly after firing with subsequent regeneration, the middle column after 587 h of illumination and the right column after ~ 2 years of illumination. Material A and B (B not shown here, because it shows exactly the same behavior as A) degrade slightly and homogeneously over the complete wafer area. Material C degrades more severely. The corners of the wafer of material C, however, degrade slightly less, presumably due to the lower oxygen concentration compared to the center. However, after nearly two years of illumination, material C shows a homogeneous lifetime distribution again. Moreover, material D already starts with an inhomogeneous lifetime distribution with ring-like defect structures right after regeneration (see Figure 6.3, bottom row), which is frequently occurring in the seed end of Cz-Si crystals [114] due to the Czochralski growth method. The lifetime of material D decreases over the complete wafer, but only the corners reach the initial lifetime again after 2.2 years of illumination, as shown in Figure 6.2(b).

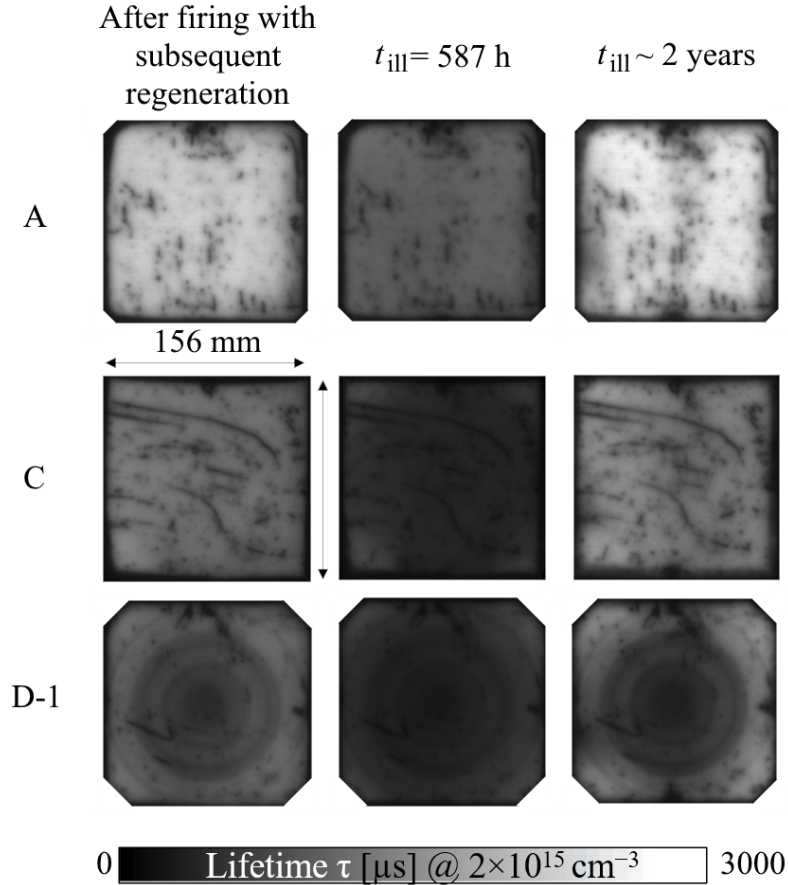


Figure 6.3: Photoconductance-calibrated photoluminescence lifetime imaging (PC-PLI) measurements of materials A, C and D-1 after firing with subsequent regeneration and different times of illumination near room temperature.

Figure 6.4 shows injection-dependent lifetimes extracted from the PC-PLI measurements at different locations on the wafers for different illumination times. Whereas for material A the injection-dependent lifetime curves at the different wafer locations are practically identical, we observe strong differences for material C. For material C the lifetime in the corner is significantly larger than the center region after 587 h of illumination. For example, at $\Delta n = 1 \times 10^{15} \text{ cm}^{-3}$ a lifetime of $920 \mu\text{s}$ is measured in the corner of the sample and a lifetime of $460 \mu\text{s}$ in the center. Only after 2.2 years of illumination the lifetime curves coincide again for material C. For material D, we observe already very different injection-dependent lifetime curves in the center and in the corner directly after regeneration. This suggests that the lifetime in these regions is limited by other recombination centers than the BO defect. After 2.2 years of illumination, the lifetime curves measured in the corners of material D-1 coincide again, whereas we observe no lifetime regeneration in the center, which is limited by other background defects. An explanation for the different regeneration behavior in the center and in the corner of material D-1 could be the different oxygen concentrations [56].

From the measured lifetimes $\tau(t)$ evolution and the lifetime measured directly after dark-annealing τ_0 , the effective defect concentration N_t^* can be determined by equation 3.1. The time evolution of N_t^* during light-induced degradation can be

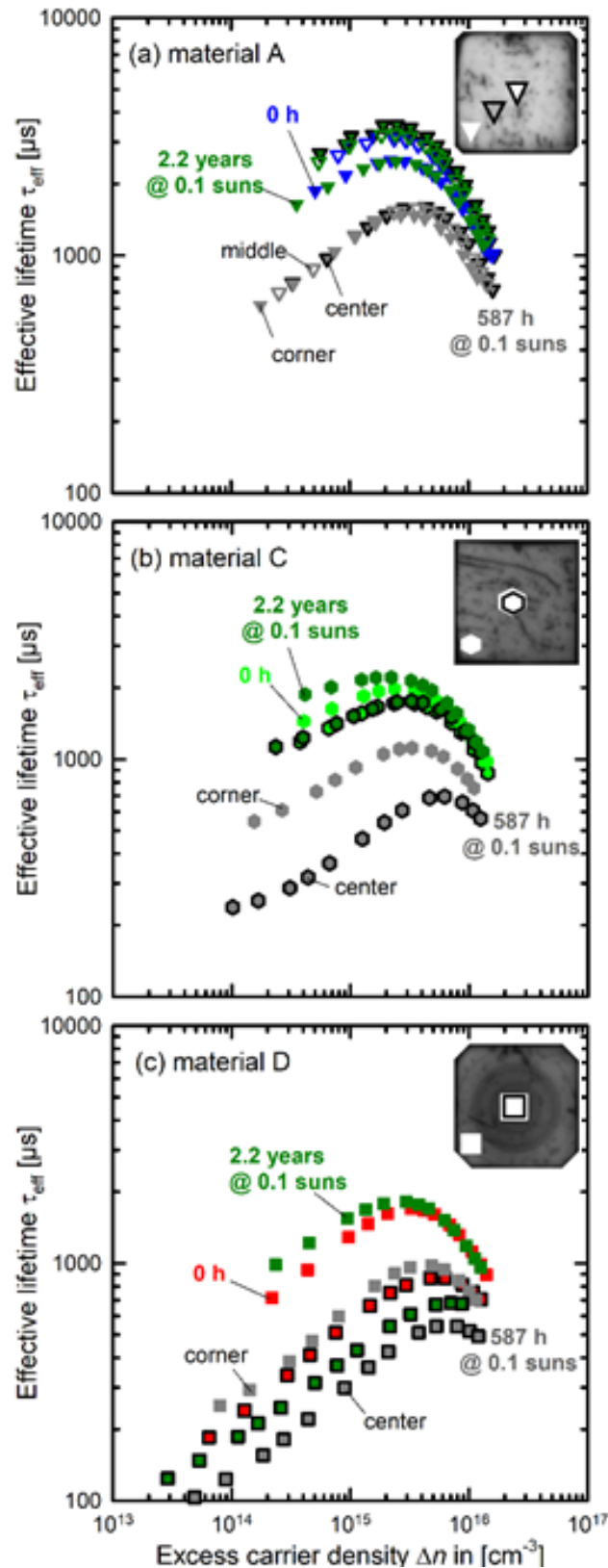


Figure 6.4: Injection-dependent lifetime measurements at different locations from PC-PLI measurements for the materials (a) A, (b) C and (c) D-1 after firing with subsequent regeneration in an industrial conveyor-belt furnace (0 h) and after 587 h as well as 2.2 years of illumination at room temperature after regeneration. Black framed symbols correspond to the center, whereas full and open symbols correspond to corner and middle position, respectively.

6.3 Lifetime measurements and analysis

described by an exponential function with a degradation rate constant R_{deg} (see Section 3.1). The determined R_{deg} values of the only-fired lifetime samples amount to $3.1 \times 10^{-5} \text{ s}^{-1}$ for materials A and D (lower doping concentration) and $1.2 \times 10^{-4} \text{ s}^{-1}$ for material C (higher doping concentration). These values are in agreement with the defect generation rate constants of the light-induced BO defect activation published in the literature [41], for unfired samples of the same doping concentrations. According to Ref. [41], the defect generation rate constant does not depend on the oxygen concentration. Obviously, the firing step has no influence on the degradation rate constants as well.

In addition, we experimentally determine the effective defect concentration from τ_{op} being the lifetime measured directly after regeneration in the industrial belt furnace and from τ_{ill} being the lifetime after long-term illumination for a period t near room temperature:

$$N_{\text{t,reg}}^*(t) = \frac{1}{\tau_{\text{ill}}(t)} - \frac{1}{\tau_{\text{op}}} \quad (6.1)$$

The time evolution of $N_{\text{t,reg}}^*$ during lifetime stability testing at room temperature and with an illumination intensity of 0.1 suns can be described by a degradation rate constant R_{deg} and a regeneration rate constant R_{reg} (see Sections 3.1 and 3.2) as already analyzed for the only-fired lifetime samples. Fired and subsequently regenerated lifetime samples made of material A and B degrade in the first 587 h of illumination with a degradation rate constant of $R_{\text{deg}} = 9.7 \times 10^{-7} \text{ s}^{-1}$, whereas lifetime samples of material C reach a minimum in lifetime after 751 h of illumination with $R_{\text{deg}} = 2.2 \times 10^{-6} \text{ s}^{-1}$. A similar degradation behavior was already reported in the literature [107] for the same material regenerated on a hot-plate. Lifetime samples of material D-1 degrade on a different time scale in the center and the corner of the wafer, but with a similar degradation rate constant. In the center the degradation takes even longer/slower (3517 h) with $R_{\text{deg}} = 3.6 \times 10^{-7} \text{ s}^{-1}$. The lifetime in the corner of material D-1 reach a minimum after 587 h of illumination with $R_{\text{deg}} = 4.4 \times 10^{-7} \text{ s}^{-1}$. All these degradation rate constants are much lower than the typical BO degradation rates (see Figure 6 in [41]) without any regeneration treatment applied. The degradation rate constants are reduced by up to two orders of magnitude due to the regeneration treatment and the materials degrade much slower in lifetime. All determined defect deactivation rates (see Section 3.2), or rather regeneration rate constants R_{reg} , of materials A-C and the corner of material D are in the same order of magnitude: $R_{\text{reg}}(\text{A}) = 5 \times 10^{-4} \text{ h}^{-1}$, $R_{\text{reg}}(\text{B}) = 7 \times 10^{-4} \text{ h}^{-1}$, $R_{\text{reg}}(\text{C}) = 3 \times 10^{-4} \text{ h}^{-1}$ and $R_{\text{reg}}(\text{D, corner}) = 3 \times 10^{-4} \text{ h}^{-1}$.

In another experiment reported recently [111], lifetime samples made of 1-2 Ωcm boron-doped Cz-Si with the same passivation layers as applied in our present study, underwent a comparable RTA treatment at $\vartheta_{\text{peak}} = 850^\circ\text{C}$ with a belt speed of about 7.2 m min^{-1} in a DO-FF-8.600-300 belt furnace. In order to investigate the impact of the regeneration temperature, different temperatures were applied on a hot-plate to regenerate the samples. The resulting Arrhenius plot of the determined regeneration rate constants for a regeneration temperature range between 80 and 220°C [111] can be extrapolated to 30°C , resulting in a range of regeneration rate constants between

0.03 to 0.0002 h^{-1} . This range fits with the regeneration rates of the present study ($0.0003 - 0.0007 \text{ h}^{-1}$), determined near room temperature (30°C) at an illumination intensity of 0.1 suns after firing with subsequent regeneration in an industrial belt furnace. However, the samples in this study are just illuminated by 0.1 suns instead of 1 suns. Therefore, the regeneration after firing with subsequent regeneration is much faster than expected.

Our experimental results suggest that the light-induced defect activation and subsequent permanent deactivation might be explained by an incomplete regeneration process and that a certain fraction of BO defects might remain after regeneration with changed activation kinetics. In order to extract further information regarding the properties of the re-activated defect in the regenerated samples, the injection-dependent lifetimes before and after degradation are analyzed in the following.

6.4 Defect analysis

The difference of the injection-dependent lifetimes before τ_0 and after degradation τ_{deg} results in the lifetime of the activated defect τ_{def} :

$$\tau_{\text{def}} = \left(\frac{1}{\tau_{\text{deg}}} - \frac{1}{\tau_0} \right)^{-1}. \quad (6.2)$$

In the case of the regenerated samples, τ_{deg} has to be replaced by the lifetime minimum under illumination after regeneration $\tau_{\text{ill,min}}$ and τ_0 by the lifetime directly measured after regeneration τ_{0p} . Plotting the normalized defect-related lifetime $\tau_{\text{def}}/\tau_{n0}$ versus the ratio of the electron-to-hole concentrations n/p can help to identify defect centers. The quantitation of recombination of charge carriers via defects in semiconductors over carrier lifetime measurements as a function of temperature and injection density is also called injection-dependent lifetime spectroscopy [115]. For a deep-level defect in *p*-type silicon the corresponding defect-related lifetime τ_{def} can be written as a linear function of n/p [116, 117]:

$$\frac{\tau_{\text{def}}}{\tau_{n0}} = 1 + Q \frac{n}{p}, \quad (6.3)$$

where the slope is $Q = \tau_{p0}/\tau_{n0}$ and τ_{n0} and τ_{p0} are the capture time constants for electrons and holes, respectively. The lifetime dependence on n/p is reduced to that expected for a one-level deep donor center [117]. The validity of a single-level approximation to the B-O defect in *p*-type silicon has been shown to give meaningful results [117]. As can be seen from Figure 6.5, we determine the electron and hole capture time constant ratio Q for the only-fired samples (filled symbols) as well as for the fired plus industrially regenerated lifetime samples (open symbols) to be in the range between 9 ± 3 and 12 ± 1 for lifetime measurements in the center of the wafers. To perform a defect analysis for the corner of material D-1, which degrades on a different time scale than the center (see Figure 6.2(b)), too few data points are available, since these lifetime measurements were only carried out by PC-PLI.

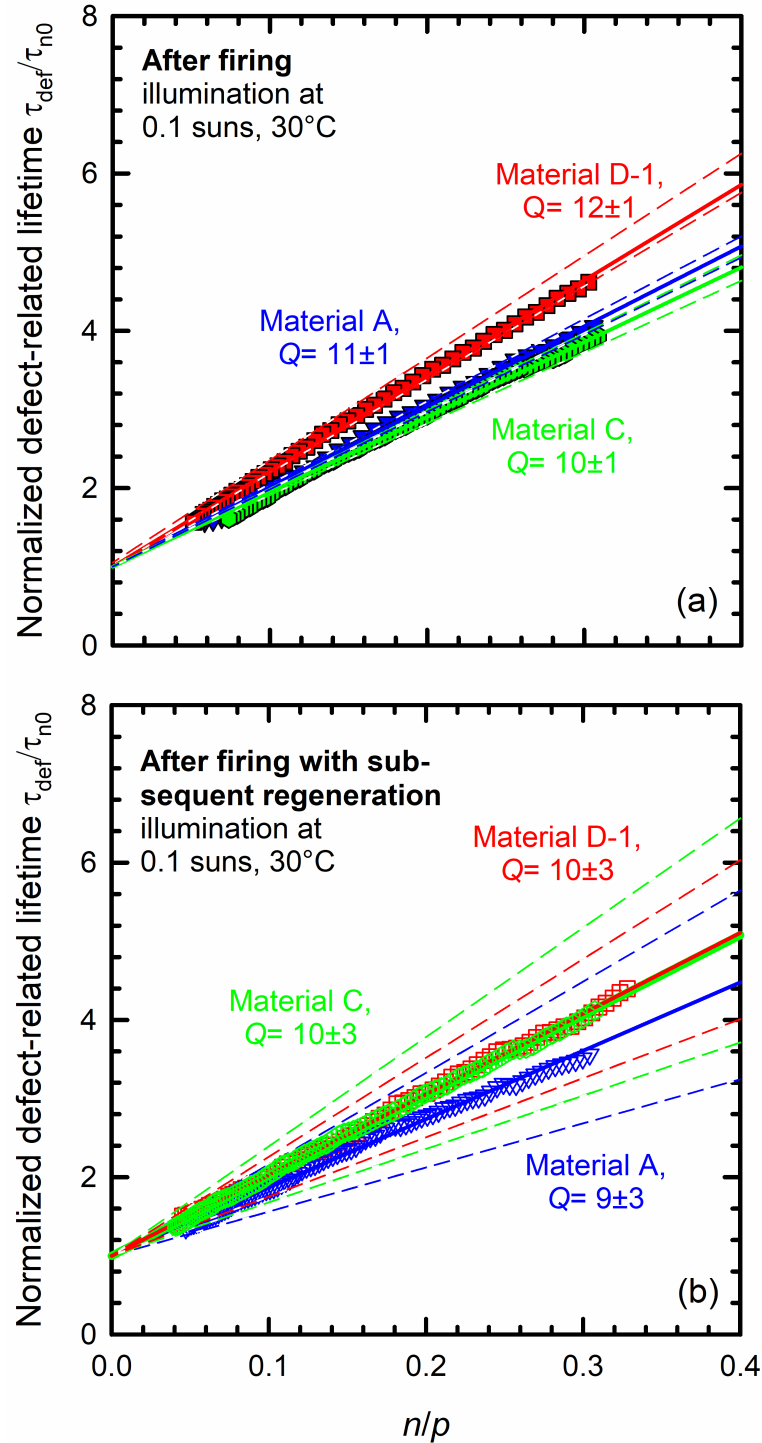


Figure 6.5: Normalized defect-related lifetime $\tau_{\text{def}}/\tau_{n0}$ of the light-induced defect for fired p -type Cz-materials A, C and D-1 as a function of the electron-to-hole concentrations n/p . The Q values were extracted from the slopes of the linear fits (solid lines; dashed lines indicate the experimental uncertainties) to the measurements for degradation under typical illumination conditions (room temperature, 0.1 suns) (a) after firing (filled symbols) and (b) after firing with subsequent industrial regeneration (open symbols). The extracted Q values do not change due to the regeneration within the measurement uncertainty.

The Q values in the range 9.5 ± 3.5 for all examined materials agree well with

literature data for the BO defect, where Q values in the range between 10 and 12 have been reported [118–120]. Typically, Q values the LeTID-specific defects are in the range between 20 and 36 [121–123] and can thus be excluded as degradation mechanism in our experiments. Our extracted Q values hence suggest that the regeneration process might not be completely finished during regeneration in the industrial belt furnace [124, 125]. However, the observed degradation kinetics slowed down significantly after regeneration. The detailed activation mechanism of the BO defect might hence have changed by the regeneration treatment [126].

6.5 Discussion

We attribute the re-degradation to a non-completed regeneration within the belt furnace due to the short regeneration period. This would imply that during the industrial regeneration process a part of the BO defects might be transformed into an in-active state, which can then lead to a re-degradation during subsequent illumination. Since the extracted degradation and regeneration rate constants after industrial regeneration do not correspond to the typical BO degradation and regeneration rate constants on non-regenerated Cz-Si wafers, the detailed defect kinetics has obviously changed significantly during the regeneration step. All in all, current defect models [3, 56, 120] are not able to explain this behavior. Hence, an extension of current BO defect models seems to be necessary.

6.6 Summary

In this chapter, we have unambiguously demonstrated the benefits of adding a regeneration step in an industrial inline regeneration tool to lifetime samples which underwent an industrial cell process sequence. The carrier lifetime evolution of state-of-the-art boron-doped Cz-Si materials as well as material stemming from the seed end of a crystal were examined at room temperature under 0.1 suns illumination intensity up to 2.2 years after regeneration. Despite very high lifetimes measured directly after regeneration, we observed a subsequent renewed light-induced degradation in all materials, although up to 72 % reduced at a much lower degradation rate (up to two orders of magnitude lower) compared to the standard BO degradation. The activated defect was found to have a capture time constant ratio Q in the range 9.5 ± 3.5 for all examined materials, which is comparable to the reported Q range for the BO defect. Hence, our results suggest that a fraction of BO was not fully removed by the fast industrial regeneration treatment. Due to the slower re-activation of the BO defect, the detailed degradation kinetics has, however, changed significantly, which is not explained by existing defect models. On the long term, we observed a second regeneration process during illumination near room temperature, which saturated after two years, except for the material stemming from the seed end, which was dominated by other background defects. This material also showed ring-like defect structures, which the other three materials did not show. The three state-of-the-art Cz-Si materials showed stable and high lifetimes above 1 ms after more than 2 years of light exposure. Typical industrial silicon wafers with a resistivity of $(1.75 \pm 0.03) \Omega\text{cm}$ and an interstitial oxygen concentration of

6.6 Summary

$(6.9 \pm 0.3) \times 10^{17} \text{cm}^{-3}$ even show lifetimes larger than 2 ms after regeneration and 2 years of light exposure.

7 Summary

In this thesis, oxygen-rich boron-doped p -type Czochralski-grown silicon (Cz-Si) was studied with the focus on the boron-oxygen-related defect center, which reduces the carrier lifetime under illumination and can be permanently deactivated under carrier injection at elevated temperature. We have for the first time investigated the deactivation process under actual regeneration conditions and as a function of the measured hydrogen content in the silicon bulk. Moreover, we have unambiguously demonstrated the benefits of adding a regeneration step in an industrial inline regeneration tool to lifetime samples, which underwent an industrial cell process sequence.

Typical industrial PERC solar cells fabricated on boron-doped p -type Cz-Si wafers were examined in darkness at elevated temperatures at different applied forward bias voltages V_{appl} , which define the electron concentration injected into the solar cell base via the p - n junction. Based on time-dependent electroluminescence measurements during regeneration, we have experimentally determined the injected excess carrier concentrations Δn during regeneration for different applied forward-bias voltages for the first time. The regeneration kinetics of the solar cells were in-situ measured by recording the time-dependent electrical cell current during regeneration. From the latter measurements, the regeneration rate constant R_{reg} was determined by mono-exponential fitting to the measured data. The in-situ measurements of the total recombination current of the cells combined with the illuminated I - V characteristics showed a successful permanent regeneration. A proportional increase of R_{reg} on Δn was observed, verifying the defect model proposed by Voronkov and Falster [9] showing that the regeneration rate constant is controlled by the injected excess carrier concentration Δn alone and photons are not required.

Via resistivity measurements we have directly measured the hydrogen content in the silicon bulk diffused into crystalline silicon from hydrogen-rich $\text{SiN}_x\text{:H}$ layers and $\text{Al}_2\text{O}_3/\text{SiN}_x\text{:H}$ stacks. Rapid thermal annealing (RTA) treatment in a conveyor-belt furnace was used to hydrogenate the samples. The total hydrogen concentration diffused into the silicon bulk was found to show a maximum as a function of the RTA peak temperature ϑ_{peak} . The ϑ_{peak} position of the maximum depends on the composition of the $\text{SiN}_x\text{:H}$ layer, as characterized by the refractive index n measured by ellipsometry at a wavelength of 633 nm. The largest total hydrogen concentration of $2 \times 10^{15} \text{ cm}^{-3}$ was detected for a silicon-rich $\text{SiN}_x\text{:H}$ layer with a refractive index of $n=2.3$ at $\vartheta_{\text{peak}} = 800^\circ\text{C}$. Increasing the peak temperature above 800°C led to a decrease in the in-diffused hydrogen concentration due to a decrease in the atomic density of the $\text{SiN}_x\text{:H}$ layer, as shown by FTIR measurements. A drastic reduction of the hydrogen in-diffusion was achieved by introducing an atomic-layer-deposited Al_2O_3 layer in-between the silicon-rich $\text{SiN}_x\text{:H}$ layer and the crystalline

silicon surface. A 5 nm thick Al_2O_3 layer led to a reduction of the in-diffused hydrogen concentration by a factor of ~ 5 at $\vartheta_{\text{peak}} = 680^\circ\text{C}$ and even thicker Al_2O_3 layers practically completely prevented hydrogen from diffusing through the Al_2O_3 layer. Thicker Al_2O_3 layers were found to be necessary at higher RTA peak temperatures for preventing hydrogen from diffusing into the silicon bulk. For example, to reduce the in-diffused hydrogen concentration into the silicon bulk by a factor of 4 at $\vartheta_{\text{peak}} = 800^\circ\text{C}$, a 20 nm thick Al_2O_3 layer was required. The results presented in this thesis hence prove for the first time that ultrathin Al_2O_3 layers of only a few nm are highly effective hydrogen diffusion barriers during contact firing processes. The adaption of such diffusion barriers could prove extremely use in the production of silicon solar cells, where hydrogen in-diffusion into the silicon bulk has recently been identified as one major reason for detrimental light-induced degradation effects.

Measurements of resistivity changes during dark-annealing were applied to RTA-treated Cz-Si and Float-zone silicon (Fz-Si) samples verifying that the hydrogen-boron pair formation is the same in defect-lean Fz-Si as in Cz-Si, the latter material known to contain significantly higher defect concentration, e.g. oxygen-related ones. Thereby, we were able to quantify the BO-related lifetime degradation and regeneration as a function of the in-diffused hydrogen concentration. Cz-Si lifetime samples were coated with Al_2O_3 layers of varying thickness and silicon-rich $\text{SiN}_x\text{:H}$ capping layers with a refractive index of 2.3, acting as hydrogen sources. By varying the Al_2O_3 thickness, acting as an effective hydrogen barrier, different hydrogen concentrations were realized. On one type of sample, the $\text{SiN}_x\text{:H}$ capping layer was omitted, leading to a minimum hydrogen bulk content. We have extracted the degradation rate constants R_{deg} and regeneration rate constants R_{reg} for the various introduced hydrogen concentrations by fitting the time evolution of the effective defect concentration $N_t^*(t)$. Under degradation conditions ($I_{\text{ill}} = 0.1$ suns, room temperature), all samples showed comparable degradation curves. The values for R_{deg} and the maximum effective defect concentration $N_{t,\text{max}}^*$ are independent of the hydrogen content, implying that hydrogen has no impact on the BO-related lifetime degradation process. Under regeneration conditions ($I_{\text{ill}} = 1$ suns, $\vartheta_{\text{reg}} = 160^\circ\text{C}$), our lifetime measurements or rather the evolution of the effective defect concentration showed that the regeneration rate constant R_{reg} increases linearly with increasing bulk hydrogen concentration. Importantly, extrapolation to zero hydrogen content, did still result in a finite R_{reg} of $\sim 30 \text{ h}^{-1}$, suggesting that two different regeneration mechanisms exist: one with hydrogen involvement and one without. Our experimental results have hence, for the first time, quantified the impact of hydrogen on the BO activation and permanent deactivation. These results agree with the previously proposed Voronkov-Falster model of the permanent BO deactivation.

Finally, we have examined the long-term stability of the carrier lifetime in boron-doped Cz-Si materials with different boron and oxygen concentrations, which were regenerated in an industrial belt furnace. The carrier lifetime evolution of state-of-the-art boron-doped Cz-Si materials as well as material stemming from the seed end of a crystal were examined at room temperature under 0.1 suns illumination intensity for up to 2.2 years after regeneration. Despite very high lifetimes measured directly after regeneration, we observed a subsequent renewed light-induced degradation in

all materials, although up to 72% reduced at a much lower degradation rate (up to two orders of magnitude lower) compared to the standard BO degradation. The activated defect was found to have a hole-to-electron capture time constant ratio Q in the range 9.5 ± 3.5 for all examined materials, which is comparable to the reported Q range for the BO defect. Hence, our results suggest that a fraction of BO was not fully removed by the fast industrial regeneration treatment. Due to the slower re-activation of the BO defect, the detailed degradation kinetics has, however, changed significantly, which is not explained by existing defect models. On the long term, we observed a second regeneration process during illumination near room temperature, which saturated after two years, except for the material stemming from the seed end, which was dominated by other background defects. This material also showed ring-like defect structures, which the other three materials did not show. The three state-of-the-art Cz-Si materials showed stable and high lifetimes above 1 ms after more than 2 years of light exposure. Typical industrial Cz-Si wafers with a resistivity of $(1.75 \pm 0.03) \Omega\text{cm}$ and an interstitial oxygen concentration of $(6.9 \pm 0.3) \times 10^{17} \text{cm}^{-3}$ even show lifetimes larger than 2 ms after regeneration and 2 years of light exposure.

Bibliography

- [1] J. Schmidt, A. G. Aberle and R. Hezel, "Investigation of carrier lifetime instabilities in Cz-grown silicon," in *Proc. 26th IEEE PVSC*, 1997, pp. 13–18.
- [2] J. Schmidt and K. Bothe, "Structure and transformation of the metastable boron- and oxygen-related defect center in crystalline silicon," *Physical Review B*, vol. 69, no. 2, p. 024107, 2004.
- [3] T. Niewelt, M. Selinger, N. E. Grant, W. Kwapil, J. D. Murphy, and M. C. Schubert, "Light-induced activation and deactivation of bulk defects in boron-doped float-zone silicon," *Journal of Applied Physics*, vol. 121, no. 18, p. 185702, 2017.
- [4] A. Herguth, G. Schubert, M. Kaes, and G. Hahn, "Avoiding boron-oxygen related degradation in highly doped Cz silicon," in *Proc. 21st EUPVSEC*, 2006, pp. 530–537.
- [5] F. Fertig, R. Lantzsich, A. Mohr, M. Schaper, M. Bartzsch, D. Wissen, F. Kersten, A. Mette, S. Peters, A. Eidner, J. Cieslak, K. Duncker, M. Junghänel, E. Jarzembowski, M. Kauert, B. Faulwetter-Quandt, D. Meißner, B. Reiche, S. Geißler, S. Hörnlein, C. Klenke, L. Niebergall, A. Schönmann, A. Weihrauch, F. Stenzel, A. Hofmann, T. Rudolph, A. Schwabedissen, M. Gundermann, M. Fischer, J. W. Müller, and D. Jeong, "Mass production of *p*-type Cz silicon solar cells approaching average stable conversion efficiencies of 22%," *Energy Procedia*, vol. 124, pp. 338–345, 2017.
- [6] B. Vicari Stefani, A. Soeriyadi, M. Wright, D. Chen, M. Kim, Y. Zhang, and B. Hallam, "Large-area boron-doped 1.6 Ωcm *p*-type Czochralski silicon heterojunction solar cells with a stable open-circuit voltage of 736 mV and efficiency of 22.0%," *Solar RRL*, vol. 4, no. 9, p. 2000134, 2020.
- [7] R. A. Sinton and A. Cuevas, "Contactless determination of current-voltage characteristics and minority-carrier lifetimes in semiconductors from quasi-steady-state photoconductance data," *Applied Physics Letters*, vol. 69, no. 17, pp. 2510–2512, 1996.
- [8] P. P. Altermatt, J. Schmidt, M. Kerr, G. Heiser, and A. G. Aberle, "Exciton-enhanced auger recombination in crystalline silicon under intermediate and high injection conditions," in *Proc. 16th EUPVSEC*, 2000, pp. 243–246.
- [9] V. Voronkov and R. Falster, "Permanent deactivation of boron-oxygen recombination centres in silicon," *physica status solidi (b)*, vol. 253, no. 9, pp. 1721–1728, 2016.

- [10] H. Nagel, C. Berge, and A. G. Aberle, “Generalized analysis of quasi-steady-state and quasi-transient measurements of carrier lifetimes in semiconductors,” *Journal of Applied Physics*, vol. 86, no. 11, pp. 6218–6221, 1999.
- [11] S. Herlufsen, J. Schmidt, D. Hinken, K. Bothe, and R. Brendel, “Photoconductance-calibrated photoluminescence lifetime imaging of crystalline silicon,” *physica status solidi (RRL) - Rapid Research Letters*, vol. 2, no. 6, pp. 245–247, 2008.
- [12] PV Lighthouse, “Wafer ray tracer,” Online: 19. September 2021, <https://www2.pvlighthouse.com.au/calculators/wafer%20ray%20tracer/wafer%20ray%20tracer.html>.
- [13] W. Bludau, A. Onton, and W. Heinke, “Temperature dependence of the band gap of silicon,” *Journal of Applied Physics*, vol. 45, no. 4, pp. 1846–1848, 1974.
- [14] BRUKER OPTIK GmbH, *VERTEX 70 Benutzerhandbuch*, 4th ed. Ettlingen: www.brukeroptics.com, 2010.
- [15] D. A. Skoog and J. J. Leary, *Instrumentelle Analytik: Grundlagen - Geräte - Anwendungen*. Berlin, Heidelberg: Springer Berlin Heidelberg, 1996, vol. I.
- [16] D. Bredemeier, “Light and elevated temperature induced degradation (LeTID) of the carrier lifetime in multicrystalline silicon,” PhD thesis, Leibniz Universität Hannover, Hannover, 2019.
- [17] R. E. Pritchard, J. H. Tucker, R. C. Newman, and E. C. Lightowers, “Hydrogen molecules in boron-doped crystalline silicon,” *Semiconductor Science and Technology*, vol. 14, pp. 77–80, 1999.
- [18] Z. Yin and F. W. Smith, “Optical dielectric function and infrared absorption of hydrogenated amorphous silicon nitride films: Experimental results and effective-medium-approximation analysis,” *Physical Review B*, vol. 42, no. 6, pp. 3666–3675, 1990.
- [19] D. Bredemeier, D. C. Walter, R. Heller, and J. Schmidt, “Impact of hydrogen-rich silicon nitride material properties on light-induced lifetime degradation in multicrystalline silicon,” *physica status solidi (RRL) - Rapid Research Letters*, vol. 13, p. 1900201, 2019.
- [20] H. Fujiwara and R. W. Collins, Eds., *Spectroscopic Ellipsometry for Photovoltaics: Volume 1: Fundamental Principles and Solar Cell Characterization*, ser. Springer Series in Optical Sciences. Cham: Springer International Publishing, 2018, vol. 212.
- [21] H. Fujiwara, *Spectroscopic Ellipsometry: Principles and Applications*. Chichester, UK: John Wiley & Sons, Ltd, 2007.
- [22] J. A. Woollam Co., “CompleteEASE software manual: Data Acquisition and Analysis Software for J.A. Woollam Co. Spectroscopic Ellipsometers,” 2014, https://wiki.nanotech.ucsb.edu/w/images/2/2e/CompleteEASE_Manual.pdf.

- [23] W. Kern, "The evolution of silicon wafer cleaning technology," *J. Electrochem. Soc.*, vol. 137, no. 6, pp. 1887–1892, 1990.
- [24] H.-P. Boehm, M. Schneider, and F. Arendt, "Der Wassergehalt "getrockneter" Siliciumdioxid-Oberflächen," *Zeitschrift für anorganische und allgemeine Chemie*, pp. 43–53, 1963.
- [25] R. K. Iler, *The chemistry of silica: Solubility, polymerization, colloid and surface properties, and biochemistry*. New York, NY: Wiley, 1979.
- [26] B. Veith-Wolf, "Crystalline silicon surface passivation using aluminum oxide: Fundamental understanding and application to solar cells," PhD thesis, Leibniz Universität Hannover, Hannover, 2018.
- [27] B. Hoex, J. Schmidt, P. Pohl, M. C. M. van de Sanden, and W. M. M. Kessels, "Silicon surface passivation by atomic layer deposited Al_2O_3 ," *Journal of Applied Physics*, vol. 104, no. 4, p. 044903, 2008.
- [28] G. Dingemans, M. C. M. van de Sanden, and W. M. M. Kessels, "Influence of the deposition temperature on the c-Si surface passivation by Al_2O_3 films synthesized by ALD and PECVD," *Electrochemical and Solid-State Letters*, vol. 13, no. 3, pp. H76–H79, 2010.
- [29] G. Dingemans, F. Einsele, W. Beyer, M. C. M. van de Sanden, and W. M. M. Kessels, "Influence of annealing and Al_2O_3 properties on the hydrogen-induced passivation of the Si/SiO₂ interface," *Journal of Applied Physics*, vol. 111, no. 9, p. 093713, 2012.
- [30] J. D. Moschner, J. Henze, J. Schmidt, and R. Hezel, "High-quality surface passivation of silicon solar cells in an industrial-type inline plasma silicon nitride deposition system," *Progress in Photovoltaics: Research and Applications*, vol. 12, 2004.
- [31] B. Lenkeit, "Elektronische und strukturelle Eigenschaften von Plasma-Siliziumnitrid zur Oberflächenpassivierung von siebgedruckten, bifazialen Silizium-Solarzellen," PhD thesis, Leibniz Universität Hannover, Hannover, 2002.
- [32] J. Robertson, "Defects and hydrogen in amorphous silicon nitride," *Philosophical Magazine B*, vol. 69, no. 2, pp. 307–326, 1994.
- [33] G. Kovačević and B. Pivac, "Reactions in silicon-nitrogen plasma," *Physical chemistry chemical physics : PCCP*, vol. 19, no. 5, pp. 3826–3836, 2017.
- [34] C. Boehme and G. Lucovsky, "Dissociation reactions of hydrogen in remote plasma-enhanced chemical-vapor-deposition silicon nitride," *Journal of Vacuum Science & Technology A: Vacuum, Surfaces, and Films*, vol. 19, no. 5, pp. 2622–2628, 2001.
- [35] S. Jafari, C. Chaitanya, and J. Hirsch, "Composition-dependent hydrogen effusion and diffusion mechanism within a-SiN_x:H," in *Proc. 34th EUPVSEC*, 2018, pp. 686–689.

- [36] S. Jafari, J. Hirsch, D. Lausch, M. John, N. Bernhard, and S. Meyer, "Composition limited hydrogen effusion rate of a-Si_x:H passivation stack," *AIP*, vol. 2147, p. 050004, 2019.
- [37] W. Beyer, "Diffusion and evolution of hydrogen in hydrogenated amorphous and microcrystalline silicon," *Solar Energy Materials and Solar Cells*, vol. 78, pp. 235–237, 2003.
- [38] H. Fischer, and W. Pschunder, "Investigation of photon and thermal induced changes in silicon solar cells," in *Proc. 10th IEEE PVSC*, 1974, pp. 404–411.
- [39] S. W. Glunz, S. Rein, W. Warta, J. Knobloch, and W. Wettling, "On the degradation of Cz-silicon solar cells," in *Proc. 2nd WCPVEC*, 1998, pp. 1343–1346.
- [40] S. W. Glunz, S. Rein, J. Y. Lee, and W. Warta, "Minority carrier lifetime degradation in boron-doped Czochralski silicon," *Journal of Applied Physics*, vol. 90, no. 5, pp. 2397–2404, 2001.
- [41] K. Bothe and J. Schmidt, "Electronically activated boron-oxygen-related recombination centers in crystalline silicon," *Journal of Applied Physics*, vol. 99, no. 1, p. 013701, 2006.
- [42] A. Herguth, "On the meaning(fullness) of the intensity unit 'suns' in light induced degradation experiments," *Energy Procedia*, vol. 124, pp. 53–59, 2017.
- [43] K. Bothe and J. Schmidt, "Fast-forming boron-oxygen-related recombination center in crystalline silicon," *Applied Physics Letters*, vol. 87, p. 262108, 2005.
- [44] D. W. Palmer, K. Bothe, and J. Schmidt, "Kinetics of the electronically stimulated formation of a boron-oxygen complex in crystalline silicon," *Physical Review B*, vol. 76, no. 3, pp. 133–138, 2007.
- [45] D. Macdonald, F. Rougieux, A. Cuevas, B. Lim, J. Schmidt, M. Di Sabatino, and L. J. Geerligs, "Light-induced boron-oxygen defect generation in compensated *p*-type Czochralski silicon," *Journal of Applied Physics*, vol. 105, no. 9, p. 093704, 2009.
- [46] B. Lim, F. Rougieux, D. Macdonald, K. Bothe, and J. Schmidt, "Generation and annihilation of boron–oxygen-related recombination centers in compensated *p*- and *n*-type silicon," *Journal of Applied Physics*, vol. 108, no. 10, p. 103722, 2010.
- [47] M. Forster, E. Fourmond, F. E. Rougieux, A. Cuevas, R. Gotoh, K. Fujiwara, S. Uda, and M. Lemitte, "Boron-oxygen defect in Czochralski-silicon co-doped with gallium and boron," *Applied Physics Letter*, vol. 100, p. 042110, 2012.
- [48] K. Bothe, J. Schmidt, and R. Hezel, "Effective reduction of the metastable defect concentration in boron-doped Czochralski silicon for solar cells," in *Proc. 29th IEEE PVSC*, 2002, pp. 194–197.

- [49] K. Bothe, R. Sinton, and J. Schmidt, "Fundamental boron-oxygen-related carrier lifetime limit in mono- and multicrystalline silicon," *Progress in Photovoltaics: Research and Applications*, vol. 13, no. 4, pp. 287–296, 2005.
- [50] S. Rein, T. Rehr, W. Warta, S. W. Glunz, and G. Willeke, "Electrical and thermal properties of the metastable defect in boron-doped Czochralski silicon (Cz-Si)," in *Proc. 17th EUPVSEC*, 2001, pp. 1555–1560.
- [51] J. Adey, R. Jones, D. W. Palmer, P. R. Briddon, and S. Oberg, "Degradation of boron-doped Czochralski-grown silicon solar cells," *Physical review letters*, vol. 93, no. 5, p. 055504, 2004.
- [52] J. Schmidt, K. Bothe, and R. Hazel, "Formation and annihilation of the metastable defect in boron-doped Czochralski silicon," in *Proc. 29th IEEE PVSC*, 2002, pp. 178–181.
- [53] A. Herguth, G. Schubert, M. Kaes, and G. Hahn, "A new approach to prevent the negative impact of the metastable defect in boron doped Cz-silicon solar cells," in *Proc. 32nd IEEE PVSC (4th WCPEC)*, 2006, pp. 940–943.
- [54] B. Lim, A. Liu, D. Macdonald, K. Bothe, and J. Schmidt, "Impact of dopant compensation on the deactivation of boron-oxygen recombination centers in crystalline silicon," *Applied Physics Letters*, vol. 95, p. 232109, 2009.
- [55] B. Lim, K. Bothe, and J. Schmidt, "Impact of oxygen on the permanent deactivation of boron–oxygen-related recombination centers in crystalline silicon," *Journal of Applied Physics*, vol. 107, no. 12, p. 123707, 2010.
- [56] S. Wilking, S. Ebert, C. Beckh, A. Herguth, and G. Hahn, "Of apples and oranges: Why comparing BO regeneration rates requires injection level correction," in *Proc. 32nd EUPVSEC*, 2016, pp. 487–494.
- [57] V. Steckenreiter, D. C. Walter, and J. Schmidt, "Kinetics of the permanent deactivation of the boron-oxygen complex in crystalline silicon as a function of illumination intensity," *AIP Advances*, vol. 7, no. 3, p. 035305, 2017.
- [58] A. Herguth and G. Hahn, "Kinetics of the boron-oxygen related defect in theory and experiment," *Journal of Applied Physics*, vol. 108, no. 11, p. 114509, 2010.
- [59] B. Lim, S. Hermann, K. Bothe, J. Schmidt, and R. Brendel, "Permanent deactivation of the boron-oxygen recombination center in silicon solar cells," in *Proc. 23rd EUPVSEC*, 2008, pp. 1018–1022.
- [60] A. Herguth, G. Schubert, M. Kaes, and G. Hahn, "Investigations on the long time behavior of the metastable boron–oxygen complex in crystalline silicon," *Progress in Photovoltaics: Research and Applications*, vol. 16, no. 2, pp. 135–140, 2008.
- [61] V. Steckenreiter, D. C. Walter, and J. Schmidt, "Two-stage permanent deactivation of the boron-oxygen-related recombination center in crystalline silicon," *Energy Procedia*, vol. 124, pp. 799–805, 2017.

- [62] D. C. Walter, B. Lim, K. Bothe, V. V. Voronkov, R. Falster, and J. Schmidt, "Effect of rapid thermal annealing on recombination centres in boron-doped Czochralski-grown silicon," *Applied Physics Letters*, no. 4, pp. 0421 11–1 – 0421 11–4, 2014.
- [63] S. Wilking, S. Ebert, A. Herguth, and G. Hahn, "Influence of short high temperature steps on the regeneration of boron-oxygen related defects," in *Proc. 28th EUPVSEC*, 2013, pp. 34–38.
- [64] B. Lim, K. Bothe, and J. Schmidt, "Deactivation of the boron–oxygen recombination center in silicon by illumination at elevated temperature," *physica status solidi (RRL) – Rapid Research Letters*, vol. 2, no. 3, pp. 93–95, 2008.
- [65] K. A. Münzer, "Hydrogenated silicon nitride for regeneration of light induced degradation," in *Proc. 24th EUPVSEC*, 2009, pp. 1558–1561.
- [66] N. Nampalli, B. Hallam, C. Chan, M. Abbott, and S. Wenham, "Evidence for the role of hydrogen in the stabilization of minority carrier lifetime in boron-doped Czochralski silicon," *Applied Physics Letters*, vol. 106, pp. 173 501–1–5, 2015.
- [67] D. C. Walter and J. Schmidt, "Impact of hydrogen on the permanent deactivation of the boron-oxygen-related recombination center in crystalline silicon," *Solar Energy Materials and Solar Cells*, vol. 158, pp. 91–97, 2016.
- [68] S. Wilking, A. Herguth, and G. Hahn, "Influence of hydrogen on the regeneration of boron-oxygen related defects in crystalline silicon," *Journal of Applied Physics*, vol. 113, no. 19, p. 194503, 2013.
- [69] M. Gläser and D. Lausch, "Towards a quantitative model for BO regeneration by means of charge state control of hydrogen," *Energy Procedia*, vol. 77, pp. 592–598, 2015.
- [70] D. C. Walter, D. Bredemeier, R. Falster, V. V. Voronkov, and J. Schmidt, "Easy-to-apply methodology to measure the hydrogen concentration in boron-doped crystalline silicon," *Solar Energy Materials and Solar Cells*, vol. 200, p. 109970, 2019.
- [71] F. A. Stevie, C. Zhou, M. Hopstaken, M. Saccomanno, Z. Zhang, and A. Turansky, "SIMS measurement of hydrogen and deuterium detection limits in silicon: Comparison of different SIMS instrumentation," *Journal of Vacuum Science & Technology B, Nanotechnology and Microelectronics: Materials, Processing, Measurement, and Phenomena*, vol. 34, no. 3, p. 03H103, 2016.
- [72] U. Gösele and T. Y. Tan, "Oxygen diffusion and thermal donor formation in silicon," *Appl. Phys. A*, vol. 28, pp. 79–92, 1982.
- [73] L. I. Murin, T. Hallberg, V. P. Markevich, and J. L. Lindström, "Experimental evidence of the oxygen dimer in silicon," *Physical review letters*, vol. 80, no. 1, pp. 93–96, 1998.

- [74] Y. J. Lee, J. von Boehm, M. Pesola, and R. M. Nieminen, “Aggregation kinetics of thermal double donors in silicon,” *Physical review letters*, vol. 86, no. 14, pp. 3060–3063, 2001.
- [75] J. C. Bourgoin and J. W. Corbett, “A new mechanism for interstitial migration,” *Physics Letters*, vol. 38A, no. 2, pp. 135–137, 1972.
- [76] K. Bothe, R. Hezel, and J. Schmidt, “Recombination-enhanced formation of the metastable boron–oxygen complex in crystalline silicon,” *Applied Physics Letters*, vol. 83, no. 6, pp. 1125–1127, 2003.
- [77] V. V. Voronkov and R. Falster, “Latent complexes of interstitial boron and oxygen dimers as a reason for degradation of silicon-based solar cells,” *Journal of Applied Physics*, vol. 107, no. 5, p. 053509, 2010.
- [78] R. D. Harris, J. L. Newton, and G. D. Watkins, “Negative-U defect: Interstitial boron in silicon,” *Physical Review B*, vol. 36, no. 2, pp. 1094–1104, 1987.
- [79] V. V. Voronkov, R. Falster, K. Bothe, and B. Lim, “Light-induced lifetime degradation in boron-doped Czochralski silicon: Are oxygen dimers involved?” in *Proc. 3rd SiliconPV*, vol. 38, 2013, pp. 636–641.
- [80] V. V. Voronkov and R. Falster, “Light-induced boron-oxygen recombination centres in silicon: Understanding their formation and elimination,” *Solid State Phenomena*, vol. 205-206, pp. 3–14, 2013.
- [81] V. V. Voronkov and R. Falster, “Formation, dissociation, and diffusion of various hydrogen dimers in silicon,” *physica status solidi (b)*, vol. 254, no. 6, p. 1600779, 2017.
- [82] T. Dullweber and J. Schmidt, “Industrial silicon solar cells applying the passivated emitter and rear cell (PERC) concept—a review,” *IEEE Journal of Photovoltaics*, vol. 6, no. 5, pp. 1366–1381, 2016.
- [83] A. Herguth, G. Schubert, M. Kaes, and G. Hahn, “Further investigations of the avoidance of boron-oxygen related degradation by means of regeneration,” in *Proc. 22nd EUPVSEC*, 2007, pp. 893–896.
- [84] D. Hinken, K. Ramspeck, K. Bothe, B. Fischer, and R. Brendel, “Series resistance imaging of solar cells by voltage dependent electroluminescence,” *Applied Physics Letters*, vol. 91, no. 18, p. 182104, 2007.
- [85] K. Misiakos and D. Tsamakis, “Accurate measurements of the silicon intrinsic carrier density from 78 to 340 K,” *Journal of Applied Physics*, no. 74, pp. 3293–3297, 1993.
- [86] T. Mchedlidze, A. Herguth, and J. Weber, “Monitoring of Si-solar cell degradation with electroluminescence,” *Solar Energy Materials and Solar Cells*, vol. 155, pp. 38–42, 2016.

- [87] T. Pernau, O. Romer, W. Scheiffele, A. Reichart, and W. Jooß, “Rather high speed regeneration of BO-defects: Regeneration experiments with large cell batches,” in *Proc. 31st EUPVSEC*, 2015, pp. 918–920.
- [88] D. C. Walter, L. Helmich, D. Bredemeier, R. Falster, V. V. Voronkov, and J. Schmidt, “Lifetime evolution during regeneration in boron-doped Czochralski-silicon,” in *Proc. 35th EUPVSEC*, 2018, pp. 522–526.
- [89] M. Kim, D. Chen, M. Abbott, S. Wenham, and B. Hallam, “Role of hydrogen: Formation and passivation of meta-stable defects due to hydrogen in silicon,” in *Proc. 8th SiliconPV*, 2018, p. 130010.
- [90] D. Bredemeier, D. C. Walter, R. Heller, and J. Schmidt, “Impact of silicon nitride film properties on hydrogen in-diffusion into crystalline silicon,” in *Proc. 36th EUPVSEC*, 2019, pp. 112–115.
- [91] J. Hong, W. M. M. Kessels, W. J. Soppe, A. W. Weeber, W. M. Arnoldbik, and M. C. M. van de Sanden, “Influence of the high-temperature “firing” step on high-rate plasma deposited silicon nitride films used as bulk passivating antireflection coatings on silicon solar cells,” *Journal of Vacuum Science & Technology B: Microelectronics and Nanometer Structures*, vol. 21, no. 5, p. 2123, 2003.
- [92] B. J. Hallam, S. R. Wenham, P. G. Hamer, M. D. Abbott, A. Sugianto, C. E. Chan, A. M. Wenham, M. G. Eadie, and G. Xu, “Hydrogen passivation of B-O defects in Czochralski silicon,” *Energy Procedia*, vol. 38, pp. 561–570, 2013.
- [93] S. J. Pearton, J. W. Corbett, and T. S. Shi, “Hydrogen in crystalline semiconductors,” *Applied Physics A Solids and Surfaces*, vol. 43, pp. 153–195, 1987.
- [94] B. L. Sopori, X. Deng, J. P. Benner, A. Rohatgi, P. Sana, S. K. Estreicher, Y. K. Park, and M. A. Roberson, “Hydrogen in silicon: A discussion of diffusion and passivation mechanisms,” *Solar Energy Materials and Solar Cells*, vol. 41/42, pp. 159–169, 1996.
- [95] D. Bredemeier, D. C. Walter, and J. Schmidt, “Possible candidates for impurities in mc-Si wafers responsible for light-induced lifetime degradation and regeneration,” *Solar RRL*, vol. 2, no. 1, p. 1700159, 2018.
- [96] P. M. Weiser, E. Monakhov, H. Haug, M. S. Wiig, and R. Søndena, “Hydrogen-related defects measured by infrared spectroscopy in multicrystalline silicon wafers throughout an illuminated annealing process,” *Journal of Applied Physics*, vol. 127, no. 6, p. 065703, 2020.
- [97] D. Chen, P. Hamer, M. Kim, C. Chan, A. Ciesla nee Wenham, F. Rougieux, Y. Zhang, M. Abbott, and B. Hallam, “Hydrogen-induced degradation: Explaining the mechanism behind light- and elevated temperature-induced degradation in *n*- and *p*-type silicon,” *Solar Energy Materials and Solar Cells*, vol. 207, p. 110353, 2020.

- [98] R. Eberle, W. Kwapil, F. Schindler, S. W. Glunz, and M. C. Schubert, “Firing temperature profile impact on light induced degradation in multicrystalline silicon,” *Energy Procedia*, vol. 124, pp. 712–717, 2017.
- [99] A. A. Dameron, S. D. Davidson, B. B. Burton, P. F. Carcia, R. S. McLean, and S. M. George, “Gas diffusion barriers on polymers using multilayers fabricated by Al_2O_3 and rapid SiO_2 atomic layer deposition,” *J. Phys. Chem. C*, no. 112, pp. 4573–4580, 2008.
- [100] S. Wilking, S. Ebert, A. Herguth, and G. Hahn, “Influence of hydrogen effusion from hydrogenated silicon nitride layers on the regeneration of boron-oxygen related defects in crystalline silicon,” *Journal of Applied Physics*, vol. 114, no. 19, p. 194512, 2013.
- [101] A. F. Holleman, N. Wiberg, and G. Fischer, *Lehrbuch der Anorganischen Chemie*. Berlin - New York: Walter de Gruyter, 2007.
- [102] W. M. Bullis and H. R. Huff, “Interpretation of carrier recombination lifetime and diffusion length measurements in silicon,” *Journal of The Electrochemical Society*, vol. 143, no. 4, pp. 1399–1405, 1996.
- [103] J. Schmidt, D. Bredemeier, and D. C. Walter, “On the defect physics behind light and elevated temperature-induced degradation (LeTID) of multicrystalline silicon solar cells,” *IEEE Journal of Photovoltaics*, vol. 9, no. 6, pp. 1497–1503, 2019.
- [104] D. C. Walter, D. Bredemeier, R. Falster, V. V. Voronkov, and J. Schmidt, “Disappearance of hydrogen-boron-pairs in silicon during illumination and its relevance to lifetime degradation and regeneration effects in solar cells,” in *Proc. 37th EUPVSEC*, 2020, pp. 140–144.
- [105] D. Bredemeier, D. C. Walter, R. Heller, and J. Schmidt, “Impact of hydrogen-rich silicon nitride material properties on light-induced lifetime degradation in multicrystalline silicon,” *physica status solidi (RRL) – Rapid Research Letters*, vol. 13, p. 1900201, 2019.
- [106] U. Varshney, B. Hallam, P. Hamer, A. Ciesla, D. Chen, S. Liu, C. Sen, A. Samadi, M. Abbott, C. Chan, and B. Hoex, “Controlling light- and elevated-temperature-induced degradation with thin film barrier layers,” *IEEE Journal of Photovoltaics*, vol. 10, no. 1, pp. 19–27, 2020.
- [107] D. C. Walter, B. Lim, V. V. Voronkov, R. Falster, and J. Schmidt, “Investigation of the lifetime stability after regeneration in boron-doped Cz silicon,” in *Proc. 29th EUPVSEC*, 2014, pp. 555–559.
- [108] D. Sperber, A. Herguth, and G. Hahn, “On improved passivation stability on highly-doped crystalline silicon and the long-term stability of regenerated Cz-Si,” *Solar Energy Materials and Solar Cells*, vol. 185, pp. 277–282, 2018.
- [109] D. C. Walter, V. Steckenreiter, L. Helmich, T. Pernau, and J. Schmidt, “Production-compatible regeneration of boron-doped Czochralski-silicon in a

- combined fast-firing and regeneration belt-line furnace,” in *Proc. 33rd EU-PVSEC*, 2017, pp. 377–381.
- [110] C. Derricks, A. Herguth, G. Hahn, O. Romer, and T. Pernau, “Industrially applicable mitigation of BO-LID in Cz-Si PERC-type solar cells within a coupled fast firing and halogen lamp based belt-line regenerator – a parameter study,” *Solar Energy Materials and Solar Cells*, vol. 195, pp. 358–366, 2019.
- [111] D. C. Walter, B. Lim, K. Bothe, R. Falster, V. V. Voronkov, and J. Schmidt, “Lifetimes exceeding 1 ms in 1- Ω cm boron-doped Cz silicon,” *Solar Energy Materials and Solar Cells*, vol. 131, pp. 51–57, 2014.
- [112] K. R. McIntosh and R. A. Sinton, “Uncertainty in photoconductance lifetime measurements that use an inductive-coil detector,” in *Proc. 23rd EUPVSEC*, 2008, pp. 77–82.
- [113] D. Sperber, A. Graf, D. Skorka, A. Herguth, and G. Hahn, “Degradation of surface passivation on crystalline silicon and its impact on light-induced degradation experiments,” *IEEE Journal of Photovoltaics*, vol. 7, no. 6, pp. 1627–1634, 2017.
- [114] J. Haunschild, I. E. Reis, J. Geilker, and S. Rein, “Detecting efficiency-limiting defects in Czochralski-grown silicon wafers in solar cell production using photoluminescence imaging,” *physica status solidi (RRL) - Rapid Research Letters*, vol. 5, no. 5-6, pp. 199–201, 2011.
- [115] J. Schmidt, “Temperature- and injection-dependent lifetime spectroscopy for the characterization of defect centers in semiconductors,” *Applied Physics Letters*, vol. 82, no. 13, pp. 2178–2180, 2003.
- [116] J. D. Murphy, K. Bothe, R. Krain, V. V. Voronkov, and R. J. Falster, “Parameterisation of injection-dependent lifetime measurements in semiconductors in terms of Shockley-Read-Hall statistics: An application to oxide precipitates in silicon,” *Journal of Applied Physics*, vol. 111, no. 11, pp. 113 709–1–113 709–10, 2012.
- [117] V. V. Voronkov, R. Falster, K. Bothe, B. Lim, and J. Schmidt, “Lifetime-degrading boron-oxygen centres in *p*-type and *n*-type compensated silicon,” *Journal of Applied Physics*, vol. 110, no. 6, p. 063515, 2011.
- [118] J. Schmidt and A. Cuevas, “Electronic properties of the recombination centers responsible for the light-induced carrier lifetime degradation in boron-doped Czochralski silicon,” *Journal of Applied Physics*, vol. 86, no. 6, p. 3175, 1999.
- [119] S. Rein and S. W. Glunz, “Electronic properties of the metastable defect in boron-doped Czochralski silicon: Unambiguous determination by advanced lifetime spectroscopy,” *Applied Physics Letters*, vol. 82, no. 7, pp. 1054–1056, 2003.
- [120] J. Schmidt, K. Bothe, V. V. Voronkov, and R. Falster, “Fast and slow stages of lifetime degradation by boron–oxygen centers in crystalline silicon,” *physica status solidi (b)*, vol. 116, p. 1900167, 2019.

-
- [121] D. Bredemeier, D. Walter, S. Herlufsen, and J. Schmidt, “Understanding the light-induced lifetime degradation and regeneration in multicrystalline silicon,” *Energy Procedia*, vol. 92, pp. 773–778, 2016.
- [122] A. E. Morishige, M. A. Jensen, D. B. Needleman, K. Nakayashiki, J. Hofstetter, T.-T. A. Li, and T. Buonassisi, “Lifetime spectroscopy investigation of light-induced degradation in *p*-type multicrystalline silicon PERC,” *IEEE Journal of Photovoltaics*, vol. 6, no. 6, pp. 1466–1472, 2016.
- [123] M. Winter, D. Walter, D. Bredemeier, and J. Schmidt, “Light-induced lifetime degradation effects at elevated temperature in Czochralski-grown silicon beyond boron-oxygen-related degradation,” *Solar Energy Materials and Solar Cells*, vol. 201, p. 110060, 2019.
- [124] G. Hahn, S. Wilking, and A. Herguth, “BO-related defects: Overcoming bulk lifetime degradation in crystalline Si by regeneration,” *Solid State Phenomena*, vol. 242, pp. 80–89, 2015.
- [125] S. Wilking, M. Forster, A. Herguth, and G. Hahn, “From simulation to experiment: Understanding BO-regeneration kinetics,” *Solar Energy Materials and Solar Cells*, vol. 142, pp. 87–91, 2015.
- [126] N. Nampalli, H. Li, M. Kim, B. Stefani, S. Wenham, B. Hallam, and M. Abbott, “Multiple pathways for permanent deactivation of boron-oxygen defects in *p*-type silicon,” *Solar Energy Materials and Solar Cells*, vol. 173, pp. 12–17, 2017.

Publications

Publications published within this thesis:

List of peer-reviewed journal papers

1. L. Helmich, D. C. Walter; D. Bredemeier, R. Falster, V. V. Voronkov, and J. Schmidt, “In-situ characterization of electron-assisted regeneration of Cz-Si solar cells”, *Solar Energy Materials and Solar Cells*, vol. 185, pp. 283–286, 2018.
2. L. Helmich, D. C. Walter, and J. Schmidt, “Direct examination of the deactivation of the boron-oxygen center in Cz-Si solar cells under regeneration conditions via electroluminescence”, *IEEE Journal of Photovoltaics*, vol. 9, pp. 1472–1476, 2019.
3. L. Helmich, D. C. Walter, D. Bredemeier, and J. Schmidt, “Atomic-Layer-Deposited Al₂O₃ as effective barrier against the diffusion of hydrogen from SiN_x:H layers into crystalline silicon during rapid thermal annealing”, *Phys. Status Solidi RRL*, vol. 96, pp. 2000367, 2020.
4. L. Helmich, D. C. Walter, R. Falster, V.V. Voronkov, and J. Schmidt, “Impact of hydrogen on the boron-oxygen-related lifetime degradation and regeneration kinetics in crystalline silicon”, *Solar Energy Materials and Solar Cells*, vol. 232, pp. 111340, 2021.
5. L. Helmich, D. C. Walter, T. Pernau, and J. Schmidt, “Carrier lifetime stability of boron-doped Czochralski-grown silicon materials for years after regeneration in an industrial belt furnace”, *IEEE Journal of Photovoltaics*, vol. 12, no. 1, pp. 198-203, 2022.

List of papers in conference proceedings

1. D. C. Walter, V. Steckenreiter, L. Helmich, T. Pernau, and J. Schmidt, “Production-compatible regeneration of boron-doped Czochralski-silicon in a combined fast-firing and regeneration belt-line furnace”, in *Proc. 33rd European Photovoltaic Solar Energy Conference*, Amsterdam, the Netherlands, 2017, pp. 377–381.

2. D. C. Walter, L. Helmich, D. Bredemeier, R. Falster, V.V. Voronkov, and J. Schmidt, “Lifetime evolution during regeneration in boron-doped Czochralski-silicon”, *Proc. 35th European Photovoltaic Solar Energy Conference*, Brussels, Belgium, 2018, pp. 522–526.
3. D. C. Walter, L. Helmich, T. Pernau, O. Romer, and J. Schmidt, “Comparing Cz-Si PERC solar cells from various manufacturers regarding BO-related light-induced degradation and regeneration”, *Proc. 36th European Photovoltaic Solar Energy Conference*, Marseille, France, 2019, pp. 464–467.
4. M. Winter, L. Helmich, D.C. Walter, and J. Schmidt, “Firing-Triggered LID (FT-LID) of the Carrier Lifetime in Cz-Si”, *Proc. 37th European Photovoltaic Solar Energy Conference*, Programme Online, 2020, pp. 462–467.
5. T. Pernau, C. Derricks, G. Hahn, L. Helmich, A. Herguth, J. Schmidt, D.C. Walter, “Upgrade Technologies for silicon photovoltaics – PART I: Industrial solution to minimize the negative impact of light induced degradation”, *Proc. 37th European Photovoltaic Solar Energy Conference*, Programme Online, 2020, pp. 414–417.

List of Figures

2.1	Schematic of the experimental setup of the WCT-120 System from Sinton Instruments.	5
2.2	Calibration of the coil for lifetime measurements in the experimental setup of the WCT-120 System from Sinton Instruments by different calibration wafers with different conductances.	6
2.3	Illumination intensity I_{ill} (straight line) and photoconductance $\Delta\sigma_{\text{ph}}$ (dashed line) plotted versus time t , measured by means of the WCT-120 System from Sinton Instruments. (a) Quasi-Steady-State Photoconductance (QSSPC) mode with a long flash and (b) Photoconductance Decay (PCD) technique with a short flash pulse compared to the lifetime of the Si sample.	8
2.4	Injection-dependent lifetimes after complete degradation under illumination at room temperature (open triangles) and after annealing in darkness (open circles) for an $1.7\ \Omega\text{cm}$ p -type Cz-Si sample with an $\text{Al}_2\text{O}_3/\text{SiN}_x$ -stack on both surfaces for passivation. According to the measured resistivity and Fourier-Transform-Infrared (FTIR) spectrum the sample has a boron concentration N_{A} about $8.3 \times 10^{15}\ \text{cm}^{-3}$ and an oxygen concentration $[\text{O}_i]$ of $7 \times 10^{17}\ \text{cm}^{-3}$. The green solid lifetime curve represents the lifetime of the activated defect, obtained by Eq.(2.10).	9
2.5	(a) Schematic of the photoconductance-calibrated photoluminescence imaging (PC-PLI) setup for spatially resolved measurements of the carrier lifetime, taken from [11]. (b) Photoluminescence (PL) image of an $1.6\ \Omega\text{cm}$ p -type Cz-Si sample with an $\text{Al}_2\text{O}_3/\text{SiN}_x$ -stack on both surfaces for passivation at a laser intensity of 0.9 suns.	10
2.6	(a) PL-calibration for a p -type $\text{Al}_2\text{O}_3/\text{SiN}_x$ -passivated Cz-Si lifetime sample by different laser intensities between 0.009 and 0.9 suns in steady-state mode. (b) Spatially resolved excess carrier image and (c) spatially resolved carrier lifetime image at a laser intensity of 0.9 suns.	11
2.7	Schematic of the electroluminescence (EL) imaging setup for determination of the injected excess carrier concentration Δn . (b) EL image of a passivated emitter and rear cell (PERC) fabricated on a boron-doped p -type Cz-Si wafer.	12
2.8	Schematic of the beam path and basic working principle within an interferometer.	13
2.9	Measured transmission T due to Si–O–Si vibration modes in dependence on the wave number $\bar{\nu}$ of a polished Cz-Si wafer.	14

2.10	Measured transmission T due to N–H, Si–H and Si–N vibration modes in dependence on the wave number $\bar{\nu}$ of a symmetrically passivated Fz-Si sample by single layers of SiN _x :H with a refractive index of $n = 2.3$	16
2.11	Calibration of the coil for resistivity measurements in the experimental setup of the WCT-120 System from Sinton Instruments by different calibration wafers with a different doping concentration or rather conductance. The $\sigma(V)$ dependence is linear for sufficiently low σ values (< 0.2 Siemens).	18
2.12	Schematic of the basic measurement principle of ellipsometry in accordance with the used Woollam M-2000UI ellipsometry tool in this work.	19
2.13	Exemplary ellipsometry measurement data: (a) amplitude ratio Ψ and (b) phase difference Δ as shown symbols, which are fitted (solid lines) using optical models. The measurement was performed at the Brewster angle of silicon ($\theta_B = 70^\circ$).	20
2.14	Refractive index n (solid line, corresponding to left y-axis) and extinction coefficient k (dashed line, corresponding to right x-axis) as a function of the wavelength λ obtained from fits of the ellipsometry measurement data using a model including optical properties of a Al ₂ O ₃ /SiN _x stack of layers. The SiN _x layer shows a refractive index n of 2.35 for light with a wavelength λ of 633 nm (open square).	21
2.15	(a) FlexAL TM (Oxford Instruments) for atomic layer deposition of Al ₂ O ₃ used throughout this work.(b) Schematic of the ALD deposition chamber, taken from [26].	22
2.16	(a) Structure of the silicon surface with silanol groups (Si-OH) after the RCA cleaning. For simplification, only free hydroxyl-groups are illustrated without any siloxane groups (Si-O-Si) on the surface. (b) Chemical reactions within one cycle of the PA-ALD process consisting of two half-cycles, depositing an aluminum oxide layer. Precursors are trimethylaluminium (TMA) in the first half-cycle and plasma-generated oxygen radicals, i.e. atomic oxygen, in the second half-cycle.	23
2.17	(a) Schematic of the inline PECVD SiNA system from Meyer Burger Technology AG, taken from [30], used for silicon nitride deposition on $156 \times 156 \text{ mm}^2$ sized silicon wafers. (b) Schematic of the remote-PECVD reactor of the Plasmalab 80 Plus system, taken from [31], used for silicon nitride deposition on smaller silicon samples.	25

3.1	(a) Typical lifetime evolution of an 1.1 Ωcm boron-doped p -type Cz-Si sample with an $\text{Al}_2\text{O}_3/\text{SiN}_x$ -stack, which is illuminated by an illumination intensity of $I_{\text{ill}} = 0.1$ suns ($10 \text{ mW}/\text{cm}^2$) near room temperature ($(25 \pm 3)^\circ\text{C}$). The lifetime is measured at 30°C and analyzed at an excess carrier density of $\Delta n = 1 \times 10^{15} \text{ cm}^{-3}$. (b) Calculated effective defect concentration N_t^* from the measured lifetimes $\tau(t)$ and the lifetime τ_0 directly measured after annealing in darkness at 200°C . The N_t^* evolution with the maximum effective defect concentration $N_{t,\text{max}}^*$ can be described by an exponential rise-to-maximum function with one degradation rate constant R_{deg}	28
3.2	Degradation rate constant R_{deg} of the fast and the slow stages of degradation versus (a) the boron concentration N_{dop} and (b) the interstitial oxygen concentration $[\text{O}_i]$ according to Bothe and Schmidt [41].	29
3.3	Degradation rate constant for non-compensated and dopant-compensated p -type Cz-Si samples in dependence on the square of net doping concentration p_0^2 and the product of the net doping and the total boron concentration $p_0 \times N_A$ according to Lim et al. [46].	30
3.4	Measured degradation rate constants R_{deg} versus the illumination intensity I_{ill} and thus versus different injected carrier concentrations according to Schmidt and Bothe [2].	31
3.5	(a) Typical lifetime evolution of an 1.1 Ωcm boron-doped p -type Cz-Si sample with an $\text{Al}_2\text{O}_3/\text{SiN}_x$ -stack, which is illuminated at elevated temperature ($I_{\text{ill}} = 1$ sun, 185°C). This treatment deactivates the boron-oxygen defect and regenerates the lifetime to the so-called permanent lifetime τ_{0p} . The lifetime is measured at 30°C and analyzed at an excess carrier density of $\Delta n = 1 \times 10^{15} \text{ cm}^{-3}$. (b) Calculated effective defect concentration N_t^* versus the illumination time t_{ill} , which can be described by an exponential decay function with a single regeneration rate constant R_{reg}	32
3.6	Regeneration rate constant R_{reg} versus (a) the boron concentration N_A according to Lim et al. [54] and (b) the interstitial oxygen concentration $[\text{O}_i]$ according to Lim et al. [55].	33
3.7	Regeneration rate constant R_{reg} in dependence on the cooling rate $-d\vartheta/dt$ according to Walter et al. [62].	34
3.8	Regeneration rate constant R_{reg} versus the inverse regeneration temperature $1000/T$ according to Lim et al. [64].	35
3.9	Energy profile for the oxygen dimer diffusion in different configurations according to Adey et al. [51]. The red arrows describe the diffusion via a <i>Bourgoin mechanism</i>	37

3.10	Free energy diagrams of the latent centre (LC) and the slowly formed recombination-active center (SRC) of the B_iO_{2i} defect in different charge states within the B_iO_{2i} defect model proposed by Voronkov and Falster [77]. The black arrows describe the model of transition (a) from a double-positive charge state through a transient configuration (TC) by overcoming the free energy barrier F_{ts} (defect activation) and (b) from an initial single-positive charge state to a neutral state by overcoming the transition barrier $F_{sl}^* - \mu$ (defect deactivation).	39
3.11	Schematic of the defect activation and deactivation mechanism in the B_iO_{2i} defect model proposed by Voronkov and Falster [77]. The latent complex $B_iO_{2i}^+$ recharges into the neutral state LC^0 in the presence of excess electrons, which is the starting state in the transition path of activation. The transition path of deactivation in darkness starts with the defect complex in the single-positive charge state.	41
4.1	Regeneration rate constant R_{reg} measured as a function of illumination intensity I_{ill} for boron-doped Cz-Si wafers with a linear fit of the data points (black line), taken from [57].	46
4.2	Typical lifetime evolution of an 1.6 Ω cm boron-doped p -type Cz-Si sample with an Al_2O_3/SiN_x -stack, which is regenerated by an illumination intensity of 1 sun at 185°C and measured at 30°C. (a) The lifetime evolution at a fixed excess carrier density of $\Delta n = 1 \times 10^{15} \text{ cm}^{-3}$ can be described by an exponential rise to maximum function with one regeneration rate constant R_{de} . The effective lifetimes are extracted from (b) the injection-dependent lifetime during the regeneration process (marked by star symbols). Differently colored curves correspond to different times of illumination at elevated temperature before the lifetime measurement at room temperature.	47
4.3	Photo of the clamped solar cell placed on the hot plate.	48
4.4	Schematic of our set-up A for the in-situ regeneration experiments in darkness.	48
4.5	Set-up B for the in-situ measurements of the cell current I_{cell} and the EL intensity Φ_{EL} during regeneration. (a) The front side of the solar cell is contacted by a copper wire centrally inserted into the window of the top brass plate. The rear side is fully contacted by a brass plate. We apply a forward-bias voltage V_{appl} between the two brass plates and detect the resulting EL signal during regeneration using a silicon charge-coupled device (Si-CCD) camera. The cell current is measured via a voltage-drop over a resistance of 0.1 Ω . (b) The EL intensity is analyzed next to the busbar, where the solar cell is contacted by a copper wire.	49
4.6	The typical two-stage degradation, as known from the literature [41], can also be observed in the dark cell current, if a constant forward-bias voltage (in this case $V_{appl} = 602 \text{ mV}$) is applied to the cell at room temperature.	50

4.7	Evolution of the cell current I_{cell} under two different constant applied forward-bias voltages V_{appl} at 140 °C in darkness. The solid black lines show fits of double-exponential decay functions. V_{appl} is kept constant during each regeneration experiment.	51
4.8	Evolution of (a) efficiency η and (b) open-circuit voltage V_{oc} after regeneration by electron injection in the dark (squares). In comparison, the degraded state (circle, gray data point) and the dark-annealed state (triangle, red data point) are shown. The scatter of measurement data refer to the reproducibility by the contacting of the solar cell.	52
4.9	Dark I - V characteristics measured at 140 °C by set-up A shown as red circles and set-up B shown as blue triangles.	53
4.10	(a) Left y-axis shows the measured EL intensities $\Phi_{\text{i,EL}}$ at different applied voltages V_{appl} at 140 °C and of three exemplary regeneration curves. The lower x-axis corresponds to the voltage applied to the solar cell during regeneration, which is kept constant over sense contacts. The upper x-axis corresponds to the locally applied voltage at the p - n junction V_i . From the measured EL intensities (filled triangles), the injected excess carrier concentration Δn (open circles) can be determined in dependence of the applied voltages. These data refer to the right y-axis. (b) Excess carrier concentration Δn is practically constant during regeneration (filled squares). The Δn value is in the regenerated state (reg.) slightly higher than in the degraded state (deg.).	55
4.11	<i>In-situ</i> EL and I - V measurements during regeneration at elevated temperatures. (a) Current through the cell I_{cell} (filled circles) measured at 140 °C and an applied voltage of $V_{\text{appl}} = 520$ mV proceeds in the opposite direction to the EL curve (filled triangles). In this case, the exposure time t_{Int} of the voltage is about 0.8 s. The regeneration curve (red line) can be described by one regeneration rate constant R_{reg} . (b) Forward-bias voltage (open circles) is constantly applied. . .	56
4.12	Determined regeneration rate constant R_{reg} versus the excess carrier concentration Δn (symbols) from EL shows a proportional increase. The red squares show measurements on 2 Ω cm and the green diamonds on 2.5 Ω cm PERC cells.	57
4.13	Lifetime evolution during regeneration measured at the regeneration temperature. (a) Injection-dependent lifetime measurements after different times of illuminated annealing with stars indicating lifetimes at $\Delta n = 1 \times 10^{15} \text{ cm}^{-3}$ and diamonds indicating lifetimes at a constant illumination intensity of 1.3 suns. (b) Extracted lifetime evolutions at $\Delta n = 1 \times 10^{15} \text{ cm}^{-3}$ and $I_{\text{ill}} = 1.3$ suns, taken from [88].	59
5.1	(a) Lifetime sample on an underlay wafer, which passes through the industrial belt-furnace. (b) Temperature profile measured on a sample with $\text{Al}_2\text{O}_3/\text{SiN}_x:\text{H}$ stack present during RTA, using a type-K thermocouple and temperature tracker from Datapaq.	64

5.2	Measured evolution of the bulk resistivity ρ versus the annealing time at 160 °C in the dark of SiN _x :H-coated 1.4 Ωcm boron-doped Fz-Si samples, RTA-treated at a measured peak temperature ϑ_{peak} of (792±10) °C. The refractive index n of the SiN _x layer is varied between 1.9 (nearly stoichiometric SiN _x) and 2.7 (very silicon-rich SiN _x).	66
5.3	Saturated hydrogen-boron concentration [HB] _{sat} , which can be identified with the total hydrogen concentration, of SiN _x -coated 1.4 Ωcm boron-doped Fz-Si wafers after RTA treatment as a function of the peak temperature ϑ_{peak} measured during rapid thermal annealing (RTA). The solid lines are guides to the eyes.	66
5.4	(a) Bond concentrations before (in black) and after firing (in red) in the SiN _x :H layers. (b) Percentage loss of Si–H (middle bar) and N–H bonds (right bar) in the SiN _x :H layers ($n=2.3$), and the total hydrogen (left bar) loss (sum of Si–H and N–H losses, solid) versus ϑ_{peak} . All concentrations are calculated from FTIR measurements.	67
5.5	Light microscopy images (dark field) of the fired samples of Figure 5.3 for SiN _x :H layers of three different refractive indices n and at different applied peak temperatures ϑ_{peak} . The blistered area fraction (BAF) of the different SiN _x :H is obtained from light microscopy images for different applied different applied ϑ_{peak} .	69
5.6	Evolution of the bulk resistivity ρ of Al ₂ O ₃ /SiN _x :H-coated 1.4 Ωcm boron-doped float-zone silicon (Fz-Si) samples with different Al ₂ O ₃ thicknesses d between 5 and 25 nm as a function of the annealing time at 160 °C in the dark after rapid thermal annealing (RTA). The composition of the SiN _x layers (refractive index $n=2.3$) and the RTA peak temperature ($\vartheta_{\text{peak}} = 770^\circ\text{C}$) are the same for all samples. The sample with 5 nm thick Al ₂ O ₃ layer shows the highest resistivity increase and hence the highest hydrogen content in the silicon bulk. With increasing Al ₂ O ₃ thickness, the hydrogen content in the silicon bulk shows a pronounced decrease.	70
5.7	Saturated hydrogen-boron concentration [HB] _{sat} of Al ₂ O ₃ /SiN _x ($n=2.3$) coated 1.4 Ωcm boron-doped float-zone silicon (Fz-Si) samples after rapid thermal annealing (RTA) treatment as a function of Al ₂ O ₃ thickness for three different peak temperatures ϑ_{peak} (uncertainty of measured peak temperatures is ±10 °C). The solid lines are exponential decay fits to extract the diffusion length L of hydrogen in Al ₂ O ₃ . The open triangles are taken from Figure 5.3 and the open square is measured on a wafer coated only by 20 nm of Al ₂ O ₃ and omitting the SiN _x :H.	71
5.8	The diffusion length is proportional to the square root of the diffusion coefficient. Therefore, the activation energy E_A of hydrogen diffusion through aluminum oxide in c-Si can be determined by linear fit over the Arrhenius relation (solid lines; dashed lines indicate the uncertainties).	72

- 5.9 Lifetime measurements on $\text{Al}_2\text{O}_3/\text{SiN}_x\text{:H}$ -coated $1.1\ \Omega\text{cm}$ boron-doped Cz-Si samples at a fixed injection density of $\Delta n = 1 \times 10^{15}\text{cm}^{-3}$. The SiN_x layers have a refractive index n about 2.3. (a) Measured lifetimes after firing versus the measured peak temperature ϑ_{peak} . The Al_2O_3 layers are 5 nm thick. (b) Measured lifetimes after RTA-treatment at a measured peak temperature ϑ_{peak} of $(773 \pm 10)^\circ\text{C}$ with a belt speed of 6.8 m min^{-1} and subsequent dark-annealing at 200°C on a hot-plate as well as subsequent illumination at room temperature versus the Al_2O_3 thickness d (lower x-axis) and the saturated hydrogen-boron concentration $[\text{HB}]_{\text{sat}}$ (upper x-axis). 74
- 5.10 Determination of the saturated hydrogen-boron concentration $[\text{HB}]_{\text{sat}}$ by resistivity change measurements. Evolution of the bulk resistivity ρ of $\text{Al}_2\text{O}_3/\text{SiN}_x\text{:H}$ -coated (a) $1.3\ \Omega\text{cm}$ boron-doped Fz-Si samples and (b) $1.1\ \Omega\text{cm}$ Cz-Si samples with two different Al_2O_3 thicknesses d as a function of the dark-annealing time at 160°C after firing. The measured peak-temperature is $\vartheta_{\text{peak}} = (765 \pm 10)^\circ\text{C}$ and the composition of the SiN_x layers (refractive index $n = 2.3$) is the same for all samples. The sample with 5 nm thick Al_2O_3 layer shows the highest resistivity change and hence the highest hydrogen content in the silicon bulk as shown in (c) and (d), where the saturated hydrogen-boron concentration $[\text{HB}]_{\text{sat}}$ is plotted versus the Al_2O_3 thickness for (c) Fz-Si and (d) Cz-Si samples. The samples without any silicon nitride layer (opened symbols) show the lowest hydrogen content in the silicon bulk. 75
- 5.11 Degradation behaviour under illumination with an illumination intensity I_{ill} of 0.1 suns at room temperature. (a) Evolution of the lifetime at an excess carrier density of $\Delta n = 10^{15}\text{ cm}^{-3}$ for p -type Fz-Si reference lifetime samples. (b) Evolution of the lifetime at $\Delta n = 10^{15}\text{ cm}^{-3}$ for Cz-Si lifetime samples with different hydrogen concentrations (10 nm Al_2O_3 =lowest hydrogen concentration, 5 nm $\text{Al}_2\text{O}_3/\text{SiN}_x\text{:H}$ =highest hydrogen concentration in these experiments) in the silicon bulk. Two samples (filled and opened symbols) per hydrogen concentration are shown. Comparable degradation curves are obtained for the other Cz-Si samples. 77
- 5.12 Impact of hydrogen on the BO-related lifetime degradation kinetics. (a) Degradation rate constant R_{deg} versus the hydrogen concentration in the bulk of the investigated samples. (b) Maximum effective defect concentration $N_{\text{t,max}}^*$ versus the hydrogen concentration. Each data point corresponds to a single sample. 78
- 5.13 Regeneration behaviour under illumination at an illumination intensity I_{ill} of 1 suns at 160°C . (a) Evolution of the lifetime at $\Delta n = 10^{15}\text{ cm}^{-3}$ for p -type Fz-Si reference lifetime samples. (b) Evolution of the lifetime at $\Delta n = 10^{15}\text{ cm}^{-3}$ for Cz-Si lifetime samples with different hydrogen concentrations (10 nm Al_2O_3 =lowest hydrogen concentration, 5 nm $\text{Al}_2\text{O}_3/\text{SiN}_x\text{:H}$ =highest hydrogen concentration in these experiments) in the silicon bulk. 79

-
- 5.14 The determined regeneration rate constants R_{reg} from the $N_t^*(t)$ evolutions plotted versus the saturated hydrogen-boron concentration $[\text{HB}]_{\text{sat}}$, which is a measure for the total hydrogen concentration in the silicon bulk. Each data point corresponds to one Cz-Si sample. The straight orange line is a linear fit to the data, clearly showing a non-zero intercept with the y-axis. 80
- 6.1 Photograph of the *c.FIRE.REG* furnace from Centrotherm International AG with a high-temperature zone for fast-firing (*c.FIRE*) and a low-temperature zone with an illumination unit for regeneration of the lifetime (*c.REG*) [109]. 85
- 6.2 Lifetime evolution, measured in the wafers' center, of *p*-type Cz-Si materials A, B, C and D from different manufacturers (filled symbols) and an Fz reference sample (open circles) under illumination at 0.1 suns at 30 °C after (a) firing in an industrial belt furnace and (b) after firing with subsequent regeneration in an industrial belt furnace. The measured lifetimes in the corner of D-1 are added as open squares. 87
- 6.3 Photoconductance-calibrated photoluminescence lifetime imaging (PC-PLI) measurements of materials A, C and D-1 after firing with subsequent regeneration and different times of illumination near room temperature. 89
- 6.4 Injection-dependent lifetime measurements at different locations from PC-PLI measurements for the materials (a) A, (b) C and (c) D-1 after firing with subsequent regeneration in an industrial conveyor-belt furnace (0 h) and after 587 h as well as 2.2 years of illumination at room temperature after regeneration. Black framed symbols correspond to the center, whereas full and open symbols correspond to corner and middle position, respectively. 90
- 6.5 Normalized defect-related lifetime $\tau_{\text{def}}/\tau_{n0}$ of the light-induced defect for fired *p*-type Cz-materials A, C and D-1 as a function of the electron-to-hole concentrations n/p . The Q values were extracted from the slopes of the linear fits (solid lines; dashed lines indicate the experimental uncertainties) to the measurements for degradation under typical illumination conditions (room temperature, 0.1 suns) (a) after firing (filled symbols) and (b) after firing with subsequent industrial regeneration (open symbols). The extracted Q values do not change due to the regeneration within the measurement uncertainty. 93

List of Tables

2.1	Calibration constants from Yin and Smith [18] for the characteristic absorption peaks of the different atomic bonds within the silicon nitride layers and from IOC88 standard for the characteristic oxygen absorption peaks.	16
2.2	Silicon nitride set deposition parameters of the two different tools used in this thesis.	26
5.1	Measured cooling rates of fired Cz-Si lifetime samples with different Al ₂ O ₃ thicknesses in Al ₂ O ₃ /SiN _x stacks or with only-Al ₂ O ₃ layers in a temperature range between 575°C and 625°C.	75
6.1	Resistivities ρ and interstitial oxygen (O _i) concentrations of the investigated boron-doped Cz-Si materials of various manufacturers. The ρ values are obtained from 4-point-probe measurements and the O _i concentrations from FTIR measurements.	84

Abbreviations

Acronym	Description
APT	aperture
BO	boron-oxygen
BRC	background defect center
BAF	blistered area fraction
CP4	damage etch
Cz-Si	Czochralski-grown silicon
D1, D2	detector
EL	electroluminescence
FF	fill factor
FRC	fast-forming recombination center (until 2019)
FTIR	Fourier Transform Infrared
Fz-Si	Float-zone silicon
ICP	inductively coupled plasma
LC	latent center
LC*	immediate precursor of recombination-active center
LCS	modified latent center (since 2013)
LeTID	light and elevated temperature-induced degradation
LID	light-induced degradation
MIR	mid-infrared
MS	mass spectrometry
OPF	optical filter
PA-ALD	plasma-assisted atomic layer deposition (\equiv PE-ALD)
PCD	photoconductance-decay
PC-PLI	photoconductance-calibrated photoluminescence imaging
PE-ALD	plasma-enhanced atomic layer deposition (\equiv PA-ALD)
PECVD	plasma-enhanced chemical vapour deposition
PERC	passivated emitter and rear cell/ contacted
PL	photoluminescence
QSSPC	quasi-steady-state photoconductance
RC	recombination center
RC ₁	identical with SRC with advanced definition (since 2019)
RC ₂	identical with FRC with advanced definition (since 2019)
RT	room temperature
RTA	rapid thermal annealing
Si-CCD	silicon charge coupled device
SRC	slow-forming recombination center (until 2019)
SRH	Shockley-Read-Hall
TC	transient center

XIV **Abbreviations**

Acronym	Description
TMA	trimethylaluminum

Arabic symbols

Symbol	Description	Unit
B	coefficient of radiative recombination	$\text{cm}^{-3}\text{s}^{-1}$
$[B]$	boron doping concentration	cm^{-3}
c	percentage concentration loss	%
c_{light}	speed of light	m/s
C_i	calibration constant for EL analysis	–
C_n	Auger coefficient for the eeh-process	$\text{cm}^{-3}\text{s}^{-1}$
C_p	Auger coefficient for the ehh-process	$\text{cm}^{-3}\text{s}^{-1}$
$[C_s]$	substitutional carbon concentration	cm^{-3}
d	layer thickness	nm
E_0	amplitude of electric field component (Maximum)	V/m
E_A	acceptor energy level	eV
E_A	activation energy	eV
E_C	conduction band edge	eV
E_D	donor energy level	eV
$E_{\text{deg,fast}}$	activation energy of the fast stage of degradation	eV
$E_{\text{deg,slow}}$	activation energy of the slow stage of degradation	eV
E_f	electric field component	V/m
E_V	valence band edge	eV
f	frequency	s^{-1}
G	generation rate	cm^{-3}/s
$[Ga]$	gallium doping concentration	cm^{-3}
$[H]$	hydrogen concentration	cm^{-3}
$[H]_{\text{after firing}}$	hydrogen concentration after firing	cm^{-3}
$[H]_{\text{before firing}}$	hydrogen concentration before firing	cm^{-3}
$[H]_{\text{loss}}$	hydrogen loss	cm^{-3}
I_{cell}	cell current	mA
$I_{\text{i,cell}}$	illumination intensity measured by reference cell	suns
I_{ill}	illumination intensity	sun
I_{PL}	intensity of the photoluminescence signal	counts s^{-1}
J_n	electron current density	mA/cm^2
$J_{\text{sc,1 sun}}$	short-circuit current density of the reference cell under 1 sun	$\text{A cm}^{-2}\text{sun}^{-1}$
k	electron-to-hole capture cross-section ratio	–
K	calibration factor for FTIR analysis	cm^{-1}
K_{eq}	equilibrium constant	cm^{-3}
k_{sample}	extinction coefficient of the sample	–
n_0	electron concentration in thermal equilibrium	cm^{-3}
n_1	electron SRH density	cm^{-3}

Symbol	Description	Unit
n	electron concentration	cm^{-3}
n	refractive index	–
N_A	acceptor doping concentration	cm^{-3}
$N_{\text{d,eq}}^*$	equilibrium effective defect concentration	μs^{-1}
n_i	intrinsic carrier concentration	cm^{-3}
N_{dop}	doping concentration	cm^{-3}
$[\text{N} - \text{H}]$	nitrogen hydrogen bond concentration	cm^{-3}
N_{t}	concentration of defect centers/ recombination centers	cm^{-3}
N_{t}^*	effective defect concentration	μs^{-1}
$N_{\text{t,max}}^*$	maximum effective defect concentration	μs^{-1}
$[\text{O}_i]$	interstitial oxygen concentration	cm^3
p_1	hole SRH density	cm^{-3}
p	hole concentration	cm^{-3}
p_0	net doping concentration	cm^{-3}
q_e	elementary charge	C
Q	electron-to-hole capture time constant ratio	–
$R_{808\text{ nm}}$	reflectivity at a wavelength of 808 nm	–
R	reflectance	–
R_{de}	deactivation rate constant ($\equiv R_{\text{reg}}$)	h^{-1}
R_{deg}	degradation rate constant	s^{-1}
$R_{\text{deg,fast}}$	fast component of lifetime degradation	s^{-1}
$R_{\text{deg,slow}}$	slow component of lifetime degradation ($\equiv R_{\text{deg}}$)	s^{-1}
R_{reg}	regeneration rate constant ($\equiv R_{\text{de}}$)	h^{-1}
r_s	reflection coefficient of s-polarized light	–
R_S	series resistance	Ω
r_p	reflection coefficient of p-polarized light	–
s	speed of light in a medium	m/s
S_{eff}	effective surface-recombination velocity	cm/s
$[\text{Si} - \text{H}]$	silicon hydrogen bond concentration	cm^{-3}
t	total layer thickness including front and back side	cm
T	transmission	%
T_{eff}	effective transmission	–
U	recombination rate	$\text{cm}^{-3}\text{s}^{-1}$
U_0	equilibrium radiative recombination rate	$\text{cm}^{-3}\text{s}^{-1}$
U_{Auger}	Auger recombination rate	$\text{cm}^{-3}\text{s}^{-1}$
U_{eff}	effective recombination rate	$\text{cm}^{-3}\text{s}^{-1}$
$U_{\text{rad,total}}$	total radiative recombination rate	$\text{cm}^{-3}\text{s}^{-1}$
V_{appl}	forward-bias applied voltage	mV
v_M	velocity of the moveable mirror	cm/s
V_i	local junction voltage	mV
V_{oc}	open-circuit voltage	mV
v_{th}	thermal velocity	cm/s
V_{th}	thermal voltage	mV
W	wafer thickness	μm

Symbol	Description	Unit
$[X - Y]_{\text{loss}}$	concentration loss of atomic bond X - Y	cm^{-3}

Greek symbols

Symbol	Description	Unit
α	absorption coefficient	cm^{-1}
α_{O}	absorption coefficient of oxygen	cm^{-1}
Δn	excess electron density	cm^{-3}
Δp	excess hole density	cm^{-3}
Δ	phase difference between the p- and s-polarization	π
η	efficiency	%
θ	incidence angle	$^{\circ}$
$\theta(\nu)$	transmittance spectra	cm^{-1}
θ_{B}	Brewster angle	$^{\circ}$
ϑ	temperature	$^{\circ}\text{C}$
ϑ_{peak}	measured peak-temperature during firing	$^{\circ}\text{C}$
ϑ_{reg}	regeneration temperature	$^{\circ}\text{C}$
λ	wavelength	nm
μ_{n}	mobility of electrons	$\text{cm}^2\text{V}^{-1}\text{s}^{-1}$
μ_{p}	mobility of holes	$\text{cm}^2\text{V}^{-1}\text{s}^{-1}$
ν	optical frequency	s^{-1}
$\bar{\nu}$	wave number	cm^{-1}
ρ	total change in the polarization state	–
σ_0	sample's conductance in the dark	Ω^{-1}
σ	sample's conductance	Ω^{-1}
σ_n	capture cross-section of electrons	cm^2
σ_p	capture cross-section of holes	cm^2
σ_{ph}	photoconductance	Ω^{-1}
τ_0	lifetime directly measured after dark-annealing	μs
$\tau_{0\text{p}}$	lifetime measured after permanent complete BO-deactivation	μs
τ	lifetime	μs
τ_{Auger}	Auger lifetime (Auger recombination lifetime)	μs
τ_{bulk}	bulk lifetime (bulk recombination lifetime)	μs
τ_{d}	lifetime measured after complete degradation	μs
τ_{eff}	effective lifetime	μs
τ_{rad}	radiative lifetime (radiative recombination lifetime)	μs
τ_{SRH}	SRH lifetime (SRH recombination lifetime)	μs
τ_{surface}	surface lifetime	μs
Φ	photon flux for excitation	$\text{s}^{-1}\text{m}^{-2}$
$\Phi_{\text{i,EL}}$	electroluminescence intensity	counts/s
Ψ	amplitude ratio between p- and s-polarization	–

XX
Greek symbols

Symbol	Description	Unit
ω	angular frequency	rad/s

Chemical formula

Formula	Compound
Al_2O_3	aluminum oxide
$\text{Al}(\text{CH}_3)_2$	methylaluminium group
B_iB_s	cluster of interstitial boron
$\text{B}_i\text{B}_s\text{O}$	boron oxygen defect complex (since 2013)
B_iO	cluster of interstitial boron
B_iO_2	cluster of interstitial boron
B_iO_{2i}	boron oxygen defect complex (until 2012)
B_sO_{2i}	boron oxygen defect complex (until 2009)
CH_4	methane
$(\text{CH}_3)_3\text{Al}$	trimethylaluminum
CH_3COOH	acetic acid
CO_2	carbon dioxide
GaAs	gallium arsenide
H_2	molecular hydrogen
HB	hydrogen-boron pair
HCl	hydrochloric acid
HF	hydrofluoric acid
HNO_3	nitric acid
H_2O_2	hydrogen peroxide
NH_3	ammonia
O_2	oxygen dimer
OH	hydroxyl group
Si	silicon
SiN_x	silicon nitride
Si-OH	silanol group

Danksagung

Abschließend möchte ich mich bei allen, die zum Gelingen dieser Arbeit beigetragen haben, bedanken:

- **Prof. Dr. Jan Schmidt** für die herzliche Aufnahme in die Arbeitsgruppe „Photovoltaik-Materialforschung“ sowie für die sehr gute und intensive wissenschaftliche Betreuung mit überaus lehrreichen Diskussionen im Rahmen von Experimenten oder dem Erstellen von wissenschaftlichen Publikationen.
- **Prof. Dr. Tobias Wietler** und **Prof. Dr. Michael Seibt** für die bereitwillige Übernahme der Koreferate und
- **Prof. Dr. Olaf Lechtenfeld** für die Übernahme des Vorsitzes der Promotionskommission.

Ein besonderer Dank gilt außerdem **Dr. Dominic Walter** für die hilfreichen Diskussionen und Anregungen, sowohl für die Anfertigung von Veröffentlichungen als auch für das experimentelle Arbeiten.

Ebenso möchte ich mich bei **Conny Marquardt** für die tolle Unterstützung bei der Probenprozessierung bedanken, seien es die Reinigungen, das Ätzen oder die Diffusionen von Wafern auf dem Weg zur Lebensdauerprobe gewesen. Genauso möchte ich mich bei **Johannes Schlieker** und **Andreas Treder** aus der Werkstatt für die tolle Unterstützung und die hilfreichen Diskussionen bezüglich der Konzipierung meiner Bestromungszelle bedanken.

Außerdem möchte ich mich bei allen **KollegInnen am ISFH** bedanken für die außergewöhnlich kollegiale angenehme Arbeitsatmosphäre und die Unterstützung beim experimentellen Arbeiten, insbesondere bei Ingo Ahrens und Sascha Wolter für die Hilfe beim eigens konzipierten Messaufbau sowie Helge Hannebauer für das Bereitstellen von PERC Solarzellen mit bekannten Prozessparametern. Ich konnte stets auf eure engagierte Mithilfe bei auftretenden Herausforderungen zählen.

Nicht zuletzt gilt ein besonderer Dank meinen **Eltern**, die mich während meines Studiums immer großartig unterstützt haben. Danken möchte ich auch meinem Freund, der mir während dieser intensiven Zeit eine große Stütze war.

Curriculum vitae

Persönliche Daten

Name	Lailah Helmich
Anschrift	Roseggerstraße 2, 30173 Hannover
Geburtsdatum	04.11.1991
Staatsangehörigkeit	deutsch

Studium

Leibniz Universität Hannover

2017-2022	Promotion in der Physik
<i>Promotionsarbeit am</i>	<i>Institut für Festkörperphysik</i>
2014-2016	Masterstudium der Analytik
<i>Masterarbeit am</i>	<i>Institut für Physikalische Chemie</i>
2010-2015	Bachelorstudium der Chemie
<i>Bachelorarbeit am</i>	<i>Institut für Anorganische Chemie</i>

Schul Ausbildung

2004-2010	Goethegymnasium Hildesheim, Abi 8 8.Klasse übersprungen
2002-2004	Orientierungsstufe OS Stadtmitte in Hildesheim
1998-2002	Grundschule Pfaffenstieg in Hildesheim

Anstellung

Leibniz Universität Hannover

Institut für Anorganische Chemie

2013-2014	Studentische Hilfskraft
2015-2016	Wissenschaftliche Hilfskraft

Institut für Solarenergieforschung Hameln (ISFH)

seit Februar 2017	wissenschaftliche Mitarbeiterin
--------------------------	---------------------------------